Guided-Wave Superconducting Quantum Optoelectronic Devices

by

Behnood Ghohroodi Ghamsari

A thesis
presented to the University of Waterloo
in fulfillment of the
thesis requirement for the degree of
Doctor of Philosophy
in
Electrical and Computer Engineering

Waterloo, Ontario, Canada, 2010

I hereby declare that I am the sole author of this thesis. This is a true copy of the thesis, including any required final revisions, as accepted by my examiners.

I understand that my thesis may be made electronically available to the public.

Abstract

This thesis investigates a novel optoelectronic platform based on the integration of superconductive structures, such as thin films and micro-constrictions, with optical waveguides for ultra-fast and ultra-sensitive devices with applications including high-speed optical communications, quantum optical information processing, and terahertz (THz) devices and systems.

The kinetic-inductive photoresponse of superconducting thin films will be studied as the basic optoelectronic process underlying the operation of these novel devices. Analytical formulation for the non-bolometric response is presented, and experimental photodetection in YBCO meander-line structures will be demonstrated.

A set of superconducting coplanar waveguides (CPW) are designed and characterized, which support the operation of the devices at microwave frequencies. Microwave-photonic devices comprising a microwave transmission line and a light-sensitive element, such as a meander-line structure, are designed and measured for implementation of optically tunable microwave components.

In order to support low-loss and low-dispersion propagation of millimeter-wave and THz signals in ultra-fast and wideband kinetic-inductive devices, surface-wave transmission lines are proposed, incorporating long-wavelength Surface Plasmon Polariton (SPP) modes in planar metal-dielectric waveguides.

The theory of superconducting optical waveguides, including analytical formulation and numerical methods, is developed in detail. The implementation of superconducting optical waveguides is discussed thoroughly, employing conventional dielectric-waveguide techniques as well as optical SPP modes.

Superconductive traveling-wave photodetectors (STWPDs) are introduced as a viable means for ultra-fast and ultra-sensitive photodetection and photomixing. A modified trans-

mission line formalism is developed to model STWPDs, where light is guided through an optical waveguide and photodetection is distributed along a transmission line.

As an appendix, a systematic approach is developed for the analysis of carrier transport through superconducting heterostructures and micro-constrictions within the Bogoliubov-de Gennes (BdG) framework. The method is applied to study the role of Andreev reflection and Josephson-like phenomena in the current-voltage characteristics of inhomogeneous superconducting structures. I-V characteristics are experimentally demonstrated in YBCO micro-constrictions with potential applications in millimeter-wave and THz devices.

Acknowledgements

It is a pleasure to thank the many people who made this thesis possible. I would like to express my sincere gratitude to my supervisor, Professor A. Hamed Majedi, for his support, encouragement, and guidance. I am also thankful to my co-supervisor, Professor Raymond Laflamme, for his continuous support.

I would like to thank Professor Pierre Berini and Ewa Lisicka-Shzek from the University of Ottawa for taking me into their lab and providing me the opportunity of learning experimental techniques for characterization of plasmonic optical waveguides. I would also like to thank Professor Steven M. Anlage from the University of Maryland for accepting me in his lab and assisting me to measure superconducting devices.

I would like to thank my group member, Haig A. Atikian, for his help in the measurement of several devices in my work and proofreading my thesis.

I am thankful to my committee members, Professor Sujeet K. Chaudhuri and Professor Dayan Ban, for valuable discussions and suggestions and reviewing my thesis. I am also grateful to my committee member, Professor Thomas Jennewine who kindly accepted to take the post from Professor Gregor Weihs, and my external examiner, Professor Roman Sobolewski from the University of Rochester, for taking their time to review my thesis.

I acknowledge the financial support from the University of Waterloo and the Institute for Quantum Computing under the Mike and Ophelia Lazaridis Fellowship.

Finally, no words can describe my gratitude to my beloved wife, Jeyran, without her support and understanding this work would have been impossible.

Dedicated to my beloved wife, Jeyran.

Contents

List of Tables

List of Figures

List of Abbreviations

AF-PPWG Air-Filled Parallel Plate Waveguide

APM Argument Principle Method

BCS Bardeen-Cooper-Schrieffer

BdG Bogoliubov-de Gennes

BTK Blonder-Tinkham-Klapwijk

CMOS Complementary Metal-Oxide-Semiconductor

DF-PPWG Dielectric-Filled Parallel Plate Waveguide

FIR Far Infra-Red

HTS High-Temperature Superconductors

KID Kinetic Inductive Detector

LAO Lanthanum Aluminate Oxide

LRSPP Long-Range Surface Plasmon Polariton

MD-SW Metal-Dielectric Surface Waveguide

MIM Metal-Insulator-Metal

MSM Metal-Semiconductor-Metal

NEP Noise Equivalent Power

NIR Near Infra-Red

NS Normal-Superconductor

PMF Polarization-Maintaining Fiber

RF Radio Frequency

SFQ Single-Flux Quantum

SNSPD Superconducting Nano-Wire Single Photon Detector

SQUID Superconducting Quantum Interference Device

STJ Superconducting Tunnel Junction

STWPD Superconductive Traveling-Wave Photodetector

TBCCO Thallium Barium Calcium Copper Oxide

TE Transverse Electric

TEM Transverse Electromagnetic

TES Transition-Edge Sensor

TM Transverse Magnetic

UV Ultra-Violet

WKBJ Wentzel-Kramers-Brillouin-Jeffreys

YBCO Yttrium Barium Copper Oxide

YSZ Yttria-Stabilized Zirconia

List of Symbols

A	area
$A(t)$	absorbed power density
B_i	quasiparticle boundary matrix
C	differential capacitance of a transmission line
G	differential conductance of a transmission line
I_Q	quantum current responsivity
I_n	normal current
I_s	supercurrent
L	differential inductance of a transmission line
L_k	kinetic inductance
M	transfer matrix
N	electron number density at the normal state
P_0	average incident optical power
P_i	quasiparticle propagator matrix
Q	differential charge of a transmission line
R	differential resistance of a transmission line
R_n	normal resistance
R_v	voltage responsivity

S	surface
T	temperature
T_c	critical temperature
U	electrostatic potential
V	volume
V_{ph}	photo-voltage
W	width
Y	differential admittance of a transmission line
Z	differential impedance of a transmission line
Z_c	transmission line characteristic impedance
Δ	superconductor energy gap
Δ_k	superconductor energy gap in the k direction
Λ	superconductor London parameter
Φ	electric potential function
Ψ	quasiparticle state vector
α	attenuation constant
β	phase constant
δ_o	optical penetration depth
ℓ	thickness
ϵ	electric permittivity
η_B	thermalization efficiency
η_Q	pair breaking quantum efficiency
γ	complex propagation constant
$\hbar$	Planck's reduced constant

$\mathbf{B}$	magnetic flux density vector
$\mathbf{D}$	electric displacement density vector
$\mathbf{E}$	electric field vector
$\mathbf{H}$	magnetic field vector
$\mathbf{J}$	electric current density vector
$\mathbf{J}_n$	normal electrons current density vector
$\mathbf{J}_s$	superelectrons current density vector
$\mathbf{P}$	electric polarization vector
$\mathbf{v}_s$	superelectron's velocity
μ	magnetic permeability
ω	angular frequency
ϕ	magnetic flux
ψ	scalar wavefunction
ρ	electric charge density
σ	electric conductivity
σ_0	electric dc conductivity
τ_Δ	gap relaxation time constant
τ_B	bolometric photoresponse time constant
τ_Q	nonequilibrium photoresponse time constant
τ_{e-P}	electron-phonon interaction time
τ_{ee}	electron-electron interaction time
τ_{th}	thermalization time constant
τ_{tr}	electron scattering time
d	length

e	elementary electric charge
g_B	bolometric quantum yield
g_B	nonequilibrium quantum yield
k_i	current conversion factor
k_v	voltage conversion factor
m^*	mass of a superelectron
m_0	electron rest mass
n	number density of the normal electrons
n^*	number density of the Cooper pairs
$p(t)$	spontaneous optical irradiance
q	electric charge
q^*	electric charge of a superelectron

With them the seed of Wisdom did I sow,
And with mine own hand wrought to make it grow;
And this was all the Harvest I reap'd–
"I came like Water, and like Wind I go."

Omar Khayyám, Persian Poet and Mathematician– 1048-1131 A.D.

Chapter 1

Introduction

1.1 Superconducting Optoelectronics

Superconducting optoelectronics has been a rapidly growing field of research during the last two decades. Although the study of the photoresponse of superconducting films and junctions [5–8] dates back to the discovery of the microscopic theory of superconductivity [9], it was not until recently that superconducting structures were seriously sought to be employed as practical optoelectronic devices [10–13]. Ever since the pioneering works in the early 90s [14, 15], where the idea of superconducting optoelectronics was conjectured with emphasis on the use of high-temperature superconductors (HTS) as optoelectronic materials, great theoretical and experimental steps have been taken by a number of researchers and groups towards the implementation and realization of superconducting optoelectronic devices. Among these achievements are the invention and development of several novel optoelectronic devices, such as superconducting nanowire single photon detectors (SNSPDs) [16, 17] and kinetic inductive detectors (KIDs) [18, 19]. The high speed and/or ultra-sensitivity of superconducting optoelectronic devices operating at visible and

near infrared wavelengths are on demand for a variety of applications, such as deep space and satellite communications, optical-to-electrical interconnects for ultra-fast single-flux-quantum (SFQ) digital processors, high-speed modulation and broadband photodetection for optical communications, probing CMOS integrated circuits using photon emission timing analysis, and quantum key distribution systems [20–23]. In the visible to ultraviolet regime, the photon counting and photon-energy resolving properties of superconducting optoelectronic devices, such as transition-edge sensors (TES) [24], superconducting tunnel junctions (STJ) [25], and KIDs [18], are very desirable for spectroscopy and astronomical applications. At the terahertz (THz) and far infrared region of the spectrum, superconducting (photo)mixers and bolometers can provide generation, manipulation, and detection of millimeter-wave and THz radiation, which in turn have many applications in spectroscopy, biosensing, and imaging [26–28].

1.2 Thesis Contributions and Organization

Regardless of the operational details, such as operating wavelength and the application, an optoelectronic device is generally composed of three essential parts. The most prominent of all is an optoelectronic process that produces electronic or optical perturbations, as a response to optical or electrical excitations, respectively. The second part is a means for supporting the propagation of the electrical input/output signals. For low-frequency electrical signals, where a device is considered a lumped-element component, a simple conducting path would suffice. However, for fast devices operating at microwave and millimeter-wave regime, the use of transmission lines and waveguides is inevitable. The third part is a photonic structure that provides the coupling between the optical waves and the active region where the optoelectronic process takes place. For simple devices, this structure could be

as straightforward as a focusing lens, whereas more sophisticated photonic structures such as a cavity resonator or an optical waveguide, are utilized for more advanced devices.

Within the aforementioned conceptual framework, this thesis introduces a novel platform for development of ultra-fast and ultra-sensitive optoelectronic devices based on superconducting structures and materials. The kinetic-inductive photoresponse of superconducting thin films, superconducting microwave transmission lines, and superconducting optical waveguides comprise the three basic elements of this novel optoelectronic platform.

Chapter 2 studies the kinetic-inductive photoresponse of superconducting thin films. Because the existing photoresponse models, such as the rate equations [29] and gap thermomodulation along with the heat-diffusion model [30, 31], are mostly focused on lumped element devices or the fast bolometric response, a new phenomenological formulation of the problem is developed that accounts for the non-bolometric response and can be readily extended for the analysis and design of distributed devices as well. The new formulation takes the non-equilibrium carriers life-time as a phenomenological input, in much the same way as in semiconductor photoconductive devices, and predicts the responsivity of a superconducting kinetic-inductive detector. The optical pair breaking is related to the perturbation of the kinetic inductance, which results in a photoinduced voltage by means of an external dc bias current. While the kinetic-inductive photoresponse will be shown to be generally nonlinear, the linear response under the small signal condition is discussed in some detail. Finally, a YBCO meander-line structure is experimentally tested under different operating conditions, to demonstrate the kinetic-inductive optoelectronic mechanism.

Chapter 3 is devoted to the design, development, and measurement of superconducting

microwave transmission lines. A set of YBCO coplanar waveguides (CPW), operating up to 50GHz, has been designed and experimentally tested to provide the microwave template of the optoelectronic devices. Moreover, it is experimentally shown that by means of incorporating a light-sensitive element, such as a superconducting meander-line, microwave properties of the device may be optically tuned. This microwave-photonic platform is employed to demonstrate tunable resonators and delay lines.

Since the kinetic-inductive photoresponse enhances at the millimeter-wave and THz regimes, it provides a promising tool for ultra-fast photodetection and high-frequency photomixing. To support low-loss and low-dispersion propagation of millimeter-wave and THz signals, chapter 4 studies metal-insulator-metal (MIM) waveguides. The analysis is general and is not limited to superconducting structures. It will be shown that the coupled surface plasmon polariton (SPP) waves at the two metal-dielectric interfaces may be utilized as a THz surface-wave transmission line. Based on analytical and numerical field analysis, the voltage and current waves are properly defined and the line parameters are obtained.

Inasmuch as the optical waveguides constitute the main ingredient of advanced optoelectronic devices, the theory of superconducting optical waveguides, including analytical formulation, numerical solution, and design criteria has been thoroughly developed in chapter 5. Designs similar to dielectric optical waveguides as well as novel designs relying on Surface Plasmon Polariton (SPP) modes have been presented and discussed. Furthermore, an experimental setup for characterization of optical waveguides and particularly long-range surface plasmon optical waveguides has been developed, and is presented in the Appendix B.

Chapter 6 proposes a novel class of optoelectronic devices, namely superconducting traveling-wave photodetectors (STWPDs), for ultra-fast and ultra-sensitive photodetection and millimeter-wave and terahertz photomixing with applications in high-capacity optical communication, quantum-key distribution systems, and terahertz technology. The proposed device is comprised of a distributed kinetic-inductive photodetector along a transmission line integrated with a velocity-matched optical waveguide. The device model is based on a modified transmission line theory, and its bandwidth and efficiency are formulated accordingly.

Appendix C studies carrier transport through inhomogeneous superconducting structures including heterostructures, superlattices, and micro-constrictions. Insofar as reducing the feature size of such structures, for instance micro-bridges, may induce new electronic phenomena, such as the Andreev reflection and Josephson tunneling, a systematic framework for the analysis of inhomogeneous superconducting structures is developed based on the Bogoliubov-de Gennes (BdG) method. Numerical examples and experimental demonstrations will be presented to illustrate the role of the Andreev reflection and Josephson-like phenomena in the I-V characteristic of superconducting heterostructures and micro-constrictions. While these effects should be voided in a kinetic-inductive element, nevertheless they may provide a new basis for optoelectronic and microwave-photonic devices.

Chapter 2

Kinetic Inductive Photoresponse in Superconducting Thin Films

2.1 Introduction

This chapter studies the photoinduced changes in the kinetic inductance of a superconducting thin film as the fundamental optoelectronic process responsible for the operation of the devices which will be discussed throughout the rest of this thesis.

The theory of kinetic inductance is briefly reviewed. The effect of optical absorption on the kinetic inductance of a superconducting thin film is discussed, and the regime of linear response is highlighted. Photodetection measurements are presented as the experimental evidences for the kinetic inductive photoresponse in optically illuminated superconducting structures.

2.2 General Theory of Kinetic Inductance

Cooper pairing comprises the underlying mechanism of superconductivity, where two electrons pair up and produce a bound state by means of an attractive potential field at the presence of a fully occupied Fermi gas [32]. These paired electrons, often referred to as Cooper pairs, form a new type of charge carriers that dramatically differ from their constituent normal electrons. Prominently, the excitation spectrum for the Cooper pairs exhibits an energy gap equal to their bounding energy [9], denoted by 2Δ[1]. Consequently, the excitations with a quantum energy less than 2Δ cannot be coupled to the Cooper pairs; and will propagate without any attenuation through a condensate of Cooper pairs, i.e. a superconductor at zero temperature. At a finite temperature, however, the excitations will be attenuated through the coupling to the quasiparticles created by the thermally broken pairs. The extremely low dissipation in superconducting microwave transmission lines and the substantially high quality factor in superconducting microwave resonators [33] are significant experimental consequences of Cooper pairing.

The spatial and spectral distribution of the coexisting Cooper pairs and quasiparticles in a superconducting sample, at a finite temperature, determine the electronic structure of the specimen. However, most of the classical macroscopic properties of superconductors can be accounted for by means of a phenomenological model, namely the two-fluid model [34], in which quasiparticles and Cooper pairs are presumed to constitute two non-interacting fluids. Within this framework, quasiparticles are modeled by normal electrons with a mass

[1]Even for non-BCS superconductors, the magnetic flux quantization experiments demonstrate that the superconducting condensate consists of paired electrons. For anisotropic superconductors, Δ is the minimum of Δ_k, which designates the energy gap along the $\mathbf{k}$ direction.

$m = m_0$ and an electric charge $q = -|e|$,[2] and obey the renowned Ohm's law

$$\mathbf{J} = \sigma \mathbf{E}, \tag{2.1}$$

where $\mathbf{J}$ and $\mathbf{E}$ are the electric current density and the electric field, respectively. The dispersive conductivity σ is, also, given by:

$$\sigma(\omega) \equiv \frac{\sigma_0}{1 + j\omega\tau_{tr}}, \tag{2.2}$$

where ω is the angular frequency, $\tau_{tr}$is the electrons' average scattering time, and $\sigma_0$is the dc conductivity,

$$\sigma_0 \equiv \frac{nq^2\tau_{tr}}{m}, \tag{2.3}$$

in which n designates the number density of the normal electrons in the material. Super-electrons, on the other hand, possess a mass $m^* = 2m_0$ and an electric charge $q^* = -2|e|$, and follow the London equations [35],

$$\mathbf{E} = -\frac{\partial}{\partial t}(\Lambda \mathbf{J}), \tag{2.4}$$

and

$$\mathbf{B} = -\nabla \times (\Lambda \mathbf{J}), \tag{2.5}$$

where $\mathbf{B}$is the magnetic flux density, and Λ is the material's London parameter,

$$\Lambda \equiv \frac{m^*}{n^*(q^*)^2}, \tag{2.6}$$

[2]Here, $m_0 = 9.11 \times 10^{-31} kg$ is the electron rest mass; and $e = 1.602 \times 10^{-19} C$ is the elementary electric charge.

in which n^* denotes the number density of the Cooper pairs in the material. Clearly, both n and n^* are functions of the temperature T. Nonetheless, the following conservation condition must hold at all temperatures in order to conserve the number of free charge carriers within the material,

$$n(T) + 2n^*(T) = N, \tag{2.7}$$

where N is the electron number density for the material at the normal state, i.e. at a temperature higher than the critical temperature T_c.

The combination of Maxwell equations and the London equations construct the classical electrodynamics theory of superconductors, in which the electric current density $\mathbf{J}$ is composed of a normal part $\mathbf{J}_n$, which obeys Ohm's law (2.1), and a supercurrent $\mathbf{J}_s$, which follows the London equations (2.4) and (2.5). In general, the Poynting theorem [36] yields

$$-\oint_S (\mathbf{E}\times\mathbf{H}).\mathbf{ds} = \int_V \left(\mathbf{E}\frac{\partial \mathbf{D}}{\partial t} + \mathbf{H}\frac{\partial \mathbf{B}}{\partial t} + \mathbf{E}.\mathbf{J}\right) dv, \tag{2.8}$$

where S is an arbitrary closed surface within the superconducting material encompassing the volume V , and $\mathbf{H}$ and $\mathbf{D}$ respectively are the magnetic field and the electric displacement density. Given that

$$\mathbf{J} = \mathbf{J}_n + \mathbf{J}_s, \tag{2.9}$$

substituting the constitutive relations (2.1) and (2.4) into (2.8) results in

$$-\oint_S (\mathbf{E}\times\mathbf{H}).\mathbf{ds} = \int_V \left(\mathbf{E}\frac{\partial \mathbf{D}}{\partial t} + \mathbf{H}\frac{\partial \mathbf{B}}{\partial t}\right) dv + \frac{\partial}{\partial t}\int_V \frac{1}{2}\Lambda J_s^2 dv + \int_V \frac{1}{\sigma} J_n^2 dv. \tag{2.10}$$

In right hand side of (2.10), the first term corresponds to the stored electromagnetic energy in the material and the last term corresponds to the ohmic dissipation ; the second term however, shows that energy could also be stored within the supercurrent. The supercurrent

is related to the average velocity of the superelectrons $\mathbf{v}_s$ through

$$\mathbf{J}_s = n^* q^* \mathbf{v}_s. \tag{2.11}$$

Using (2.6) and (2.11),

$$\frac{1}{2}\Lambda J_s^2 = n^* \left(\frac{1}{2} m^* v_s^2\right). \tag{2.12}$$

Equation (2.12) implies that the additional stored energy term corresponds to the kinetic energy of the superelectrons. While the kinetic energy of normal electrons dissipates through collisions with the lattice, such a scattering is prohibited for Cooper pairs due to the energy gap in their excitation spectrum. Therefore, superelectrons transport through the lattice without any collisions, provided that the energy of the photons associated with the electromagnetic field is less than the bounding energy of the Cooper pairs, i.e. $\hbar\omega < 2\Delta$.

The J_s^2 dependence of the new stored energy term suggests it can be equivalently represented by the stored energy in an inductor L_k, often referred to as the kinetic inductance of the superconducting structure, whose magnitude depends on the material parameters and geometry

$$\frac{1}{2} L_k I_s^2 = \int_V \frac{1}{2}\Lambda J_s^2 dv, \tag{2.13}$$

where I_s is the total supercurrent passing through the volume V. While the superelectrons provide an inductive channel for the flow of current in a superconductor, the normal electrons provide a resistive channel, which is represented by the normal resistance of the structure R_n

$$\frac{1}{2} R_n I_n^2 = \int_V \frac{1}{2\sigma} J_n^2 dv, \tag{2.14}$$

where I_n is the total normal current passing through the volume V. Hence, a superconductor with any arbitrary shape could be modeled by a kinetic inductance in parallel with

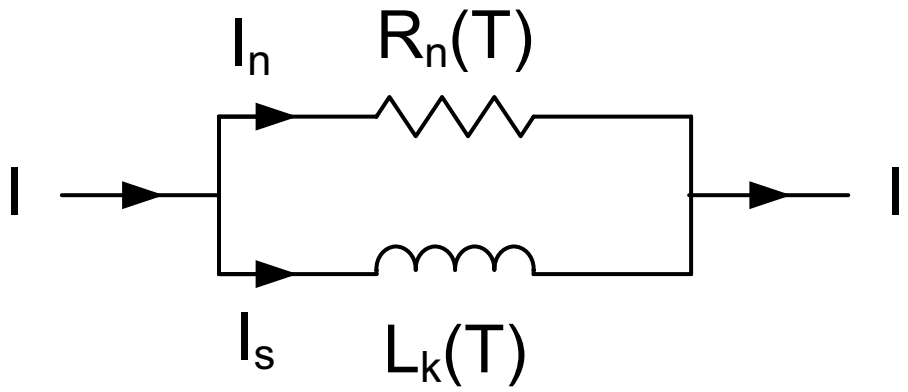

Figure 2.1: The equivalent circuit model of a superconductor in terms of its kinetic inductance L_k and the normal resistance R_n.

a normal resistance, as depicted in Figure 2.1. For a superconductor of length ℓ, in which the supercurrent and the normal current are uniformly distributed over its cross section area A, the kinetic inductance and the normal resistance are respectively given by

$$L_k = \frac{\Lambda \ell}{A} = \frac{m^* \ell}{n^* (q^*)^2 A}, \tag{2.15}$$

and

$$R_n = \frac{\ell}{\sigma_n A} = \frac{m \ell}{n q^2 \tau_{tr} A}. \tag{2.16}$$

2.3 Photodetection in Superconducting Thin Films

Photons with an energy greater than the bounding energy of Cooper pairs[3], i.e. $\hbar\omega > 2\Delta$, can break the pairs and create excess quasiparticles. Therefore, for a superconductor under uniform optical illumination the number density of Cooper pairs, n^*, and quasiparticles, n change from their equilibrium values n_0^* and n_0. The nonequilibrium carrier densities are, in general, functions of both temperature and time,

$$n(T,t) = n_0(T) + \delta n(T,t), \tag{2.17}$$

$$n^*(T,t) = n_0^*(T) + \delta n^*(T,t). \tag{2.18}$$

A number of theories and models exist for finding the nonequilibrium distributions δn^* and δn, differing in the level of adherence to the microscopic theories, mathematical sophistication, generality, and popularity. Rothwarf-Taylor rate equation models [29], phenomenological approaches such as the two-temperature [37] or the μ^* models [5], more fundamental methods like the gap-control equation [38] and fully microscopic techniques such as the Green's function method [39] are a few of the widely-used approaches to name.

In practice, the instantaneous nonequilibrium carrier densities cannot be measured directly, but rather the associated changes in the average macroscopic properties of the superconducting structure are probed for the study of the photoresponse as well as in photodetector devices. These macroscopic changes are often closely related to the kinetic inductance and normal resistance of the structure, which themselves are readily related to the carrier densities. For example, in Transition Edge Sensors (TESs) the change in the resistance of a superconducting sample, at a temperature near its critical temperature

[3]In the rest of the thesis, when a reference to optical illumination is made it is presumed that the condition $\hbar\omega > 2\Delta$ holds.

T_c, as a result of a global phase transition into the normal state is measured for photodetection [24]. In Superconducting Nanowire Single Photon Detectors (SNSPD), a local superconducting-normal phase transition in a current-biased superconducting film at the hot spot produces a photo-voltage pulse [16,17]. Moreover, in the Superconducting Tunnel Junction (STJ) detectors, the resistance of a superconducting tunnel junction is optically modulated [25]; and in the Kinetic Inductive Detectors (KIDs), the photoinduced changes in the kinetic inductance of a microwave resonator shifts the resonance frequency [18].

Therefore, a physical model that approximately predicts the photoinduced changes in the kinetic inductance and normal resistance of a superconducting structure, on the average sense over the time scale of the problem, generally suffices for the purpose of device engineering. Involvement of microscopic techniques and starting from first principles, for engineering purposes, would hardly be an advantage for its own sake. In contrast, some degree of phenomenology would be welcome provided it could lead to a more general, accurate, and flexible framework. The experiment, nevertheless, will ultimately benchmark the validity of any model or theory.

The first experimental study of the photoresponse of superconducting films was performed by Testardi [40] through measuring the resistance change of a Pb film under the illumination of laser pulses. He carefully measured the temperature rise of the film δT as a result of the laser illumination in the normal state, i.e. $T > T_c$. The resistance measurement at temperatures below $T_c - \delta T$ exhibited features which could not be described by a heating model. For instance, the response time was shorter than the thermal response time; and the transition width was much larger compared to the case of no illumination. From these observations and a series of quantitative comparisons, Testardi concluded that the energy of the photons "should initially be shared among the electrons very rapidly, in

a time scale τ_{ee}, followed by a conversion to phonons over a longer time scale τ_{eP}"[4].

Other researchers, also, applied similar techniques to investigate the nonequilibrium photoresponse of other superconductors, such as Nb and YBCO [4, 41–44]. In a prominent work, Bluzer performed photoimpedence measurements on YBCO films at the normal-state $T > T_c$, the transition state $T_c > T > T_c - \delta T$, and the superconducting state $T_c - \delta T > T$ [4]. The experiments showed a thermal photoresponse [5] for the normal and transition states, with a much higher amplitude and time constant for the latter. The higher photoresponse amplitude for the transition state clearly resulted from a more severe change in the sample's impedance because of the phase transition. The longer time constant, however, was attributed to the order parameter relaxation time, which could be greater than the thermalization time constant at temperatures much close to T_c [38, 45]. Nevertheless, the superconducting state photoresponse exhibited more complicated features, such as a sign change in the falling tail of the photoresponse amplitude. Similar results were inferred from the experiments on Nb. To interpret the results, Bluzer employed the Rothwarf-Taylor model, where the dynamics of the three systems of pairs, quasiparticles, and phonons are determined through a set of coupled rate equations [29]. His conclusion about the observed photoresponse in the superconducting state presumed three stages, as depicted in Figure 2.2. The photons are absorbed at time t_0. From time t_0 to t_1, Cooper pair density reduces from n_0^* to n_1^* through electron-electron interactions.[6] From time t_1 to t_2, pair breaking dominates by electron-phonon interactions, wherein Cooper pairs continue to break, though at a slower rate. In the period from t_2 to t_3, phonon escape from the system dominates and quasiparticles begin to recombine. At time t_3, the transient has elapsed and the Cooper pair density restores back to n_0^*.

[4] τ_{ee} and τ_{eP} respectively stand for the electron-electron and electron-phonon interaction time.

[5] This photoresponse is also referred to as the bolometric photoresponse.

[6] This stage greatly resembles the avalanche breakdown in semiconductors; and sometimes is called the cascading stage.

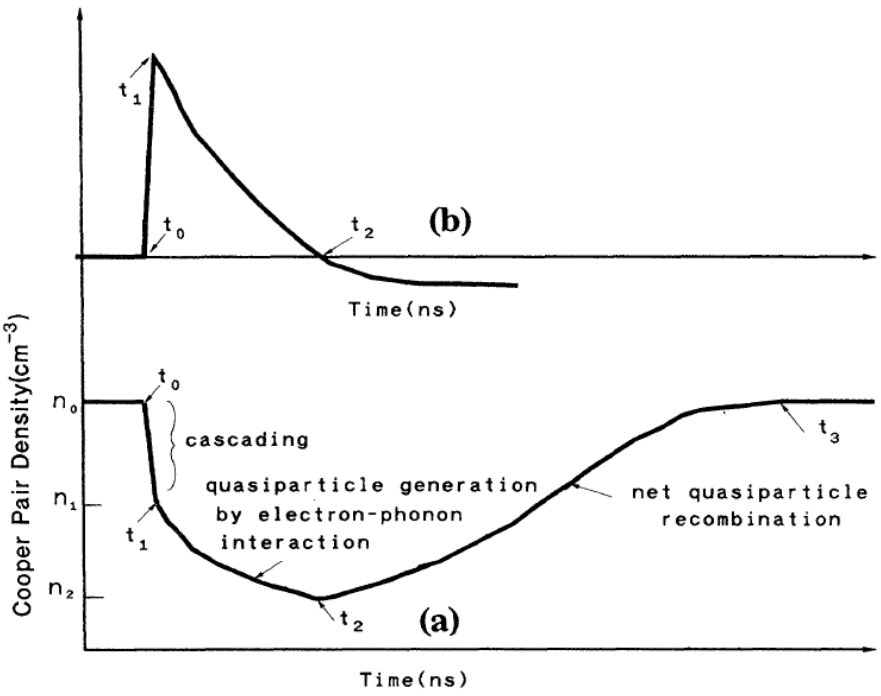

Figure 2.2: Different stages involving the transient photoresponse of a superconducting film. Adapted from [4].

Photoresponse measurements reveal that the rise time of the transient response, i.e. $t_1 - t_0$, is very short. For example, Bluzer reported a rise time less than 50ps which was believed to be limited by the measuring equipment [4]. More recent photoresponse experiments employing an electro-optic sampling technique reported transient times in the order of 1ps for YBCO micro-bridges well below the transition temperature [10, 11, 46, 47]. Such a fast photoresponse is surely non-bolometric[7].

The aforementioned experiments show that the bolometric response can be represented by a time constant τ_B , which depends on the thermalization time constant τ_{th} and the gap relaxation time constant τ_Δ as

$$\tau_B = \max(\tau_{th}, \tau_\Delta). \tag{2.19}$$

Similarly, the nonequilibrium response can also be accounted for by a time constant τ_Q,where

$$\tau_Q \approx t_2 - t_0. \tag{2.20}$$

The time constant τ_Q may be envisioned as the quasiparticle life time in the non-bolometric regime. Clearly, these time constants can be empirically extracted from the photoresponse measurements, nevertheless, more fundamental theories may be used to approximate them in terms of elementary parameters such as τ_{ee} and τ_{e-P} .

Fast and low-noise photodetection calls for exploiting the quantum photoresponse. Inasmuch as kinetic inductance is the most eminent macroscopic property of a superconductor that directly responds to changes in the Cooper pairs density, probing the kinetic inductance of a superconducting structure provides a viable means for quantum photodetection. To this end, several devices have been proposed for kinetic-inductive photodetec-

[7]The non-bolometric photoresponse is also referred to as the quantum photoresponse.

tion [12, 13, 48–52], most of which incorporate weak-links, in the form of SQUID, either as part of the photodetector device or for the read-out. SQUID-based kinetic inductive photodetectors require operation in the voltage state, which adds to the noise-equivalent-power (NEP) of the device, whereas SQUID-based read-out are bulky and complicate the device operation. Hence, the works of this thesis deploy a kinetic inductive photodetection scheme that does not require any superconducting weak-links. In this scheme, the superconducting structure is externally biased by a dc current I_0. The photoinduced changes in the kinetic inductance[8] produce a time varying magnetic flux; which, in turn, results in a voltage pulse due to the Faraday's law,

$$V_{ph} \approx \frac{d}{dt}\left(L_k I_0\right) = I_0 \frac{dL_k}{dt}. \tag{2.21}$$

This technique has been successfully demonstrated in studying the photoresponse of YBCO micro-bridges [10, 11, 46, 47]. Experimental results for photodetector devices will be presented at the end of this chapter.

The following formulates the kinetic inductive photodetection scheme for a superconducting thin film of a cross section area A, a thickness ℓ[9], and an energy gap 2Δ under a uniform monochromatic optical irradiance $p(t)$. This problem was investigated by means of the gap thermo-modulation formalism and heat-transfer method in [30, 31]. However, a phenomenological approach, based on the bolometric and non-equilibrium time constants τ_B and τ_Q, is presented here that readily models the photoinduced changes in the electrical parameters of the structure. In general, the signal $p(t)$ may be represented by a Fourier

[8] The role of quasiparticles is neglected, here, for the sake of simplicity. This matter, nevertheless, will be taken into account in the formal treatment of the problem.

[9] The thickness ℓ is presumed to be smaller than the optical penetration depth δ_o, so that the absorption would be nearly uniform over the thickness.

integral

$$p(t) = \frac{1}{2\pi} \int_{-\infty}^{+\infty} P_S(\omega) e^{j\omega t} d\omega. \tag{2.22}$$

Assume that $P_0 = P_S(0)$ is the average incident optical power. At a temperature close to the critical temperature and for harmonics with $\omega\tau_B < 1$ the bolometric response dominates, whereas at a temperature far from the critical temperature and for harmonics $\omega\tau_B \gg 1$ the non-equilibrium response is dominant. The time-invariant component of the irradiance, P_0, clearly fits into the bolometric regime and changes the Cooper pair density from its equilibrium value n_0^* to the steady-state value n_s^*

$$n_s^* = n_0^* - g_B P_0, \tag{2.23}$$

where g_B is the bolometric quantum yield

$$g_B \equiv \frac{\eta_B \tau_B}{2\Delta A \ell}, \tag{2.24}$$

and η_B is the thermalization efficiency. Therefore, the steady-state normal electrons density changes to $n_s = N - 2n_s^*$. Obviously, equation (2.23) limits the incident average power for staying in the superconducting state. For a sample whose specifications are listed in Table 2.1, the maximum allowed average incident optical power, as a function of the operating temperature, is depicted in Figure 2.3.

Provided that the time varying part of the incident optical power falls into the non-equilibrium regime, the instantaneous Cooper pairs density follows

$$n^*(t) = n_s^* - \delta n^*(t), \tag{2.25}$$

Parameter	Value
Critical Temperature (T_c)	$86.9(K)$
Debye Temperature (Θ_D)	$380(K)$
Critical Current (J_c)	$4(MA/cm^2)$
Energy Gap at $T = 0K$ ($2\Delta_0$)	$32(meV)$
London Penetration Depth at $T = 0K$ (λ_0)	$200(nm)$
Optical Penetration Depth (δ_o)	$100(nm)$
Length (ℓ)×Width (w)×Thickness (t)	$2(\mu m)\times 2(\mu m)\times 100(nm)$
Bolometric Response Time Constant (τ_B)	$1(ns)$
Quantum Response Time Constant (τ_Q)	$1(ps)$
Normal Electron Scattering Time (τ_{tr})	$0.1(ps)$
Normal Conductivity (σ_0)	$5.56(k\mho/cm)$

Table 2.1: Physical parameters associated with a typical YBCO thin film for use in optoelectronic devices.

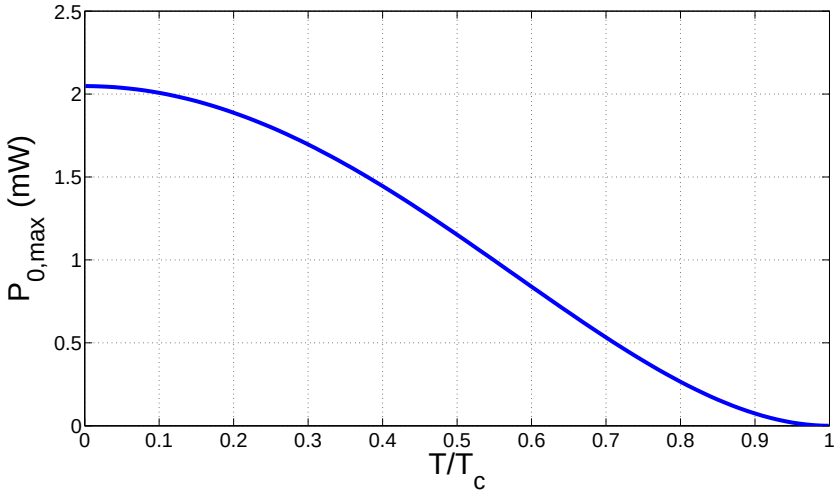

Figure 2.3: Simulation of the temperature variation of the maximum allowable average incident power for the YBCO sample of Table 2.1.

with

$$\delta n^*(t) = g_Q[p(t) - P_0], \tag{2.26}$$

where the nonequilibrium quantum yield g_Q is

$$g_Q \equiv \frac{\eta_Q \tau_Q}{2\Delta A \ell}, \tag{2.27}$$

and η_Q is the pair breaking quantum efficiency. The modulation of the Cooper pair density is accompanied by a modulation in the kinetic inductance and the normal resistance of the film, that is

$$L_k(t) = L_{k0}\left[1 - \frac{\delta n^*(t)}{n_s^*}\right]^{-1}, \tag{2.28}$$

and

$$R_n(t) = R_{n0}\left[1 + \frac{2\delta n^*(t)}{n_s}\right]^{-1}, \tag{2.29}$$

where L_{k0} and R_{n0} are the steady-state parameters, which may be found from (2.15) and (2.16) by means of (2.23) and the carrier conservation condition (2.7). In general,

$$L_k(t) = L_{k0} + \delta L_k(t), \tag{2.30}$$

and

$$R_n(t) = R_{n0} - \delta R_n(t). \tag{2.31}$$

The opposite signs in (2.30) and (2.31) manifest the fact that reducing Cooper pair population increases the kinetic inductance, whereas a raise in the quasiparticles population decreases the normal resistance.

According to the circuit model in Figure 2.1, the photoinduced voltage indexphotoin-

duced voltage reads

$$V_{ph} = \frac{d}{dt}\left[L_k(t)I_s(t)\right], \tag{2.32}$$

where

$$\frac{d}{dt}\left[L_k(t)I_s(t)\right] = R_n\left[I_0 - I_s(t)\right]. \tag{2.33}$$

Assuming $I_s(t) = I_0 + i(t)$, the differential equation (2.33) reduces to

$$(L_{k0} + \delta L_k)\frac{di}{dt} + (I_0 + i)\frac{d}{dt}\delta L_k + (R_{n0} - \delta R_n)i = 0. \tag{2.34}$$

2.4 Linear Response

In light of the above equations, the kinetic inductance photodetection mechanism is obviously nonlinear in general. Nevertheless, the photodetection may be linearized in the small signal regime[10], when $|\delta n^*| \ll n_s^*$ and $2|\delta n^*| \ll n_s$. The conditions of small signal operation are derived in the Appendix A. Upon the small signal assumption, equations (2.28)-(2.31) yield

$$\delta L_k(t) = L_{k0}\frac{\delta n^*(t)}{n_s^*}, \tag{2.35}$$

and

$$\delta R_n(t) = R_{n0}\frac{2\delta n^*(t)}{n_s}. \tag{2.36}$$

Hence, the linear regime corresponds to the case where the photoinduced changes in the kinetic inductance and the normal resistance are small compared to their steady-state values, i.e. $|\delta L_k| \ll L_{k0}$, and $|\delta R_n| \ll R_{n0}$. These conditions, in turn, imply that $|i| \ll I_0$.

[10]Hereafter, the terms "linear regime" and "small signal regime" will be used interchangeably.

Therefore, equation (2.34) may be readily approximated by

$$L_{k0}\frac{di}{dt} + I_0\frac{d}{dt}\delta L_k + R_{n0}i = 0. \tag{2.37}$$

According to (2.22), the kinetic inductive responsivity follows

$$R_v(\omega) \equiv \frac{V_{ph}(\omega)}{P_S(\omega)} = \left(\frac{\eta_Q \tau_Q I_0}{2\Delta A \ell n_s^*}\right)\left(\frac{j\omega L_{k0} R_{n0}}{j\omega L_{k0} + R_{n0}}\right). \tag{2.38}$$

The responsivity is a function of temperature through the temperature dependence of Δ, n_s^*, L_{k0}, and R_{n0}. Two limiting cases of interest are the inductive limit $j\omega L_{k0} \ll R_{n0}$ and the resistive limit $j\omega L_{k0} \gg R_{n0}$. The responsivity at the inductive limit can be approximated by

$$R_v(\omega) = j\omega L_{k0} I_Q, \tag{2.39}$$

whereas at the resistive limit

$$R_v(\omega) = R_{n0} I_Q, \tag{2.40}$$

and the quantum current responsivity I_Q is defined as

$$I_Q \equiv \frac{\eta_Q \tau_Q I_0}{2\Delta A \ell n_s^*}. \tag{2.41}$$

Obviously, the realization of the linear regime at a given temperature, depends on the incident optical power as well as the material parameters. For a thin film with parameters of Table 2.1, the relative photoinduced changes in the kinetic inductance and the normal resistance as a function of peak-to-average signal ratio are depicted in Figure 2.5 and Figure 2.6. The kinetic inductive responsivity of the film is shown in Figure 2.7.

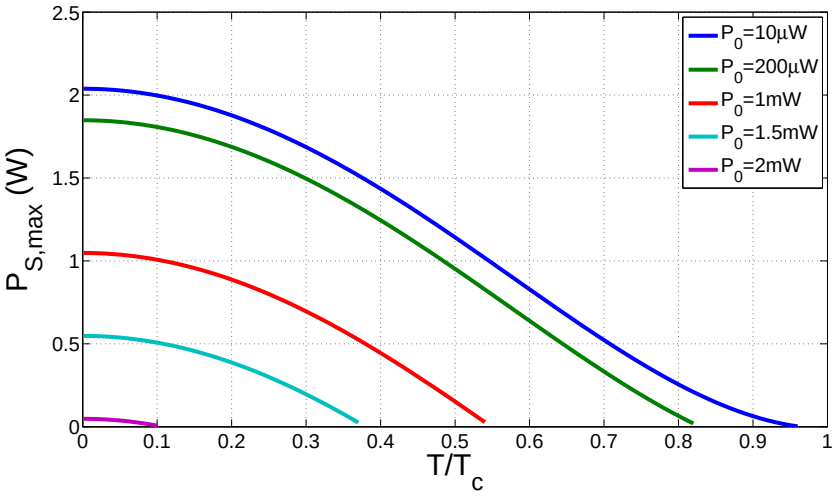

Figure 2.4: Simulation of the maximum allowable incident peak power for the YBCO sample of Table 2.1 with different average incident power.

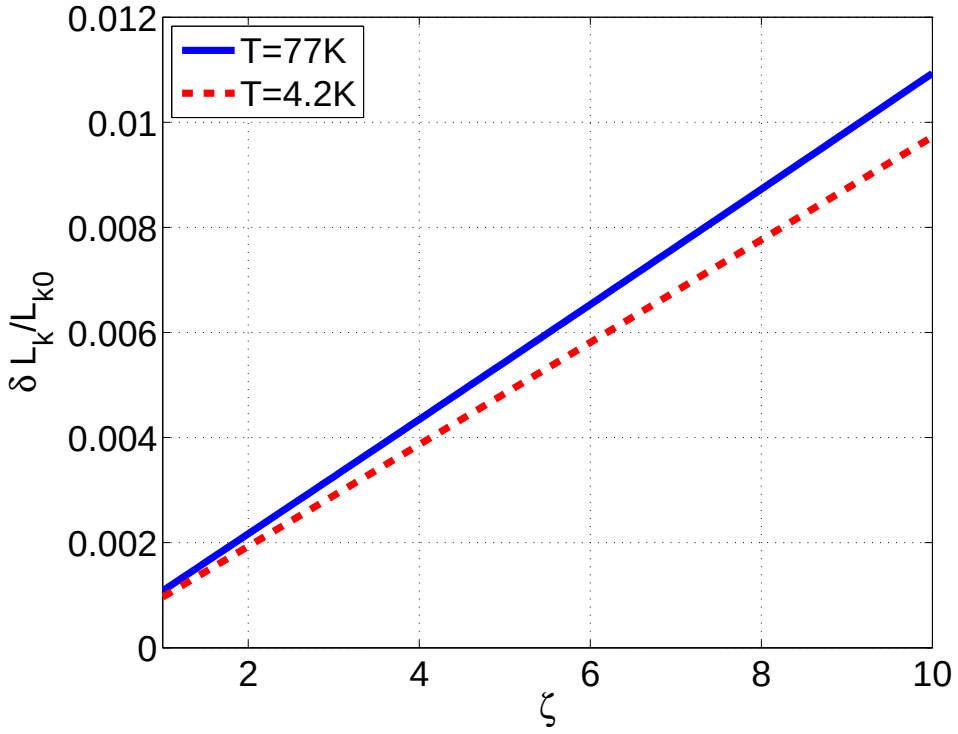

Figure 2.5: Simulation of the relative photoinduced changes in the kinetic inductance of a thin film with the parameters of Table 2.1 as a function of peak-to-average incident power ratio $\zeta = p_{max}/P_0$, at T=77K ($P_0 = 50\mu$W) and T=4.2K ($P_0 = 1$mW).

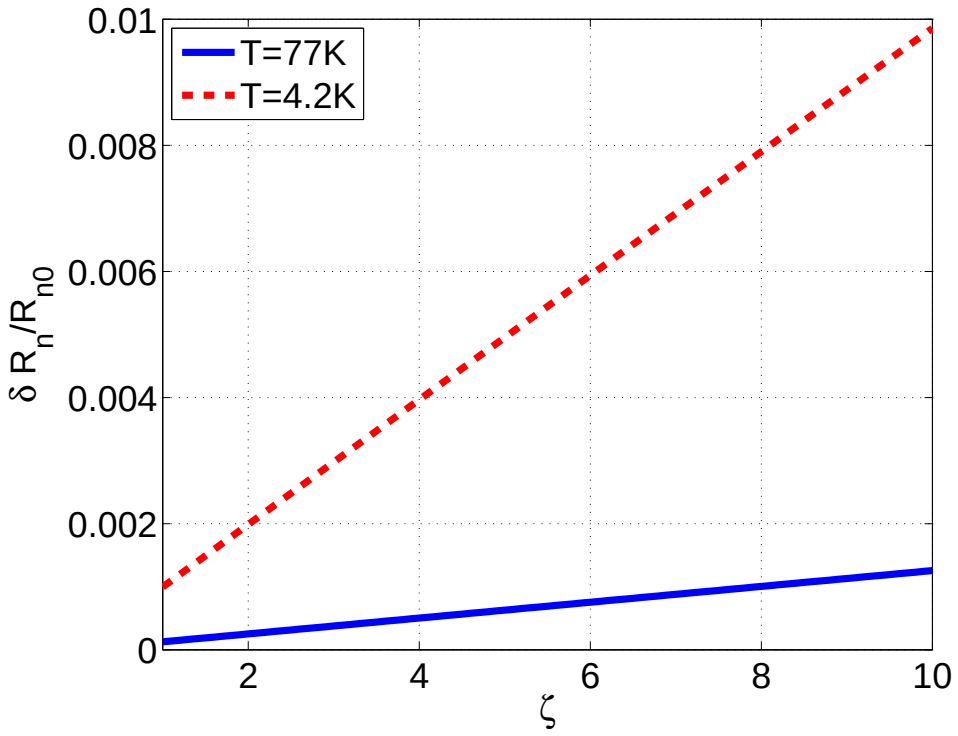

Figure 2.6: Simulation of the relative photoinduced changes in the normal resistance of a thin film with the parameters of Table 2.1 as a function of peak-to-average incident power ratio $\zeta = p_{max}/P_0$, at T=77K ($P_0 = 50\mu$W) and T=4.2K ($P_0 = 1$mW).

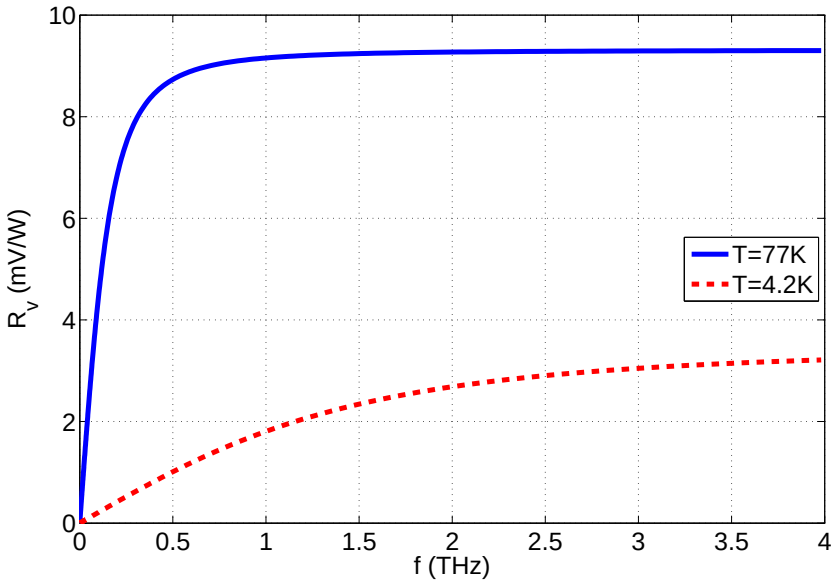

Figure 2.7: Simulation of the kinetic inductive responsivity of a thin film with the parameters of Table 2.1 at T=77K and T=4.2K.

2.5 Experimental Photodetection in YBCO Microstructures

A meander line structure could be used as a simple superconducting photodetector. The meander shape increases the length-to-area ratio, which leads to a better overall responsivity. In order to guide the photogenerated signals, the meander line has been implemented in the middle of a microwave coplanar waveguide (CPW)[11]. Figure 2.8 shows the images of two meander-line structures with 3μm and 5μm line-width, respectively. The devices respectively cover an area of 176μm$\times$201μm and 176μm$\times$195μm. Both the transmission line and the meander structures are made of YBCO.

Figure 2.9 shows the resistance of the YBCO film as a function of the temperature. Clearly, the critical temperature is about 86K. Figure 2.10 depicts the I-V characteristic of the 3μm meander line[12]. Obviously, the critical current for the meander structure is about 5.5mA.

For the photodetection experiment, the device is dc biased, by means of two bias Tees, inside a cryostat. The details about the cryogenic setup can be found in [53]. A 1550nm laser beam is focused on the meander line structure. The laser pulses are Gaussian with a duration of 45ps. One side of the transmission line is matched to prevent the interference of the signal with its reflected replica. The photogenerated signal is amplified by an amplifier with a gain of 100 and a bandwidth of 1.8GHz. Clearly, the photoresponse suffers from the limited bandwidth of the amplifier. The output waveform is then monitored on a 16GHz bandwidth oscilloscope.

The device is first operated with laser pulses at a repetition rate of 1MHz. The total average incident optical power is 3.5mW. Figure 2.11 demonstrates the photoresponse

[11]The microwave properties of the CPW transmission line are addressed in the next chapter in detail.
[12]In the following, it is the 3μm meander line that has been used in photodetection experiments.

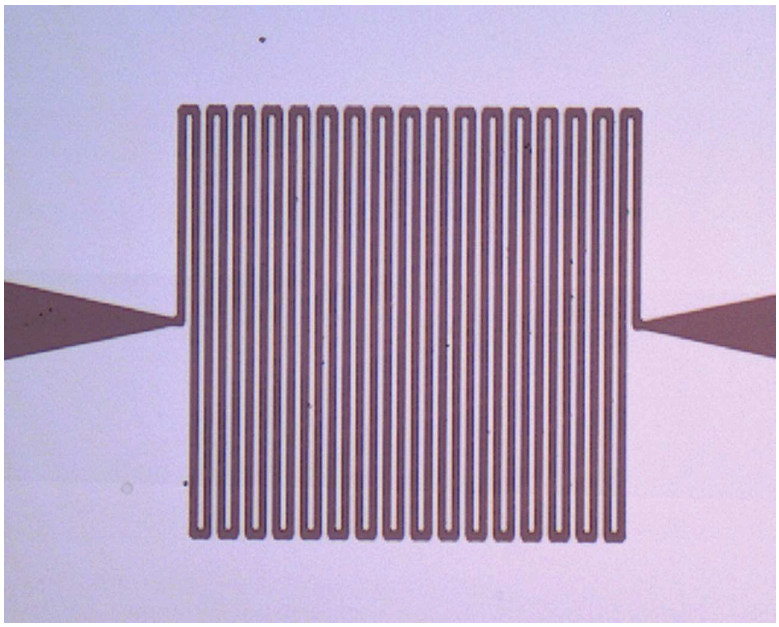

(a)

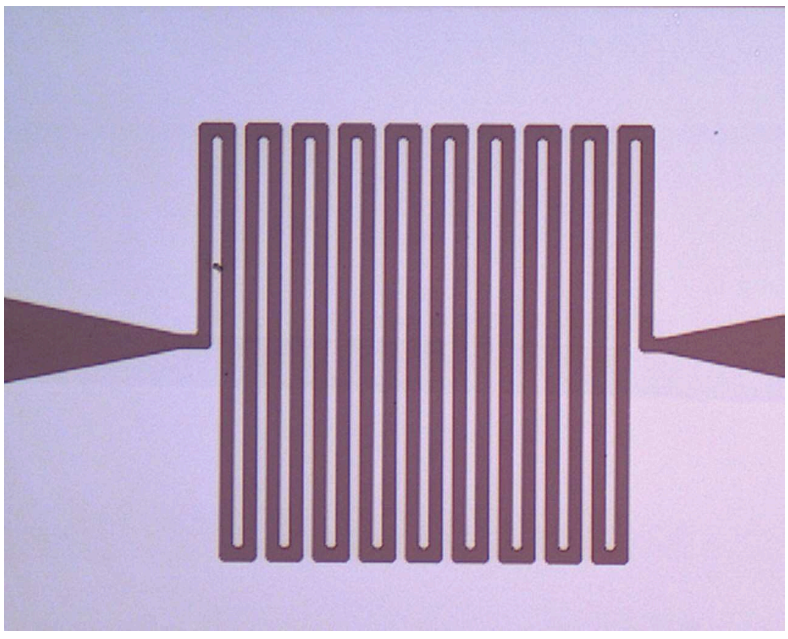

(b)

Figure 2.8: Optical images of YBCO meander line structures with (a) 3μm and (b) 5μm line width.

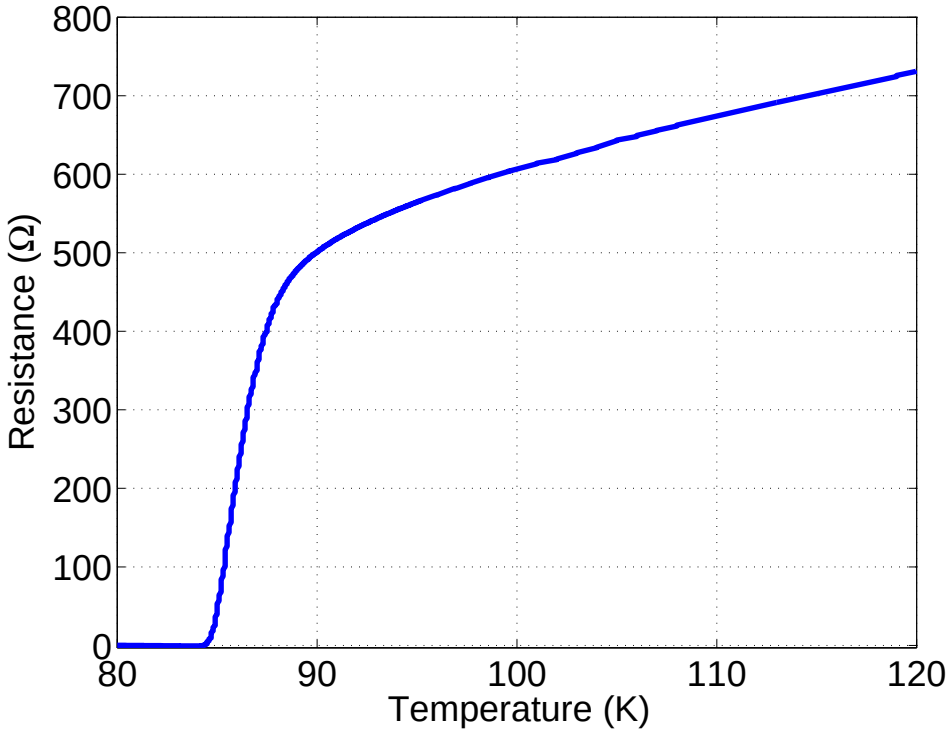

Figure 2.9: Measurement of the YBCO film resistance vs. temperature.

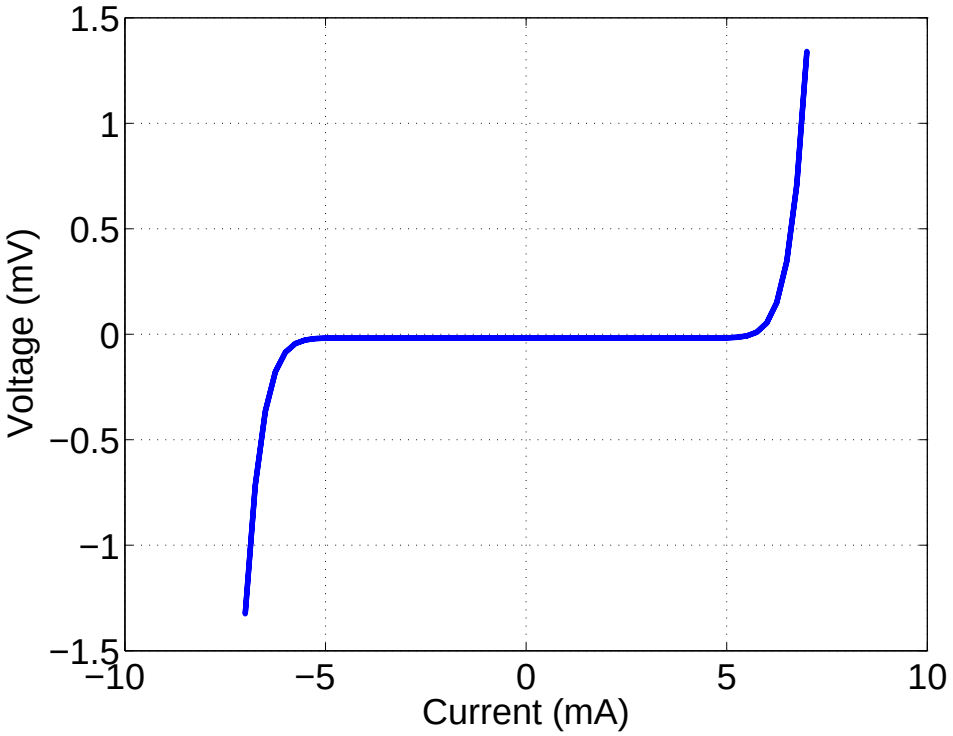

Figure 2.10: The measured I-V characteristic of the 3μm meander structure at 77K.

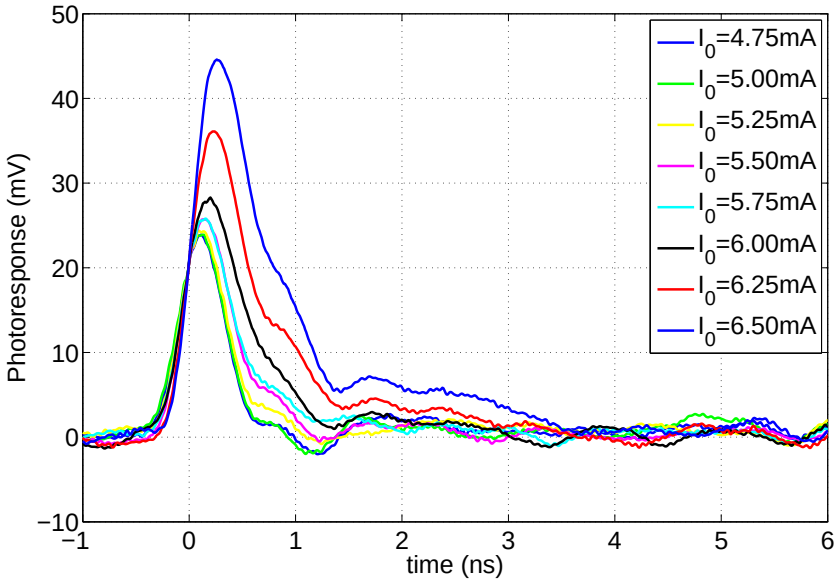

Figure 2.11: Measured photoresponse waveforms of the 3μm meander line structure for different bias currents, at a temperature of 77K.

waveforms for different bias currents from 5mA to 6.5mA.

The detector is next operated at a constant bias current of 5.5mA under different optical powers, where the results are illustrated in Figure 2.12. The photoresponse waveform associated with the 4.9mW incident optical power clearly corresponds to a situation where the whole meander-line structure turns into the normal state as a result of the optical illumination.

One can readily recognize the bipolar photoresponse below the critical current, whereas at or above the critical current the response is unipolar. The negative part of the photoresponse corresponds to the recombination of the quasiparticles and restoration of the Cooper pairs condensate. This feature exactly follows the kinetic-inductive mechanism of Figure 2.2. The linear dependence of the photoresponse amplitude on the bias cur-

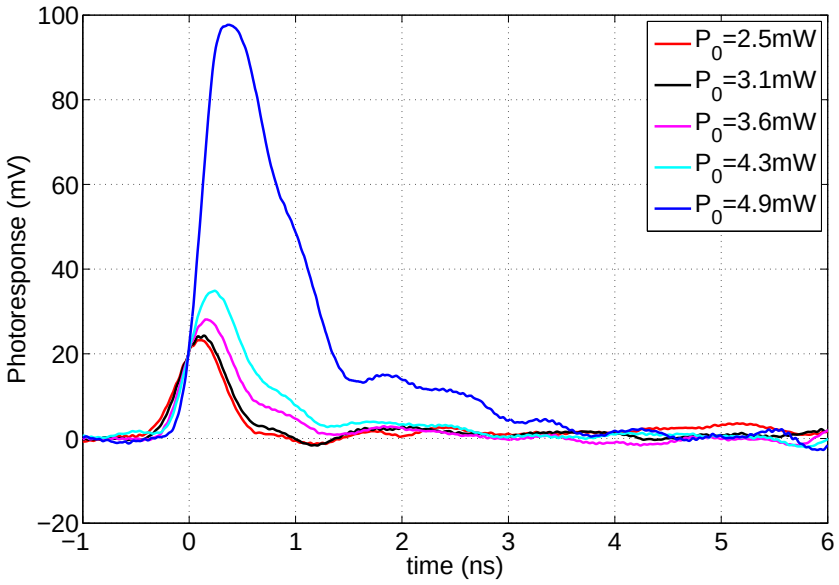

Figure 2.12: Measured photoresponse waveforms of the 3μm meander line structure for different optical powers, with a 5.5mA dc bias at 77K.

Photoresponse	Non-Bolometric		Transition		Bolometric			
Current Bias (mA)	4.75	5.00	5.25	5.50	5.75	6.00	6.25	6.50
Rise Time (ps)	310	340	300	300	310	350	320	310
FWHM (ps)	490	500	500	530	540	630	620	700
Settling Time (ns)	0.88	1.93	1.18	1.24	1.34	1.96	1.66	2.91

Table 2.2: Summary of the measured photoresponse characteristics for the YBCO meander-line of Figure 2.11 at 77K.

rent is evidently illustrated in Figure 2.13, wherein different line slopes distinguish the photoresponse regimes. Table 2.2 summarizes important features of the photoresponse.

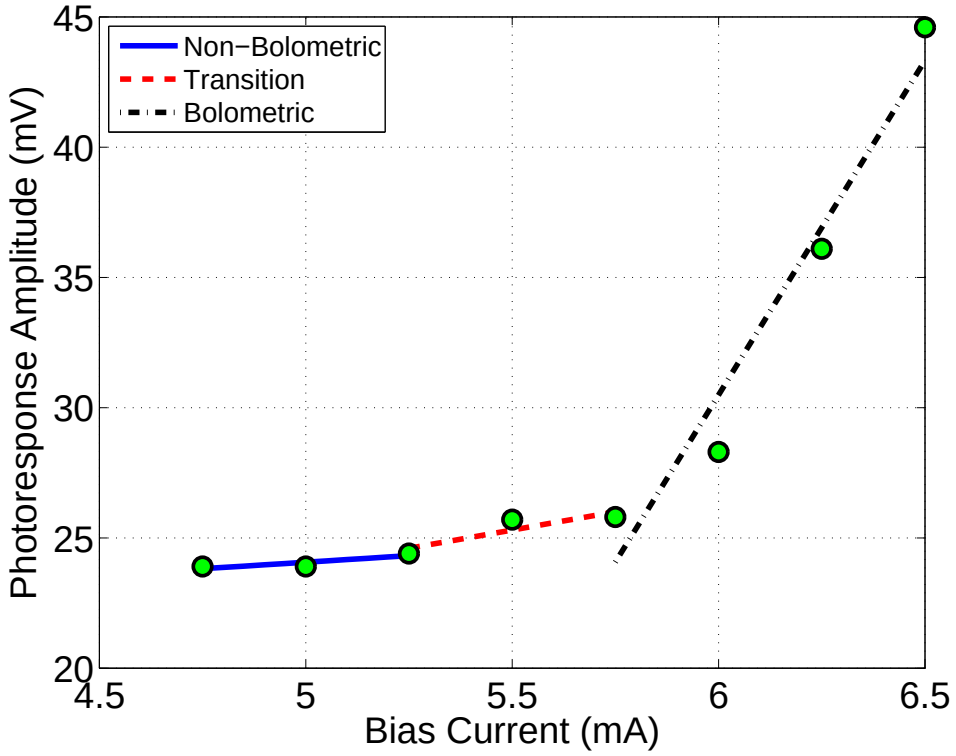

Figure 2.13: Linear dependence of the measured photoresponse amplitudes on the bias current at different regimes.

2.6 Summary

This chapter reviewed the kinetic inductive mechanism of the photoresponse in superconducting thin films based on the two-fluid model. The concept of the kinetic inductance was precisely defined in terms of the stored electromagnetic energy by means of the Poynting theorem, where it was shown that the energy associated with the kinetic energy of Cooper pairs can be accounted for by the so called kinetic inductance L_k of the superconducting structure. The photoresponse mechanism relies on the optically induced variations in the L_k as a result of breaking the Cooper pairs through the absorption of energetic photons, and results in a change in the impedance of the structure and is most conveniently measured as a voltage by applying an external dc current bias. An analytical formulation of the problem was introduced where the photo-generated voltage was calculated in terms of the input optical power and the material parameters. While the responsivity is generally nonlinear, a linearized model of the photoresponse was derived under the small signal assumption. Finally, the photoresponse of sample YBCO meander-line devices were measured under different operating conditions to demonstrate photodetection in the superconducting, transition, and normal regimes.

Chapter 3

Superconducting Microwave and Microwave-Photonic Waveguides

3.1 Introduction

This chapter investigates structures for guiding the photogenerated high-frequency electrical signals in superconducting optoelectronic devices.

A set of superconducting coplanar waveguide (CPW) transmission lines are designed and measured up to a frequency of 50GHz. These transmission lines provide the microwave template for all the devices which are experimentally investigated in this thesis.

Based on the same photoresponse mechanism as presented in chapter 2, microwave properties of a structure may be modulated by means of an external optical signal. This method is experimentally demonstrated to be useful for the implementation of microwave-photonic devices. In particular, two optically tunable microwave devices are measured, namely a tunable resonator and a tunable delay line.

Slot Width (μm)	Measured Attenuation (dB/mm)					
	1GHz	5GHz	10GHz	20GHz	40GHz	50GHz
94	0.003	0.026	0.043	0.074	0.121	0.211
97	0.005	0.027	0.042	0.507	0.121	0.142
100	0.009	0.031	0.046	0.065	0.125	0.155
103	0.004	0.025	0.041	0.062	0.137	0.153
107	0.015	0.033	0.049	0.069	0.129	0.192

Table 3.1: The measured insertion loss for the CPW transmission lines of Figure 3.1a and 3.1b at some sample frequencies.

3.2 Design and Measurement of YBCO Microwave Transmission Lines

Successful operation of an optoelectronic device requires low-loss and low-dispersion propagation of the photogenerated signals to the output port(s). At RF/microwave frequencies, this requirement can be suitably met through the integration of the active region with a microwave transmission line. To this end, a set of CPW transmission lines have been designed and measured to ensure proper propagation of the electrical signals along the device. Microwave probes are used to accurately and reliably read the high-frequency signals out of the transmission lines. The transmission lines are made of a 100nm thick YBCO film on top of an LAO substrate with gold patches at the ends, which provide good contacts between the probe tips and the device. According to the analysis of superconducting transmission lines in [54], the width of the center strip is designed to be 60μm with different slot size between the ground lines and the center signal strip. The results of the S-parameter measurements, at a temperature of T=77K, are illustrated in Figure 3.1. Table 3.1 summarizes the measurements at some specific frequencies.

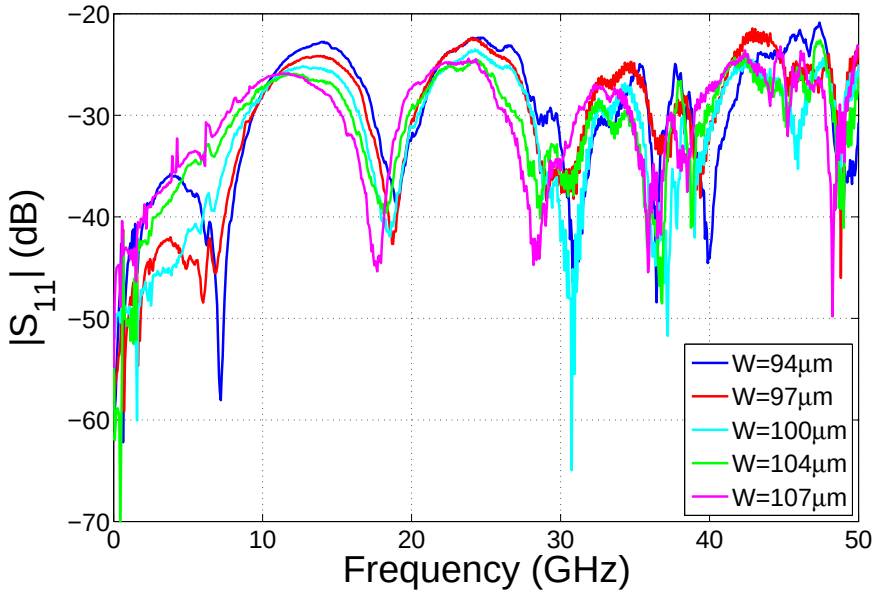

(a)

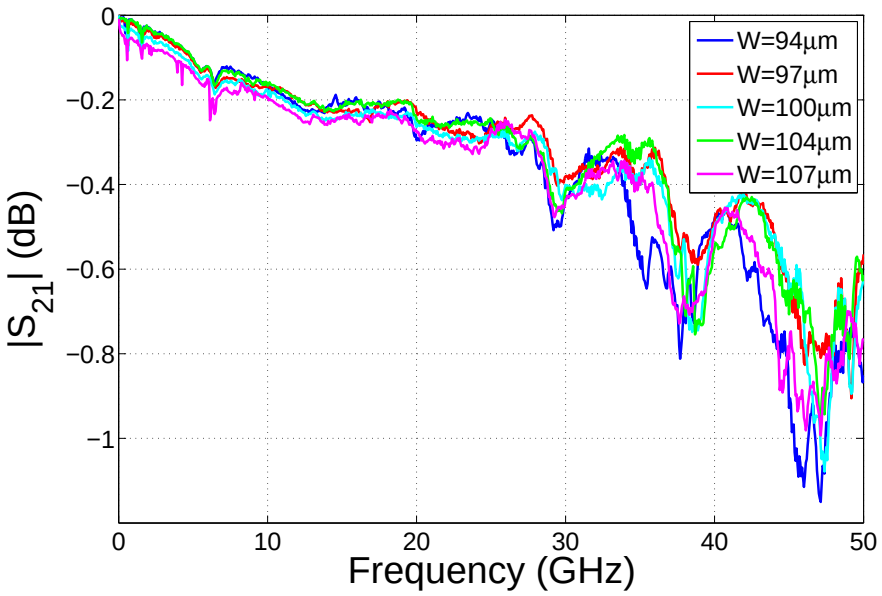

(b)

Figure 3.1: The measured magnitude of (a) S_{11} and (b) S_{21} for 4mm-long YBCO CPW transmission lines with a 100nm-thick YBCO film and 60μm-wide center strip on an LAO substrate with different slot size, at a temperature of 77K.

3.3 Experimental Demonstration of Superconducting Microwave-Photonic Devices

Microwave properties of a superconducting structure may be controlled by an external optical signal, based on the photoresponse mechanism introduced in the previous chapter. This technique can be used to implement optically tunable microwave devices. In the following, a meander-line structure embedded in the middle of a CPW transmission line, is experimentally shown to be capable of serving as a microwave-photonic device. The supporting transmission line is one of the characterized CPWs in the previous section, with the 107μm slot width.

Optical radiation changes the kinetic inductance of the meander-line structure. This change results in a shift in the resonance frequency of the structure. Therefore, by adjusting the average incident optical power, one can optically tune the resonance frequency of the meander-resonator. Figure 3.2 and Figure 3.3 depict the measured S-parameter of the device under different levels of optical illumination.

As Figure 3.4 illustrates, the frequency shift linearly varies with the incident optical power. For the 3μm and 5μm meander lines, the slope of variations is -66.9 GHz/W and -81.4 GHz/W respectively. The negative sign shows that the resonance frequency shifts toward lower frequencies at a higher optical power. This effect is attributed to the increase in the kinetic inductance as a result of pair breaking. The increase in the kinetic inductance is accompanied by an increase in the normal conductance of the device due to the photogenerated excess quasiparticles. Therefore, optical pair breaking reduces the contribution of the inductive channel to the microwave signal transmission and accentuates the role of the normal channel. The increase in the device insertion loss with incident optical power clearly illustrates this fact; and is shown in Figure 3.5. The photoinduced loss is 40.2

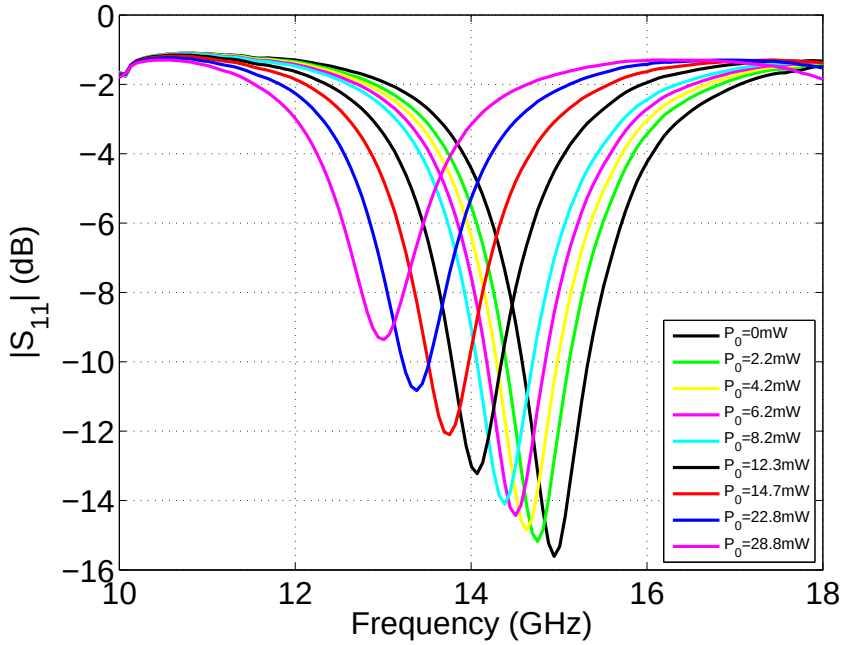

(a)

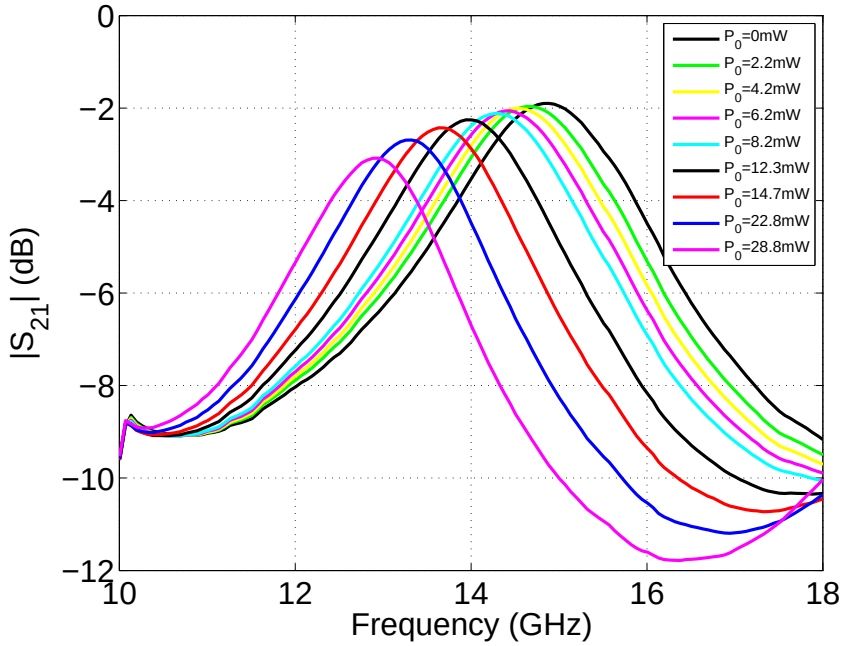

(b)

Figure 3.2: The measured S-parameters for the 3μm meander line structure under different incident optical power, at a temperature of 77K.

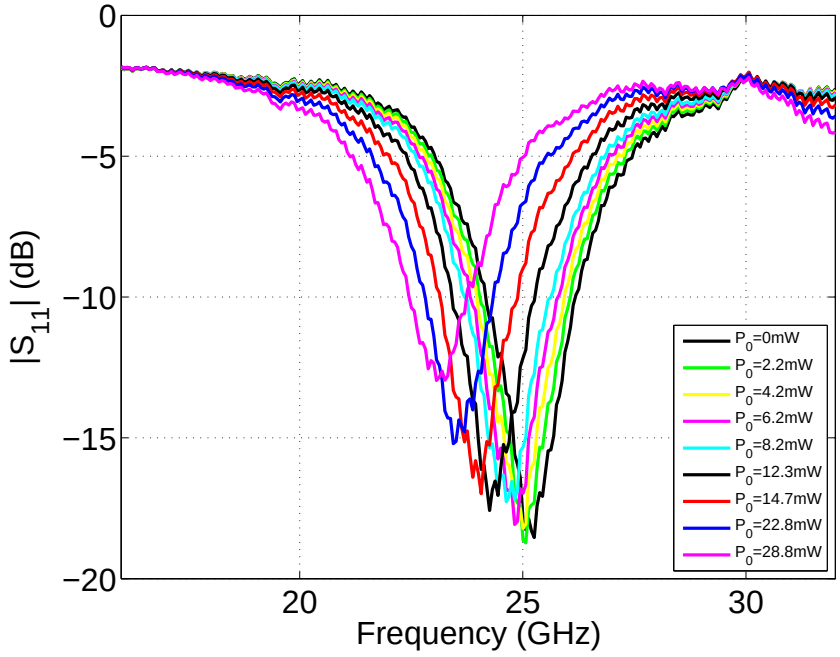

(a)

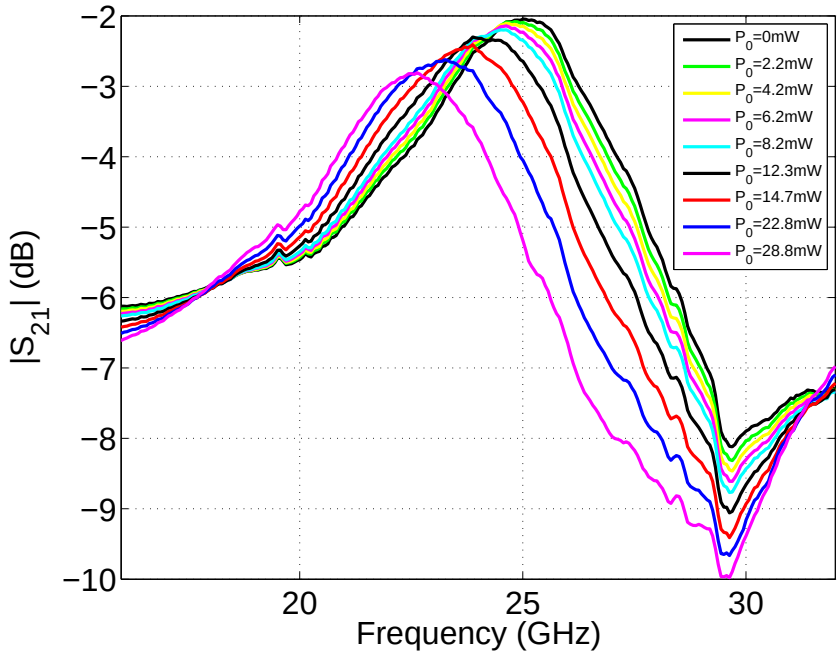

(b)

Figure 3.3: The measured S-parameters for the 5μm meander line structure under different incident optical power, at a temperature of 77K.

Meander Line Feature Size (μm)	Resonance Frequency Shift (GHz/mW)	Excess Insertion Loss (dB/mW)	Phase Shift (deg/mW)
3	-1.34	0.80	-65.6
5	-1.63	0.54	-31.0

Table 3.2: The measured performance of the meander line structures as microwave-photonic devices.

dB/W and 27.2 dB/W for the 3μm and 5μm meander lines, respectively. Consequently, the quality factor of the resonator decreases at a higher incident optical power. This effect is evident from the broadening of the resonance with the incident optical power in Figure 3.2 and Figure 3.3.

The photoinduced change in the kinetic inductance also modifies the signal transmission phase. Therefore, at a given frequency, the device may function as a tunable delay line. Figure 3.6 shows the variation of the signal transmission phase with incident optical power. Clearly the phase shift is not constant over the whole frequency range; thus, for a signal with an extended bandwidth the device may be used for waveform generation. However, if the signal is narrowband the device perfectly serves as a delay line. Figure 3.7 illustrates the linear dependence of the photoinduced phase shift on the incident optical power. The slope of variations is -3.28 (deg/mW) and -1.55 (deg/mW) for the 3μm and 5μm meander lines, respectively.

Table 3.2 summarizes the performance of the meander line structures as microwave-photonic devices, based on a 5% optical coupling efficiency.

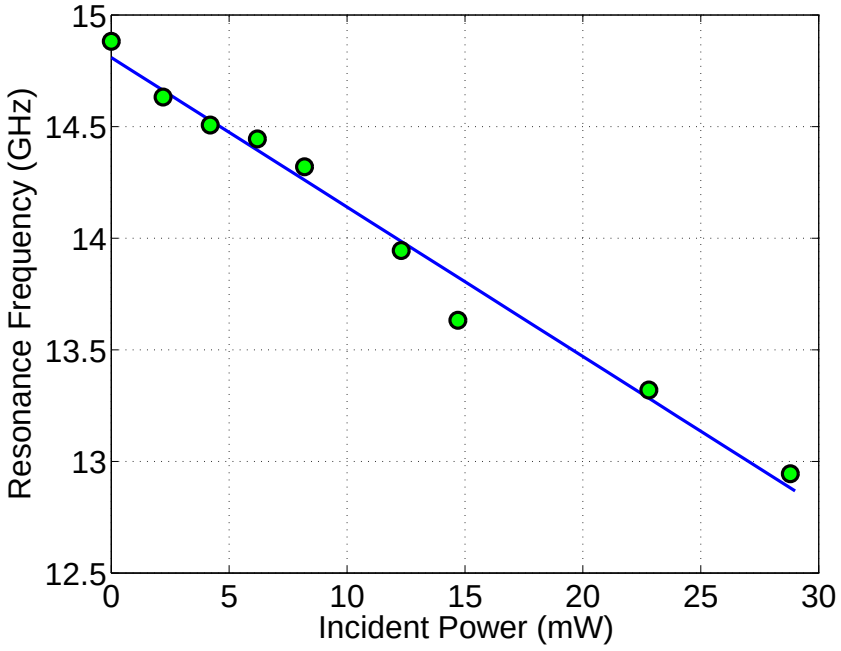

(a)

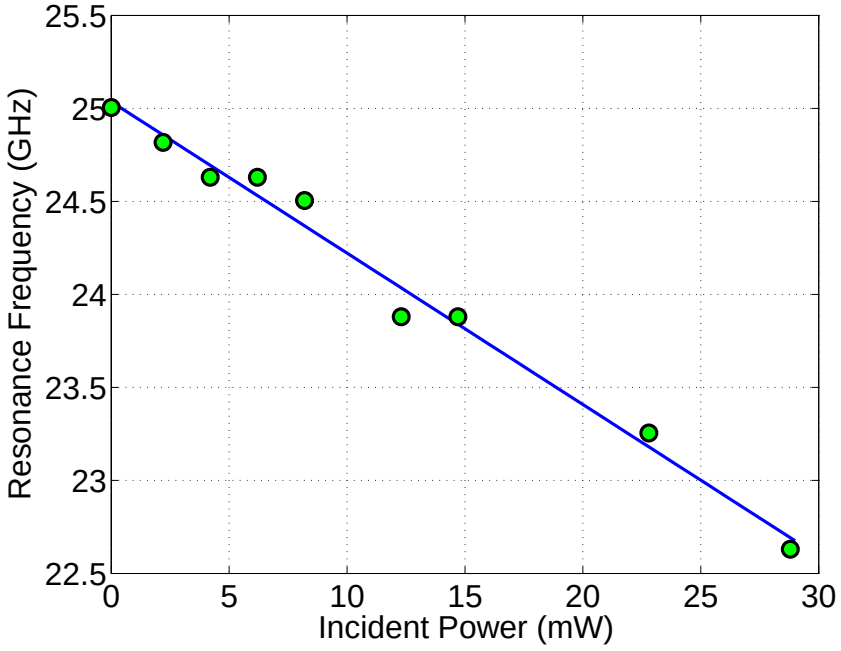

(b)

Figure 3.4: Measured resonance frequency versus the incident optical power for the (a) 3μm and (b) 5μm meander line structure, at a temperature of 77K.

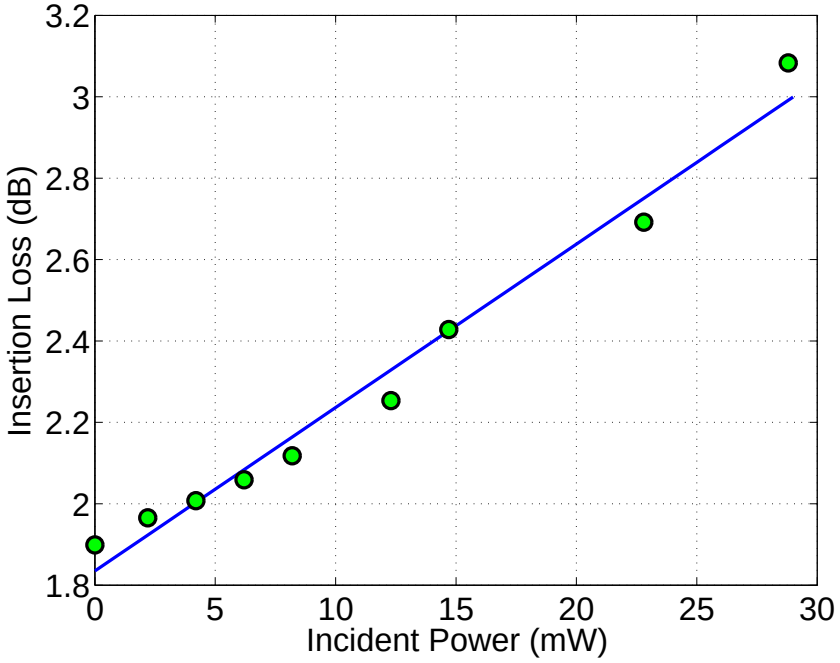

(a)

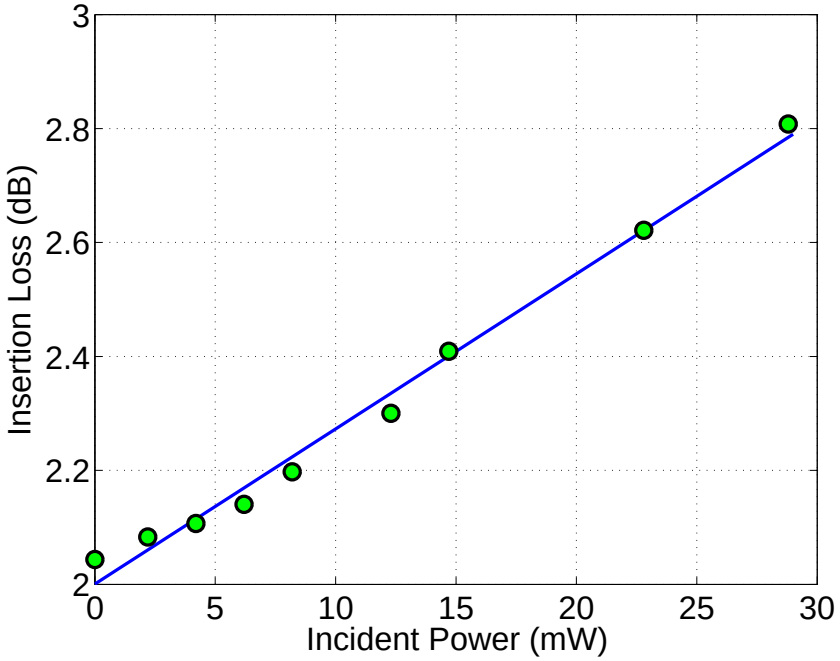

(b)

Figure 3.5: Measured insertion loss versus the incident optical power for the (a) 3μm and (b) 5μm meander line structure, at a temperature of 77K.

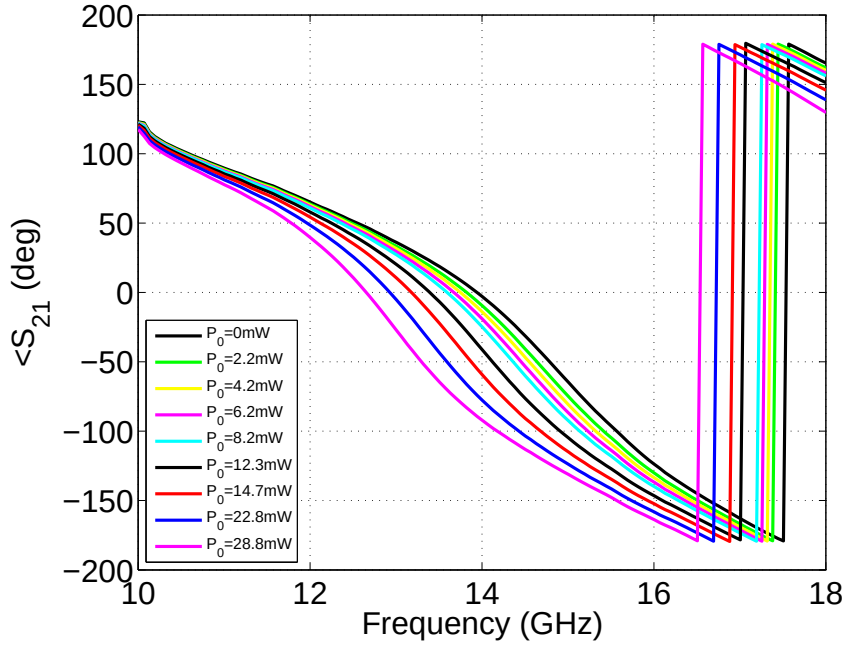

(a)

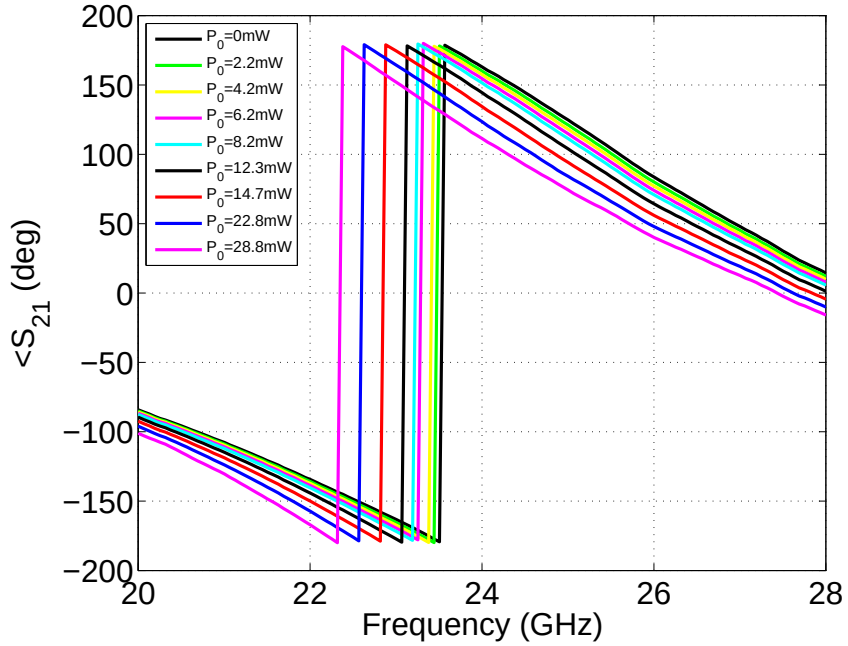

(b)

Figure 3.6: Variation of the measured signal transmission phase with incident optical power for the (a) 3μm and (b) 5μm meander line structure, at a temperature of 77K.

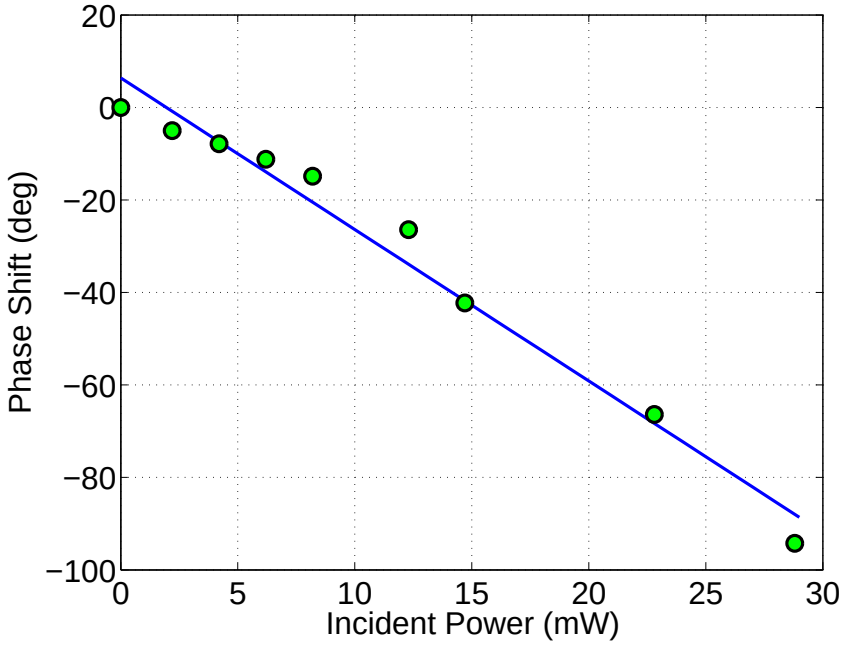

(a)

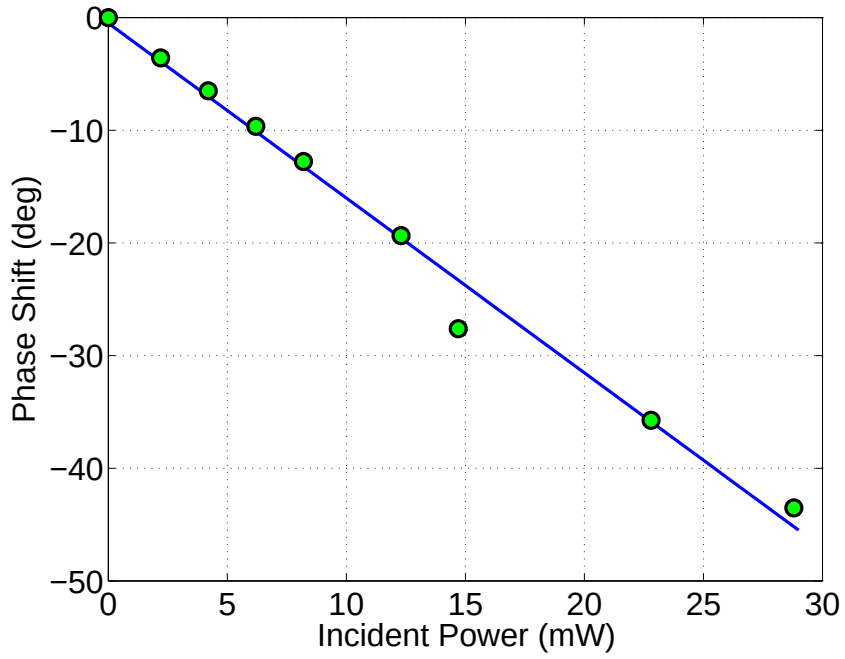

(b)

Figure 3.7: Measured transmission phase shift as a function of incident optical power, at a temperature of 77K, for the (a) 3μm and (b) 5μm meander line structure, respectively at f=20GHz and f=26GHz.

3.4 Summary

This chapter demonstrated the design and measurement of several microwave and microwave-photonic devices. A set of YBCO CPWs on LAO substrate were designed and fabricated whose S-parameters measurement showed insertion and reflection losses respectively less than 0.22dB/mm and greater than 20dB up to a frequency of 50GHz. Then, devices comprising of YBCO meander-line structures in the middle of a CPW were measured for microwave-photonic applications. The tunable resonators with 3μm and 5μm meander lines exhibited -66.9 GHz/W and -81.4 GHz/W frequency tunability ratios and 40.2 dB/W and 27.2 dB/W photoinduced loss factors, respectively. The tunable phase shifters with 3μm and 5μm meander lines respectively showed -3.28 (deg/mW) and -1.55 (deg/mW) phase tunability ratios.

Chapter 4

Millimeter-Wave and Terahertz Transmission Lines based on Surface Waves in Plasmonic Waveguides

4.1 Introduction

Low-loss, quasi-TEM and low-dispersion propagation of THz waves has been experimentally demonstrated in both air-filled parallel-plate waveguides (AF-PPWGs) [55, 56] and dielectric-filled parallel-plate waveguides (DF-PPWGs) [57, 58]. PPWGs have been used in two-dimensional interconnect layers [59], planar quasi optics [60], transmitters [61], generators [62] and photonic crystal filters [63] for applications ranging from the study of whispering-gallery modes [64] and photonic crystals [65] to biosensing [66] and guided-wave spectroscopy [67].

It is well-known that metal-dielectric surface waveguides (MD-SWs) also support the propagation of electromagnetic waves in the form of surface plasmon polariton (SPP) modes

[68,69], ranging from visible and near infrared [70–72] to far infrared and THz region of the spectrum [73, 74]. While the propagation along MD-SWs is highly dissipative at optical wavelengths, low-loss propagation of visible and near infrared waves is achievable based on the long-rang surface plasmon polaritons (LRSPPs) in such structures as symmetrically loaded metal slabs [75, 76] and strips [77] as well as metal-clad waveguides [78]. However, at THz and far infrared wavelengths, SPPs benefit from low-loss propagation along the metal-dielectric waveguides, which has been the subject of study in recent years [79, 80].

The low-loss and quasi-TEM nature of THz wave propagation in PPWGs and MD-SWs, provokes the idea of employing the transmission line theory to study these structures, which enables circuit-like techniques to be used for the analysis and design of THz devices and components, in particular, THz optoelectronic devices, such as traveling-wave photomixers [81–84] and detectors [85, 86].

MD-SWs, in general, are not regarded as practical structures for guiding THz waves due to the poor confinement of the fields to the surface, arising from the Zenneck-wave nature of the propagation. Nevertheless, aside from its theoretical importance, the metal layer can be replaced by a doped-semiconductor [73,74,87,88] to provide better confinement. The same arguments hold if corrugated surfaces that mimic SPP behavior for THz regime [89, 90] are used rather than the flat metallic surface. Moreover, it will be shown that the low-loss and quasi-TEM propagation in PPWGs is due to resonant excitations of SPPs at the two metal-dielectric boundaries. Therefore, the behavior of PPWGs can be best understood, in the THz regime, as two coupled MD-SWs that serve as the basic elements of any planar THz plasmonic passive element. Therefore, the rest of this chapter develops transmission line models for MD-SWs and PPWGs, based on their full-wave field solutions.

4.2 Surface Waves at the Boundary of Two Semi-infinite Media

Figure 4.1 shows the interface of two semi-infinite media consisting of linear, isotropic and homogenous materials. For an electromagnetic wave propagating along the z-direction, Maxwell's equations may be more conveniently written in terms of the longitudinal and transverse field components and operators,

$$\nabla_t \times \mathbf{E}_z + \mathbf{z} \times \frac{\partial \mathbf{E}_t}{\partial z} = -\mu \frac{\partial \mathbf{H}_t}{\partial t}, \tag{4.1a}$$

$$\nabla_t \times \mathbf{E}_t = -\mu \frac{\partial \mathbf{H}_z}{\partial t}, \tag{4.1b}$$

$$\nabla_t \times \mathbf{H}_z + \mathbf{z} \times \frac{\partial \mathbf{H}_t}{\partial z} = \epsilon \frac{\partial \mathbf{E}_t}{\partial t}, \tag{4.1c}$$

$$\nabla_t \times \mathbf{H}_t = \epsilon \frac{\partial \mathbf{E}_z}{\partial t}, \tag{4.1d}$$

where $\nabla_t = \mathbf{x} \times \frac{\partial}{\partial x} + \mathbf{y} \times \frac{\partial}{\partial y}$. Since there is no variation in the geometry and the field distribution along the y-axis, i.e. $\frac{\partial}{\partial y} = 0$, the solutions of Maxwell's equations are divided into TE and TM polarizations. In general, the nonzero field components are of the form of (ψ_y, ψ_x, ψ_z), which corresponds to (E_y, H_x, H_z) and (H_y, E_x, E_z) for TE and TM waves respectively. Assuming a time-harmonic field,

$$\psi_y(x, z; t) = \psi(x) e^{j(\omega t - \gamma z)}, \tag{4.2a}$$

$$\psi_x(x, z; t) = \frac{-\gamma \xi}{\omega \mu} \psi(x) e^{j(\omega t - \gamma z)}, \tag{4.2b}$$

$$\psi_z(x, z; t) = \frac{j\xi}{\omega \mu} \frac{d\psi(x)}{dx} e^{j(\omega t - \gamma z)}, \tag{4.2c}$$

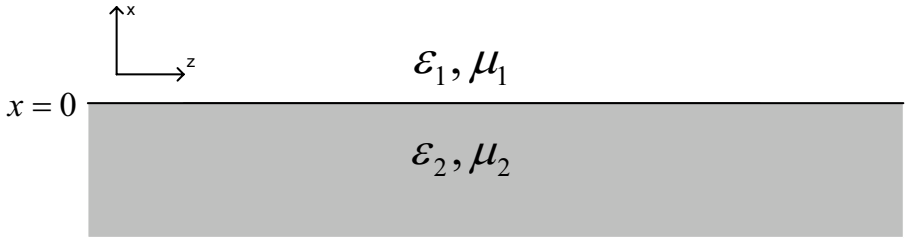

Figure 4.1: The interface of two semi-infinite media.

where $\xi = 1$ for TE waves and $\xi = (-\mu/\epsilon)$ for TM waves. The wavefunction $\psi(x)$, satisfies the one-dimensional wave equation

$$\left[\frac{d^2}{dx^2} + (\omega^2\mu\epsilon - \gamma^2)\right]\psi(x) = 0. \tag{4.3}$$

Since the two media are semi-infinite, the wavefunction $\psi(x)$ must vanish at infinity, i.e. $\psi(\pm\infty) = 0$. Hence,

$$\psi(x) = \begin{cases} Ae^{-\kappa_1 x}, & \text{for } x > 0 \\ Be^{\kappa_2 x}, & \text{for } x < 0 \end{cases} \tag{4.4}$$

where $\kappa_i = \pm\sqrt{\gamma^2 - \omega^2\mu_i\epsilon_i}$ and the sign is chosen such that $\Re e\{\kappa_i\} > 0$, in both media. The mode condition follows from applying the boundary conditions at $x = 0$

$$\frac{\kappa_1}{\mu_1} + \frac{\kappa_2}{\mu_2} = 0, \qquad \text{for TE waves,} \tag{4.5a}$$

$$\frac{\kappa_1}{\epsilon_1} + \frac{\kappa_2}{\epsilon_2} = 0, \qquad \text{for TM waves.} \tag{4.5b}$$

4.3 Metal-Dielectric Surface Waveguide

Consider the plasma-dielectric boundary, where the permittivity of the dielectric and the plasma are ϵ_1 and ϵ_2 respectively. Because both media are nonmagnetic, i.e. $\mu_1 = \mu_2 = \mu_0$, the mode condition (4.5a) has no solutions. Therefore, the plasma-dielectric does not support any TE surface wave. However, for plasmas $\Re e\{\epsilon_2\} < 0$, the interface supports a TM surface wave whose longitudinal propagation constant γ is

$$\gamma = \omega\sqrt{\frac{\mu_0\epsilon_1\epsilon_2}{\epsilon_1 + \epsilon_2}}, \tag{4.6}$$

and consequently,

$$\kappa_i = \omega\sqrt{\frac{-\mu_0\epsilon_i^2}{\epsilon_1 + \epsilon_2}}. \tag{4.7}$$

Generally, the propagation constant is a complex number $\gamma = \beta - j\alpha$, where β is the phase constant and α is the attenuation constant. If $|\epsilon_2| \gg |\epsilon_1|$, then [68]

$$\beta \simeq \omega\sqrt{\mu_0\epsilon_1} = \beta_0 n_1, \tag{4.8a}$$

$$\alpha \simeq \beta\frac{\epsilon_1\epsilon_2''}{2|\epsilon_2|^2}, \tag{4.8b}$$

$$\kappa_i \simeq \beta\sqrt{\frac{-\epsilon_i^2}{\epsilon_1\epsilon_2}}, \tag{4.8c}$$

where $\beta_0 = \omega\sqrt{\mu_0\epsilon_0}$, $n_1 = \sqrt{\epsilon_1/\epsilon_0}$, and $\epsilon_2 = \epsilon_2' - j\epsilon_2''$.

It is well known that metals exhibit plasma characteristics below their plasma frequency, which normally lies within the ultraviolet(UV) part of the electromagnetic spectrum. Therefore, metal-dielectric interfaces are capable of guiding electromagnetic waves along their boundaries [68, 70–72]. This property has led to the introduction of plasmonic

Table 4.1: The complex refractive index of gold, silica and silicon at different wavelengths [1–3].

Wavelength	Gold (Au)		Silica (SiO_2)		Silicon (Si)	
$\lambda(\mu m)$	n	k	n	k	n	k
1.55	0.599	9.81	1.45	-	3.48	1×10^{-2}
30	56.6	192	2.45	0.12	3.68	4.8×10^{-2}
269	521	598	1.96	4×10^{-5}	3.74	8×10^{-2}

Table 4.2: Simulated characteristics of the gold-dielectric surface wave for different dielectrics and wavelengths.

Waveguides	$\lambda(\mu m)$	$f(THz)$	β/β_0	α/β_0	L_{eff}	δ_1/λ	δ_2/λ
Au-Air	1.55	193.5	1.0052	5.97×10^{-4}	$206\mu m$	0.78	8.07×10^{-3}
Au-Air	30	10	$1 + 1 \times 10^{-5}$	6.77×10^{-6}	$35.27cm$	16.61	4.14×10^{-4}
Au-Air	269	1.1	$1 + 1 \times 10^{-7}$	7.87×10^{-7}	$27.20m$	83.72	1.33×10^{-4}
Au-SiO_2	1.55	193.5	1.4659	0.0019	$67\mu m$	0.37	8.02×10^{-3}
Au-SiO_2	30	10	2.4501	0.1301	$18.35\mu m$	2.86	4.14×10^{-4}
Au-SiO_2	269	1.1	1.9600	5.93×10^{-6}	$3.61m$	21.79	1.33×10^{-4}
Au-Si	1.55	193.5	3.7188	0.0425	$2.9\mu m$	0.06	7.59×10^{-3}
Au-Si	30	10	3.4804	0.0103	$232\mu m$	1.37	4.14×10^{-4}
Au-Si	269	1.1	3.7400	0.0800	$267\mu m$	6.22	1.33×10^{-4}

optical waveguides, which can confine optical power to the vicinity of the guiding surface. At visible and near infrared (NIR) wavelengths, even sub-wavelength confinement is achievable, however at the far-infrared (FIR) domain, confinement to the surface is very poor. For example, consider the gold-dielectric boundary at three different wavelengths $\lambda_a = 1.55\mu m$, $\lambda_b = 30\mu m$ and $\lambda_c = 269\mu m$, with the complex refractive indices listed in Table 4.1. The characteristics of the surface wave associated with this interface are listed in Table 4.2. The penetration depth δ_i measures the field confinement.

Table 4.2 clearly shows that the field penetrates less into the metal at a longer wavelength, which results in lower dissipation, and the confinement weakens. Interestingly the

long-wavelength surface waves are quasi-TEM. It is readily found that

$$\frac{|E_{x1}|}{|E_{z1}|} = \sqrt{\frac{|\epsilon_2|}{|\epsilon_1|}}. \tag{4.9}$$

At THz frequencies, $|\epsilon|$ is usually much greater for metals than for dielectrics. Therefore, the surface wave may be very well approximated as a quasi-TEM wave and a transmission line approach may be applied to THz plasmonic waveguides.

4.4 MD-SW Transmission Line

Explicit expressions for the field components of the surface wave read

$$\mathbf{H}_1 = (0, 1, 0)e^{-\kappa_1 x}e^{j(\omega t - \gamma z)}, \tag{4.10a}$$

$$\mathbf{E}_1 = (\frac{\gamma}{\omega\epsilon_1}, 0, \frac{j\kappa_1}{\omega\epsilon_1})e^{-\kappa_1 x}e^{j(\omega t - \gamma z)}, \tag{4.10b}$$

$$\mathbf{H}_2 = (0, 1, 0)e^{\kappa_2 x}e^{j(\omega t - \gamma z)}, \tag{4.10c}$$

$$\mathbf{E}_2 = (\frac{\gamma}{\omega\epsilon_2}, 0, \frac{-j\kappa_2}{\omega\epsilon_2})e^{\kappa_2 x}e^{j(\omega t - \gamma z)}. \tag{4.10d}$$

Voltage

The surface mode at the metal-dielectric interface is a TM wave; therefore, equation (4.1b) yields

$$\nabla_t \times \mathbf{E}_t = 0, \tag{4.11}$$

which enables to define the potential Φ_t as a solution of the Poisson equation

$$\nabla_t^2 \Phi_t = -\nabla_t . \mathbf{E}_t. \tag{4.12}$$

The solution of (4.12) subjected to the boundary condition $\Phi_t(\pm\infty) = 0$ is

$$\Phi_t(x) = \begin{cases} \frac{\gamma}{\omega\epsilon_1\kappa_1} e^{-\kappa_1 x}, & \text{for } x > 0, \\ \frac{-\gamma}{\omega\epsilon_2\kappa_2} e^{\kappa_2 x}, & \text{for } x < 0. \end{cases} \tag{4.13}$$

The discontinuity of the potential at the metal boundary, clearly shows the presence of surface charges. The voltages at the two sides of the metal-dielectric interface are

$$V_1 \equiv \Phi_t(0^+) = \frac{\gamma}{\omega\epsilon_1\kappa_1}, \tag{4.14a}$$

$$V_2 \equiv \Phi_t(0^-) = \frac{-\gamma}{\omega\epsilon_2\kappa_2}. \tag{4.14b}$$

Therefore, the voltage at each point along the transmission line is

$$V(z) = V_0 e^{j(\omega t - \gamma z)}, \tag{4.15}$$

where

$$V_0 \equiv V_1 - V_2 = \frac{\gamma}{\omega}\left(\frac{1}{\epsilon_1\kappa_1} + \frac{1}{\epsilon_2\kappa_2}\right). \tag{4.16}$$

From (4.8c), it is found that $|\kappa_2|/|\kappa_1| = |\epsilon_2|/\epsilon_1|$. According to the condition of quasi-TEM approximation, i.e. $|\epsilon_2| \gg |\epsilon_1|$, one finds that $|V_2| \ll |V_1|$, thereby the second term in (4.16) can be neglected and $V_0 \simeq V_1$.

Current

For SPP modes, the flow of current is due to the coherent charge waves at the surface of the metal, rather than conduction. This fact is accounted for by considering that the current

and charge densities in the matter are associated with the polarization vector [74, 91]

$$\mathbf{P}_i = \mathbf{D}_i - \epsilon_0 \mathbf{E}_i = (\epsilon_i - \epsilon_0)\mathbf{E}_i, \tag{4.17}$$

and

$$\mathbf{J}_i = \frac{\partial \mathbf{P}_i}{\partial t}, \tag{4.18}$$

$$\rho_i = -\nabla.\mathbf{P}_i. \tag{4.19}$$

Applying (4.18) to (4.10b) and (4.10d)

$$\mathbf{J_1} = (\epsilon_1 - \epsilon_0)(\frac{j\gamma}{\epsilon_1}, 0, \frac{-\kappa_1}{\epsilon_1})e^{-\kappa_1 x}e^{j(\omega t - \gamma z)}, \tag{4.20a}$$

$$\mathbf{J_2} = (\epsilon_2 - \epsilon_0)(\frac{j\gamma}{\epsilon_2}, 0, \frac{\kappa_2}{\epsilon_2})e^{\kappa_2 x}e^{j(\omega t - \gamma z)}. \tag{4.20b}$$

Hence, the current in longitudinal direction for width W of the surface waveguide is

$$I(z) = W\left(\int_{-\infty}^{0} J_{z2}(x)dx + \int_{0}^{+\infty} J_{z1}(x)dx\right) = I_0 e^{j(\omega t - \gamma z)}, \tag{4.21}$$

where

$$I_0 \equiv \epsilon_0 \left(\frac{\epsilon_2 - \epsilon_1}{\epsilon_1 \epsilon_2}\right) W. \tag{4.22}$$

4.4.1 Line Parameters

Characteristic Impedance

The characteristic impedance of the line is defined as $Z_c \equiv V(z)/I(z)$. Therefore,

$$Z_c = \frac{1}{\omega W}\left(\frac{\epsilon_1+\epsilon_2}{\epsilon_0\epsilon_2}\right)\sqrt{\frac{-\epsilon_2}{\epsilon_1}}, \tag{4.23a}$$

$$\simeq \frac{1}{\epsilon_0\omega W}\sqrt{\frac{-\epsilon_2}{\epsilon_1}}. \tag{4.23b}$$

For example the characteristic impedance of the Au-air surface waveguide with $W = 1mm$ is $(101 - j345)\Omega$ and $(8.4 - j9.6)K\Omega$, respectively at $\lambda_b = 30\mu m$ (10THz) and $\lambda_c = 269\mu m$ (1.1THz).

Shunt Admittance and Series Impedance

By examining (4.19), it is readily found that $\rho(x) = 0$ except at $x = 0$, which exhibits the presence of the surface charge at the surface of the metal. This result is consistent with the discontinuity of the potential Φ_t at the interface. Using (4.19), (4.17), (4.10b) and (4.10d)

$$\rho_s = \frac{\epsilon_0\gamma}{\omega}\left(\frac{\epsilon_2-\epsilon_1}{\epsilon_1\epsilon_2}\right), \tag{4.24}$$

hence the total charge per width W of the transmission line is $Q = W\rho_s$. Generally, both the charge Q and the voltage V_0 are complex numbers, thus the ratio Q/V_0 not only determines the capacitance per unit length of the line C, but also the shunt conductance per unit length G

$$\frac{Q}{V_0} = C + \frac{G}{j\omega} = \epsilon_0\kappa_1 W\left(\frac{\epsilon_2}{\epsilon_1+\epsilon_2}\right), \tag{4.25}$$

where C and G are real numbers. This yields that the shunt admittance per unit length of the transmission line is

$$Y = j\omega C + G = j\omega\epsilon_0\kappa_1 W\left(\frac{\epsilon_2}{\epsilon_1+\epsilon_2}\right). \tag{4.26}$$

The inductance per unit length of the transmission line L is more appropriately defined from the magnetic flux linkage ϕ and the current

$$\phi = \mu_0\left(\int_{-\infty}^{0} H_{y2}dx + \int_{0}^{+\infty} H_{y1}dx\right) = \mu_0\left(\frac{1}{\kappa_1}+\frac{1}{\kappa_2}\right). \tag{4.27}$$

Since both ϕ and I_0 are complex values, the ratio ϕ/I_0 determines both the inductance L and the series resistance R per unit length of the transmission line

$$\frac{\phi}{I_0} = L + \frac{R}{j\omega} = \frac{\mu_0\epsilon_1}{\epsilon_0\kappa_1 W}. \tag{4.28}$$

Therefore, the series impedance per unit length of the transmission line is

$$Z = j\omega L + R = \frac{j\omega\mu_0\epsilon_1}{\epsilon_0\kappa_1 W}. \tag{4.29}$$

One can readily verify that $\sqrt{Z/Y}$ gives the characteristic impedance Z_c as defined in (4.23a), and also $ZY = -\gamma^2$. Note that the only deviation from the linear dependance of γ to ω is from the material dispersion, i.e. $\epsilon_2(\omega)$, thereby the plasmonic surface transmission line exhibits very low dispersion.

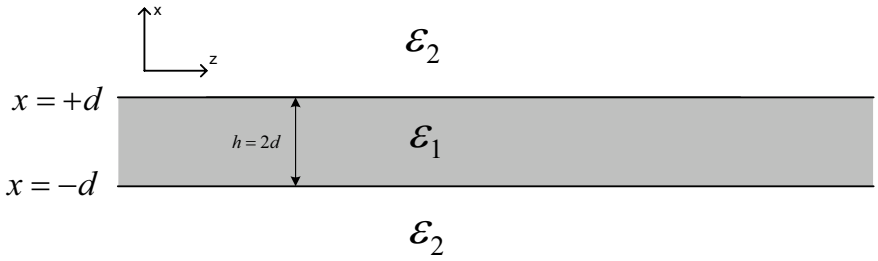

Figure 4.2: Schematic of a PPWG.

4.5 Parallel-Plate Plasmonic Waveguide

The geometry of Figure 4.2 has been extensively studied regarding the propagation of SPPs at optical frequencies, especially when the metal cladding is symmetric. Generally, the structure supports a rich family of modes including both TM and TE modes. The modes of interest regarding the propagation of SPPs are the fundamental even and odd TM modes. Here, the parity refers to the symmetry of the transverse component of the electric field E_x with respect to the center of the core. The lowest order even TM mode has no cut-off for a vanishing core thickness [92]. This point has been used to demonstrate long range propagating modes at optical frequencies [92, 93]. As will be shown later, this particular mode is responsible for low-loss propagation of THz waves in PPWGs. However, for a sufficiently large core thickness, higher order modes begin to appear. At optical frequencies, these modes suffer from high attenuation, therefore, they are not generally considered useful for power transmission [94]. Nevertheless, due to the much larger λ/h ratio at THz frequencies, these modes are more vulnerable to cut-off than their optical counterparts.

The wavefunction $\psi(x)$ associated with this structure follows

$$\psi(x) = \begin{cases} Ae^{-\kappa_2(x-d)}, & \text{for } x > d \\ Be^{\kappa_1(x-d)} + Ce^{-\kappa_1(x+d)}, & \text{for } |x| < d \\ De^{\kappa_2(x+d)}, & \text{for } x < -d \end{cases} \tag{4.30}$$

where

$$\kappa_i = \pm\sqrt{\gamma^2 - \omega^2\mu_o\epsilon_i}, \tag{4.31}$$

and the sign is chosen so that $\Re e\{\kappa_i\} > 0$. Applying the boundary conditions to (4.30), it is found that for the even modes, i.e. $B = C$ and $A = D$,

$$\zeta = -\tanh(\kappa_1 d), \tag{4.32}$$

whereas for the odd solutions, i.e. $B = -C$ and $A = -D$,

$$\zeta = -\coth(\kappa_1 d), \tag{4.33}$$

where $\zeta \equiv (\xi_2\kappa_2)/(\xi_1\kappa_1)$.

4.5.1 TM Modes

The mode conditions (4.32) and (4.33) reduce to (4.5b) for $|\kappa_1 d| \gg 1$, which represents two independent surface waves at each metal-dielectric interface and was examined in the previous section. It can be shown that the lowest order even TM mode[1] has no cut-off for a vanishing core layer thickness [95], i.e. for $|\kappa_1 d| \ll 1$, analogous to the same mode at optical frequencies [93, 96]. Figure 4.3 illustrates the dispersion of the fundamental mode with a varying core thickness in an Au-air-Au PPWG at 1.1THz and 10THz. Clearly, the

[1]Hereafter, this mode is referred to as the fundamental mode of the PPWG.

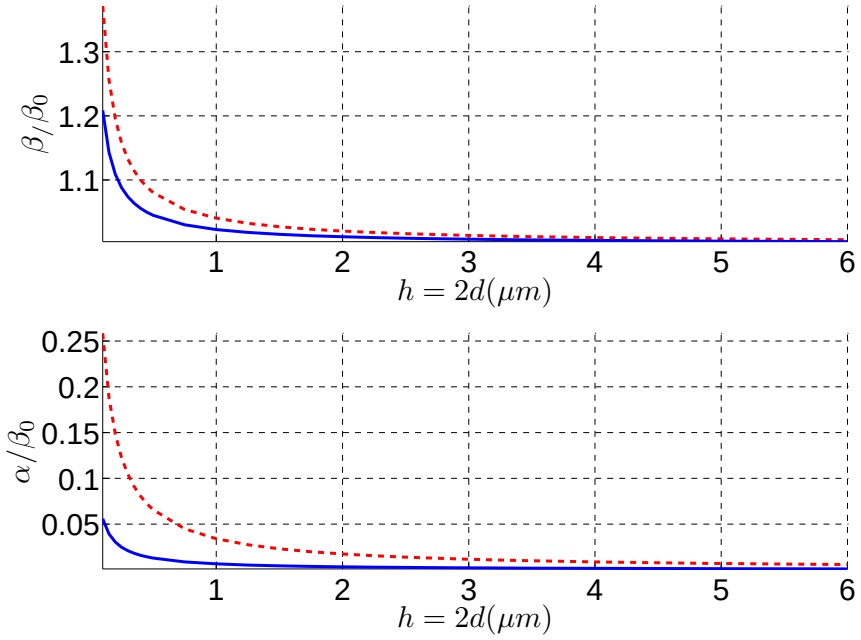

Figure 4.3: The simulated dispersion of the fundamental mode of an Au-air-Au PPWG with a varying core thickness at 10THz (solid curve) and 1.1THz (dashed curve). (a) The normalized phase constant and (b) the normalized attenuation constant.

loss is very small provided that the dielectric thickness is greater than a few micrometers. In contrast, the first odd TM mode does not propagate at small values of d. For example, this mode cuts off below $d = 2.09mm$, in an Au-air-Au PPWG at a frequency of 10THz.

Higher order TM mode solutions with oscillatory fields in the core layer are, in principle, possible for this geometry, however their cut-off thickness are even higher than that of the lowest order odd TM mode. Therefore, for a wide range of separation between the two metals, they are in cut-off and do no play a role in transmission of THz power. This point has also been demonstrated experimentally for DF-PPWGs [57] and AF-PPWGs [55].

Similar results hold if the air is replaced by other dielectrics as well. Figure 4.4 to Figure 4.6 show the dispersion of an Au-Silica-Au PPWG as a function of the core thickness at

three different wavelengths, i.e. $\lambda = 1550nm$, $30\mu m$ and $269\mu m$. For a sufficiently small core thickness, the plasmonic mode is the only guided mode such that the PPWG is a single mode plasmonic waveguide. After the core thickness reaches a fraction of the wavelength other ordinary modes appear as guided waves. As the core thickness increases, the loss of the plasmonic mode approaches to the extinction factor of the dielectric core. Therefore, a low-loss dielectric is required to achieve low-loss THz waveguides. The THz plasmonic mode in PPWG, can be viewed as the result of the resonant coupling of the SPP waves at the two metal surfaces. These modes can be used to design low-loss and low-dispersion THz transmission line [95].

4.5.2 TE Modes

Figure 4.7 and Figure 4.8 show the real and imaginary parts of γ as a function of $h = 2d$ for a Au-air-Au structure at 10THz and 1.1THz, respectively. Obviously, the TE modes are in cut-off for a wide range of the core thicknesses. This result is consistent with the modal properties of TE modes in the same geometry at optical frequencies, where their cut-off thickness is even greater than that of the lowest order odd TM mode [93]. Hence, for a practical dielectric thickness there exists no TE mode which contributes to THz power transmission.

4.5.3 Fundamental Mode

The characteristics of the fundamental mode of a Au-air-Au PPWG are shown in Table 4.3 for different frequencies and dielectric thicknesses. Comparing the propagation constant of the fundamental mode with that of the surface wave in MD-SW and also the field solution (4.30) in the bounded region, it is obviously seen that the fundamental mode is associated

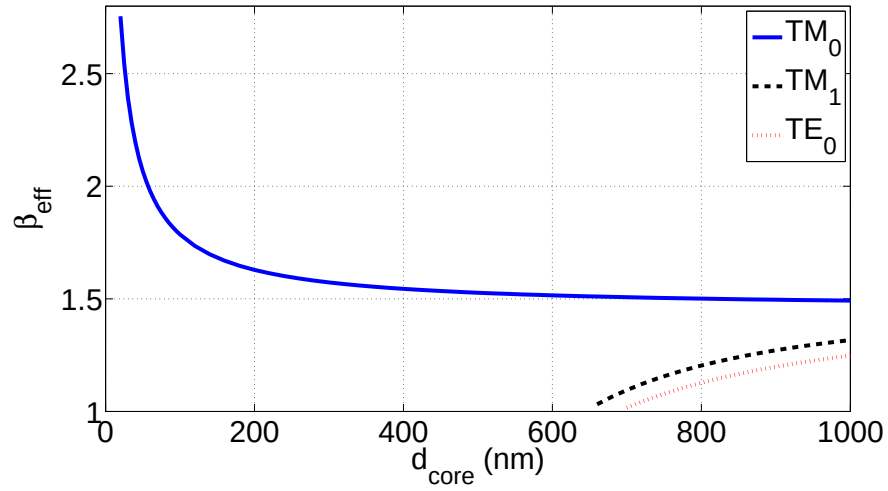

(a)

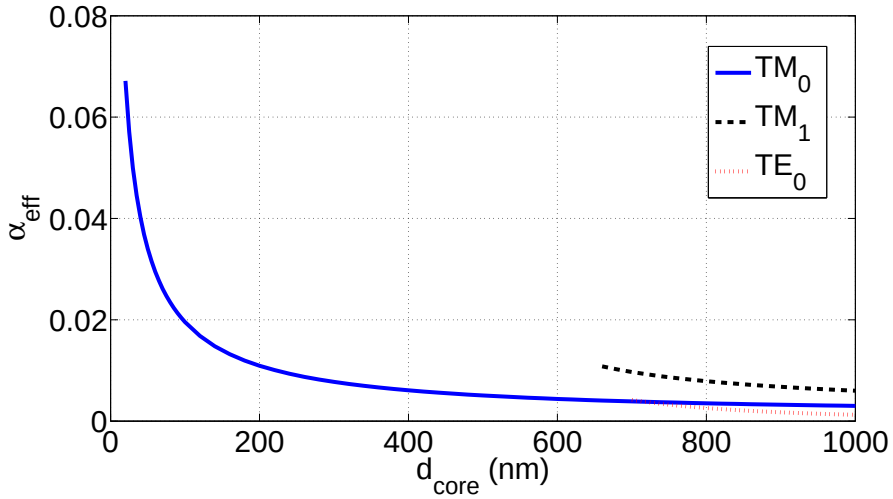

(b)

Figure 4.4: Simulated dispersion of the guided modes of Au-Silica-Au parallel plate waveguide as a function of the core thickness. **(a)** effective refractive index of the modes for Au-Silica-Au PPWG at $\lambda = 1550nm$;**(b)** normalized attenuation constant of the modes for Au-Silica-Au PPWG at $\lambda = 1550nm$.

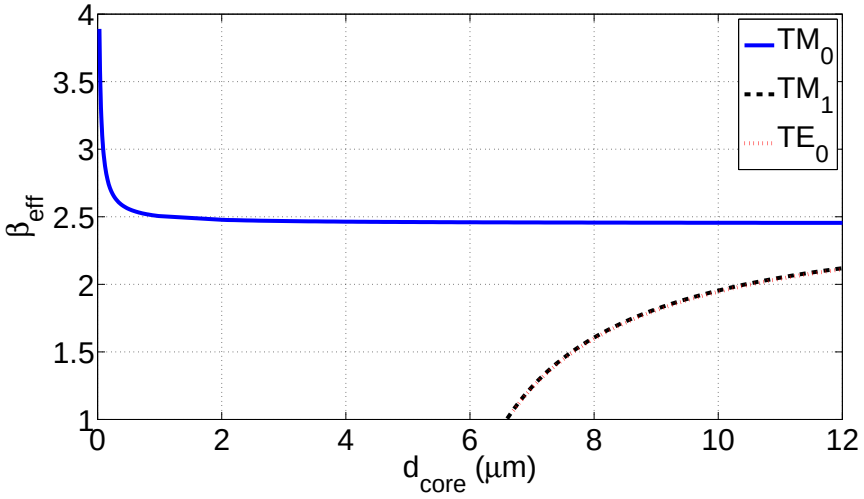

(a)

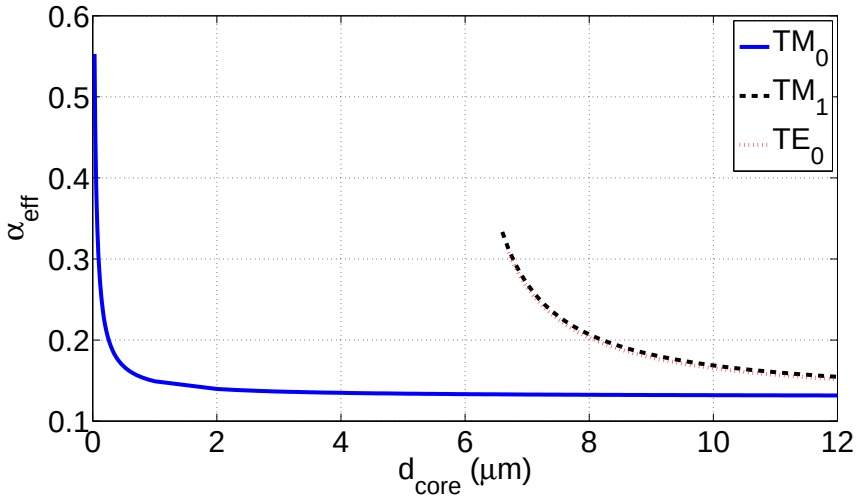

(b)

Figure 4.5: Simulated dispersion of the guided modes of Au-Silica-Au parallel plate waveguide as a function of the core thickness. **(a)** effective refractive index of the modes for Au-Silica-Au PPWG at $\lambda = 30\mu m$;**(b)** normalized attenuation constant of the modes for Au-Silica-Au PPWG at $\lambda = 30\mu m$.

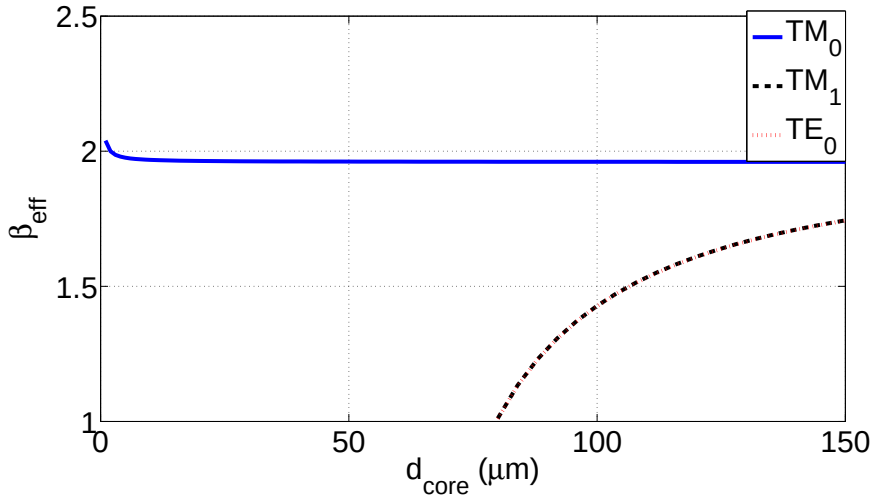

(a)

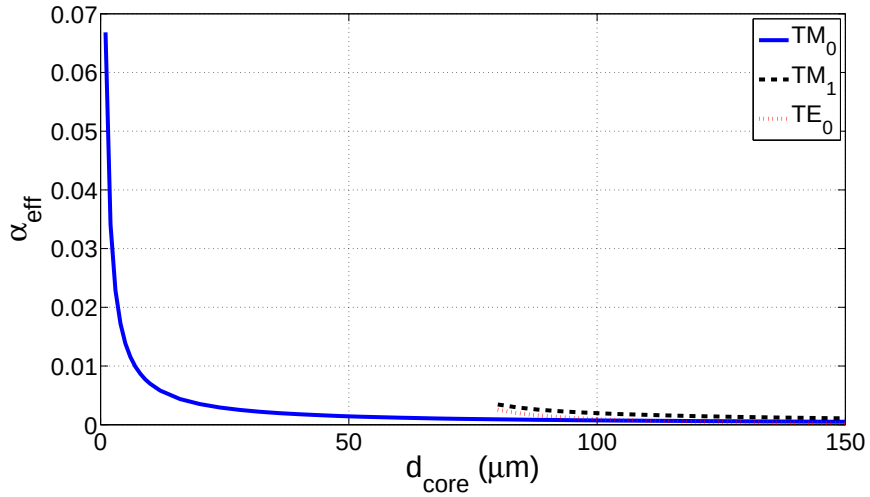

(b)

Figure 4.6: Simulated dispersion of the guided modes of Au-Silica-Au parallel plate waveguide as a function of the core thickness. **(a)** effective refractive index of the modes for Au-Silica-Au PPWG at $\lambda = 269\mu m$;**(b)** normalized attenuation constant of the modes for Au-Silica-Au PPWG at $\lambda = 269\mu m$.

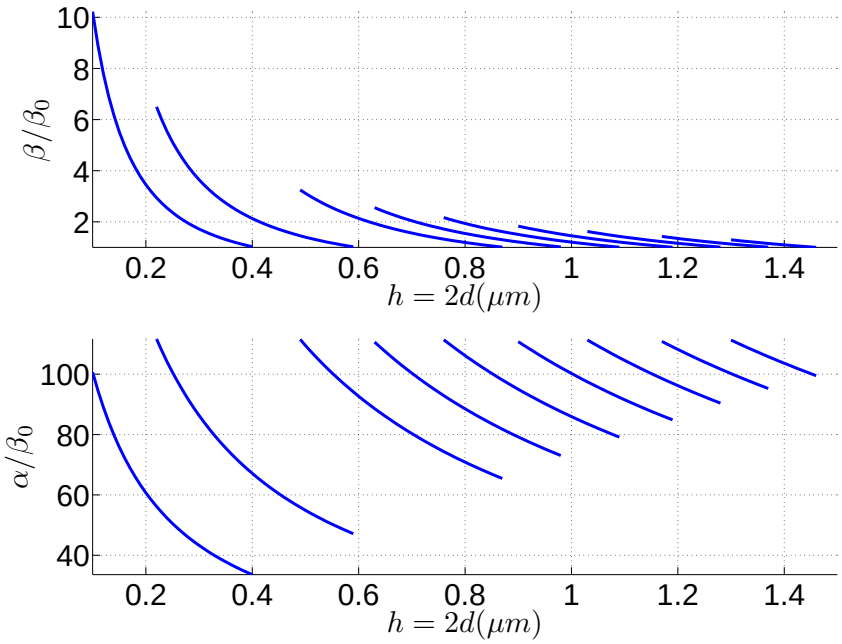

Figure 4.7: The real and imaginary parts of the simulated propagation constant for the TE modes associated with an Au-air-Au PPWG as a function of the separation between the metal plates, at a frequency of 10THz.

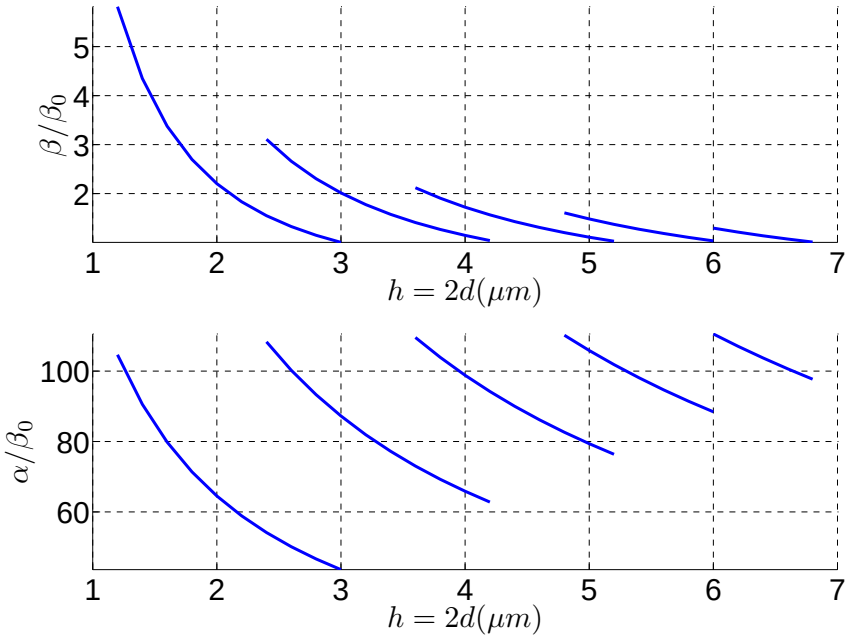

Figure 4.8: The real and imaginary parts of the simulated propagation constant for the TE modes associated with an Au-air-Au PPWG as a function of the separation between the metal plates, at a frequency of 1.1THz.

Table 4.3: Simulated characteristics of the fundamental mode of an Au-air-Au PPWG at different dielectric thicknesses and wavelengths.

$\lambda(\mu m)$	$h(\mu m)$	β/β_0	α/β_0	$\lvert E_z\rvert/\lvert E_x\rvert$
30	1	1.0226	6.60×10^{-3}	≤ 0.005
30	20	1.0011	3.39×10^{-4}	≤ 0.005
30	100	1.0002	6.97×10^{-5}	≤ 0.005
30	1000	1.0000	9.50×10^{-6}	≤ 0.005
269	1	1.0405	3.41×10^{-2}	≤ 0.001
269	20	1.0020	1.77×10^{-3}	≤ 0.001
269	100	1.0004	3.55×10^{-4}	≤ 0.001
269	1000	1.0000	3.57×10^{-5}	≤ 0.001

with the coupled surface waves at the two metal-dielectric interfaces attributed to the resonant excitation of SPPs at the two boundaries.

At the large dielectric thickness limit, the waveguide approaches to two independent surface waveguides. Therefore, from previous sections $|\epsilon_2| \gg |\epsilon_1|$ guarantees that the fundamental guided mode is a quasi-TEM wave at large separation between metals. At the thin dielectric approximation, $|\kappa_1 d| \ll 1$, it is readily found that

$$\gamma \simeq \omega\sqrt{\mu_0\epsilon_1} + \frac{1}{2d}\sqrt{\frac{-\epsilon_1}{\epsilon_2}}, \tag{4.34a}$$

$$\kappa_1 \simeq \sqrt{\frac{\omega\sqrt{\mu_0\epsilon_1}}{d}\sqrt{\frac{-\epsilon_1}{\epsilon_2}}}, \tag{4.34b}$$

$$\kappa_2 \simeq \omega\sqrt{\mu_0\epsilon_2}. \tag{4.34c}$$

Since $|E_x|/|E_z| = |\gamma|/|\kappa_1|$, the condition of having a quasi-TEM wave is

$$\left(\omega d\sqrt{\mu_0|\epsilon_2|}\right)^{1/2} \gg 1, \tag{4.35}$$

which is normally satisfied for d greater than a few micrometers. The approximations

(4.34) are valid as long as $|\kappa_1 d| \ll 1$, which corresponds to

$$\left(\omega d\sqrt{\mu_0|\epsilon_1|}\sqrt{\frac{|\epsilon_1|}{|\epsilon_2|}}\right)^{1/2} \ll 1, \tag{4.36}$$

For the Au-air-Au PPWG, (4.36) holds up to $d \simeq 500\mu m$ at 1.1THz and $d \simeq 60\mu m$ at 10THz. If the condition (4.36) holds, the field in the dielectric is almost constant. This corresponds to strong coupling between the surface plasmons of the two interfaces. Figure 4.9 shows $|\psi(x)|^2$ for different situations in the Au-air-Au PPWG.

4.6 PPWG Transmission Line

The field components for the fundamental mode of the PPWG of Figure 4.2 are explicitly shown below

$$\mathbf{H}_1 = (0,1,0)(1+\Gamma)e^{-\kappa_2(x-d)}, \tag{4.37a}$$

$$\mathbf{E}_1 = (\frac{\gamma}{\omega\epsilon_2}, 0, \frac{j\kappa_2}{\omega\epsilon_2})(1+\Gamma)e^{-\kappa_2(x-d)}, \tag{4.37b}$$

$$\mathbf{H}_2 = (0,1,0)\left[e^{\kappa_1(x-d)} + e^{-\kappa_1(x+d)}\right], \tag{4.37c}$$

$$\mathbf{E}_2 = (\frac{\gamma}{\omega\epsilon_1}, 0, \frac{-j\kappa_1}{\omega\epsilon_1})\left[e^{\kappa_1(x-d)} \pm e^{-\kappa_1(x+d)}\right], \tag{4.37d}$$

$$\mathbf{H}_3 = (0,1,0)(1+\Gamma)e^{\kappa_2(x+d)}, \tag{4.37e}$$

$$\mathbf{E}_3 = (\frac{\gamma}{\omega\epsilon_2}, 0, \frac{-j\kappa_2}{\omega\epsilon_2})(1+\Gamma)e^{\kappa_2(x+d)}, \tag{4.37f}$$

where $\Gamma \equiv e^{-2\kappa_1 d}$, and all the field components share in a $e^{j(\omega t-\gamma z)}$ factor. Also, the plus sign in (4.37d) belongs to E_{x2} and the minus sign is for E_{z2}.

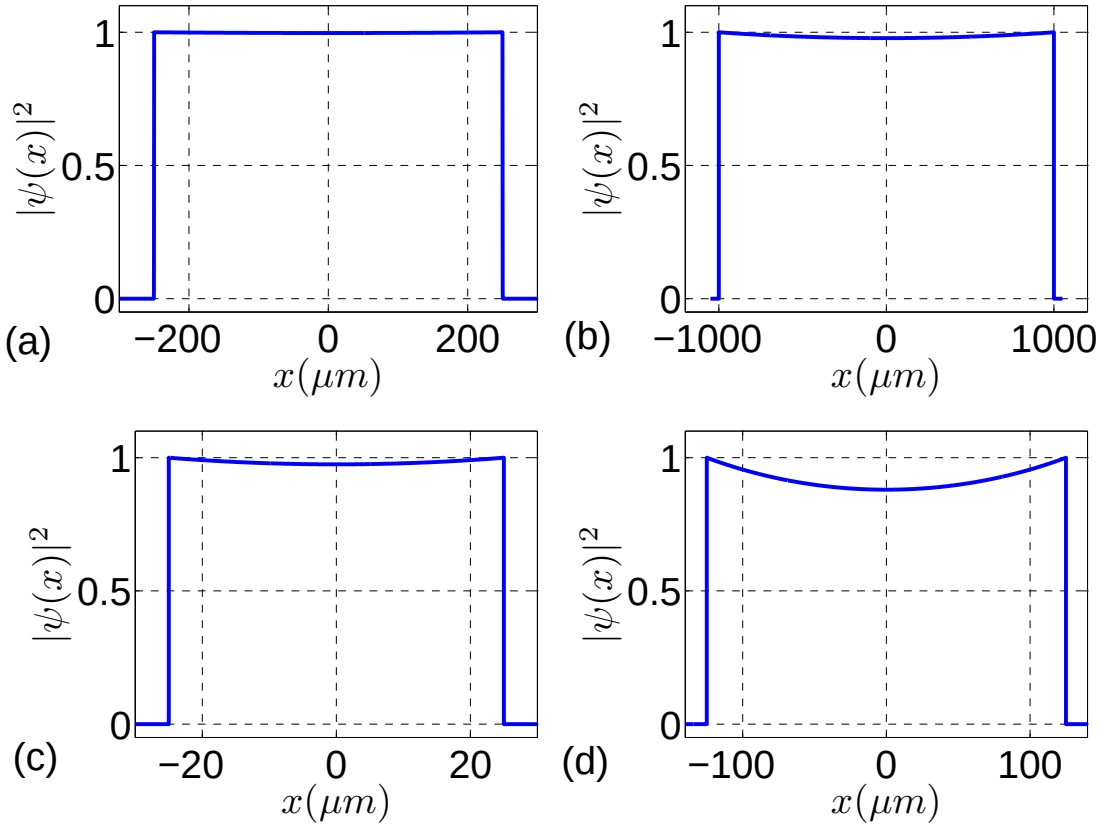

Figure 4.9: Simulated $|\psi(x)|^2$ in an Au-air-Au PPWG for (a) h=500 μm and f =1.1 THz, (b) h=2000 μm and f =1.1 THz, (c) h=50 μm and f =10 THz, and (d) h=250 μm and f =10 THz.

Voltage

The potential $\Phi_t(x)$ is the solution of (4.12) subjected to the conditions $\Phi_t(\pm\infty) = 0$

$$\Phi_t(x) = \begin{cases} \frac{\gamma(1+\Gamma)}{\omega\epsilon_2\kappa_2} e^{-\kappa_2(x-d)}, & \text{for } x > d \\ \frac{-\gamma}{\omega\epsilon_1\kappa_1}\left[e^{\kappa_1(x-d)} - e^{-\kappa_1(x+d)}\right], & \text{for} |x| < d \\ \frac{-\gamma(1+\Gamma)}{\omega\epsilon_2\kappa_2} e^{\kappa_2(x+d)}, & \text{for } x < -d \end{cases} . \tag{4.38}$$

The discontinuity of the potential $\Phi_t(x)$ at the surface of the metallic plates shows the presence of surface charge. The voltage of the bottom and top plates are defined as $V_B \equiv \Phi_t(-d^+) - \Phi_t(-d^-)$ and $V_T \equiv \Phi_t(d^-) - \Phi_t(d^+)$, respectively. Therefore, the voltage at each point along the transmission line is

$$V(z) = V_0 e^{j(\omega t - \gamma z)}, \tag{4.39}$$

where

$$V_0 \equiv V_B - V_T = \frac{2\gamma}{\omega}\left[\frac{1-\Gamma}{\epsilon_1\kappa_1} + \frac{1+\Gamma}{\epsilon_2\kappa_2}\right]. \tag{4.40}$$

If the condition of strong coupling (4.36) holds, or equivalently $|\kappa_1 d| \ll 1$, then (4.40) reduces to

$$V_0 = \frac{2\gamma h}{\omega\epsilon_1}, \tag{4.41}$$

where $h = 2d$.

Current

Applying (4.18) to (4.37), gives

$$\mathbf{J_1} = (\epsilon_2 - \epsilon_0)(\frac{j\gamma}{\epsilon_2}, 0, \frac{-\kappa_2}{\epsilon_2})(1+\Gamma)e^{-\kappa_2(x-d)}, \tag{4.42a}$$

$$\mathbf{J_2} = (\epsilon_1 - \epsilon_0)(\frac{j\gamma}{\epsilon_1}, 0, \frac{\kappa_1}{\epsilon_1})\left[e^{\kappa_1(x-d)} \pm e^{-\kappa_1(x+d)}\right], \tag{4.42b}$$

$$\mathbf{J_3} = (\epsilon_2 - \epsilon_0)(\frac{j\gamma}{\epsilon_2}, 0, \frac{\kappa_2}{\epsilon_2})(1+\Gamma)e^{\kappa_2(x+d)}, \tag{4.42c}$$

where the plus sign in (4.42b) belongs to J_{x2} and the minus sign is for J_{z2}, and all the current densities share in $e^{j(\omega t - \gamma z)}$ factor.

The longitudinal current for width W of the PPWG is

$$I(z) = W\left(\int_{-\infty}^{-d} J_{z3}(x)dx + \int_{-d}^{0} J_{z2}(x)dx\right) = I_0 e^{j(\omega t - \gamma z)}, \tag{4.43}$$

where

$$I_0 \simeq \epsilon_0\left(\frac{\epsilon_2 - \epsilon_1}{\epsilon_1\epsilon_2}\right)(1+\Gamma)W. \tag{4.44}$$

For the case of strong coupling $|\kappa_1 d| \ll 1$, the current is

$$I_0 = \frac{2\epsilon_0}{\epsilon_1}W. \tag{4.45}$$

4.6.1 Line Parameters

Characteristic Impedance

Using (4.40) and (4.44), the characteristic impedance of the transmission line is

$$Z_c \equiv \frac{V_0}{I_0} = \frac{2\mu_0\epsilon_1\omega\gamma}{\epsilon_0\kappa_1^2\kappa_2 W}. \tag{4.46}$$

In case of strong coupling, where the field in the dielectric is almost uniform, (4.46) reduces to that of a conventional PPWG

$$Z_c = \frac{\eta_0 h}{W}\sqrt{\frac{\epsilon_1}{\epsilon_0}}, \tag{4.47}$$

where $\eta_0 = \sqrt{\mu_0/\epsilon_0}$ is the intrinsic impedance of free space. For example, the characteristic impedance of the Au-air-Au parallel-plate plasmonic transmission line is 50Ω for $h = 400\mu m$ and $W = 3mm$ at 1.1THz; and $h = 60\mu m$ and $W = 450\mu m$ at 10THz.

Shunt Admittance and Series Impedance

Using (4.19), it is readily found that $\rho(x) = 0$ except at $x = \pm d$, which exhibits the presence of the surface charge at the surface of the metallic plates.

$$\rho_s = \frac{\epsilon_0 \gamma}{\omega}\left(\frac{\epsilon_2 - \epsilon_1}{\epsilon_1 \epsilon_2}\right)(1 + \Gamma), \tag{4.48}$$

hence, the total charge per width W of the transmission line is $Q = W\rho_s$. Therefore, the shunt admittance per unit length of the transmission line is

$$Y \equiv \frac{j\omega Q}{V_0} = j\omega C + G = \frac{j\epsilon_0 \kappa_1^2 \kappa_2 W}{2\omega\mu_0\epsilon_1}. \tag{4.49}$$

For strong coupling, this expression simplifies to the capacitance of a conventional PPWG

$$C = \frac{\epsilon_0 W}{h}. \tag{4.50}$$

The impedance per unit length of the transmission line is defined by means of the

magnetic flux linkage ϕ and the current

$$\phi = \mu_0 \int_{-\infty}^{\infty} H_y dx = 2\mu_0 \left(\frac{1-\Gamma}{\kappa_1} + \frac{1+\Gamma}{\kappa_2} \right), \tag{4.51}$$

and thus,

$$Z \equiv \frac{j\omega\phi}{I_0} = \frac{j2\mu_0\epsilon_1\omega\gamma^2}{\epsilon_0\kappa_1^2\kappa_2 W}. \tag{4.52}$$

For strong coupling, the inductance of a conventional PPWG is recovered

$$L = \frac{\epsilon_1\eta_0^2 h}{W}. \tag{4.53}$$

One can readily verify that $\sqrt{Z/Y}$ gives the characteristic impedance Z_c as defined in (4.46), and also $ZY = -\gamma^2$.

4.7 Summary

This chapter studied the surface waveguide and the parallel-plate waveguide for transmission of THz waves. Full-wave field analysis was employed to distinguish the conditions of quasi-TEM and low-loss propagation of THz signals. Transmission line models were proposed based on the surface waves corresponding to the waveguides' plasmonic modes, which are consistent with the experimentally demonstrated low-loss, quasi-TEM and low-dispersion characteristics of these waveguides. The transmission line models enables the application of circuit-like techniques for the analysis and design of the elements of THz monolithic integrated circuits, such as filters, directional couplers, power dividers and interconnects as well as traveling-wave devices such as THz photomixers and detectors.

The fundamental even TM mode was shown to be responsible for low-loss, quasi-TEM and low-dispersion propagation of THz signals in PPWGs. Moreover, it was discussed that

this mode doesn't have a cut-off for vanishing core layer thickness. Thus, this mode can provide sub-wavelength confinement of THz fields well below the diffraction limit. This mode corresponds to resonant excitation of surface plasmons at the two metal-dielectric boundaries; therefore, the PPWG can be viewed as two coupled surface waveguides, which support two coupled surface waves. Employing this surface plasmonic mode, a consistent transmission line model for PPWG was obtained that gives the observed features of THz propagation, which reduces to the conventional transmission line model at the limiting case of the strong coupling. The existence of TE modes as well as higher order TM modes with oscillatory field profile in the core layer were examined. While these modes can in principle exist for sufficiently large thickness of the core layer, they are all in cut-off under usual operating conditions in terms of the materials used for the core and metal cladding as well as a practical thickness of the core layer.

Chapter 5

Superconducting Optical Waveguides

5.1 Introduction

The integration of superconducting devices with photonic guided-wave structures is an emerging strategy for ultra-fast and ultra-sensitive optoelectronics [97]. Several novel devices, such as traveling-wave photodetectors and traveling-wave photomixers [86, 98], have been introduced based on this strategy and quite a few attempts have been recently made for integrating optical waveguides with superconducting junctions [99, 100]. Before these works, application of optical guided-wave structures in a superconducting device was rather rare, and even fewer concern a real optoelectronic device. Nonetheless, two specific works are really worth mentioning. The first one is the elegant and still admirable work of Gilabert and coworkers in the late 70s [101], in which a photodetector was proposed based on inducing a superconducting weak-link by optical guided waves. The second is the work of Yoshida and coworkers in the 90s [102], which consists of a traveling-wave $LiNbO_3$ modulator integrated with a superconducting transmission line. While the former takes advantage of a superconductive photoresponse, in the latter the real optoelectronic mechanism is that

of the $LiNbO_3$ and the superconducting part improves the device performance in terms of loss and dispersion.

The incorporation of photonic guided-wave structures, especially optical waveguides, into superconducting optoelectronic devices offers many different advantages. The most prominent of all is the enhancement of optical coupling to the active regions; inasmuch as unguided coupling of optical power to an optoelectronic device is usually very inefficient. This argument is true for almost any optoelectronic device, including superconducting and semiconductor devices. Thus, the overall system efficiency of waveguide devices are normally much higher than their illuminated analogues. This factor is much more critical for ultra-sensitive devices such as photon detectors. Given the fact that single photon detectors and photon counting devices comprise an important part of superconducting optoelectronics, their integration with optical waveguides is a promising prospect. For example, one would expect that integrating an optical waveguide with SNSPDs results in a substantial improvement of the overall device quantum efficiency.

Waveguide optoelectronic devices also have the advantage that their response to different states of the optical input can be engineered. For instance, the modal characteristic of the waveguide can be designed in order to achieve polarization sensitivity or to filter some specific modes. For devices operating at visible, near- and mid-infrared wavelengths, optical power can be coupled from the free space or a fiber to the waveguide and thereby to the active region. For devices at far-infrared and THz regime, an antenna can feed the waveguide. In the case that the entire optical power is not absorbed by a single active region, a series of lumped element devices could be fed by a single waveguide. This technique, in turn, raises such new possibilities as phased array and periodic devices. Furthermore, incorporation of an optical waveguide with superconducting devices is very promising for monolithic superconducting circuits, where several components and sub-systems are present on the

same chip. The SFQ digital processors and quantum information processing chips are two good examples of this.

Moreover, traveling-wave devices are the other important class of guided-wave optoelectronic devices, which is the subject of the next chapter. The main difference between the traveling-wave and waveguide devices, is that the optoelectronic active region of the former is not a lumped element anymore. In fact, in traveling-wave devices, the optoelectronic functions are performed in a distributed manner along the effective length of the active region.

This chapter discusses the analysis, simulation, and design of multilayer slab optical waveguides, which contain dielectric, metal, and superconducting layers. A systematic approach, based on the transfer matrix method, is presented to model a multilayer waveguide with any arbitrary number of layers and materials; and obtaining the dispersion equations for the TM and TE modes. A robust and efficient numerical technique is developed to find the complex roots of the dispersion equations, which are in fact the propagation constants of the guided-modes. In addition, two major classes of waveguide design are introduced for application in superconducting waveguide optoelectronic devices, including traveling-wave structures.

5.2 Analysis of a General Multilayer Slab Waveguide

According to chapters 2 and 3, the width of active region for a typical superconducting device is in practice many times greater than an optical wavelength. Therefore, a practical superconducting optical waveguide may be conveniently approximated as a one-dimensional slab waveguide. This section aims at finding the solutions of the Maxwell equations for the general structure of Figure 5.1, which consists of linear, isotropic, and

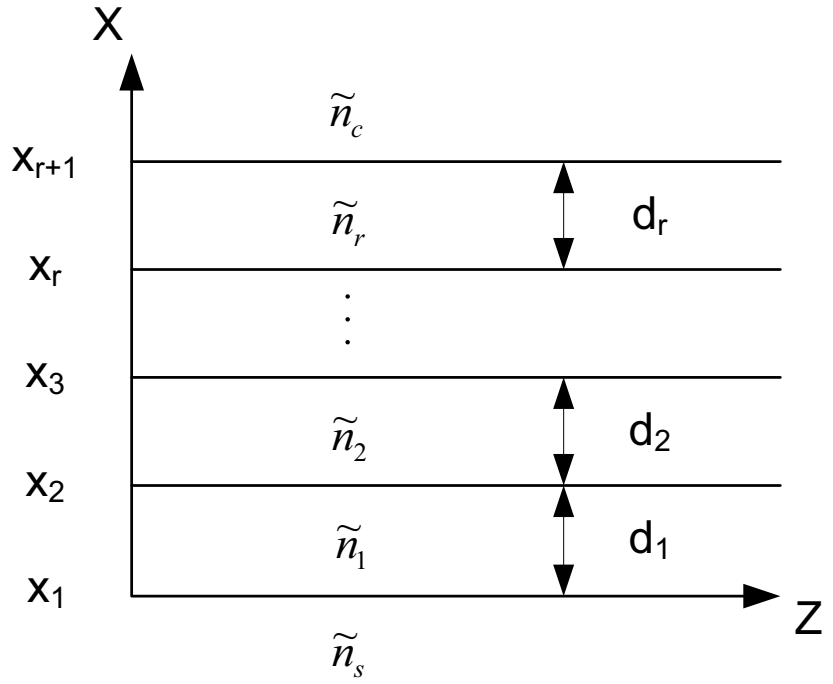

Figure 5.1: Cross section of a general planar multilayer structure.

homogeneous materials. For the sake of simplicity, it is further assumed that the materials are all non-magnetic. Therefore, each layer is characterized by its thickness d_i and complex refractive index $\tilde{n} = n_i - jk_i$, where n_i and k_i being the refractive index and the extinction coefficient respectively.

Because $\partial/\partial y = 0$ along the structure, the field components (E_y, H_x, H_z) and (H_y, E_x, E_z) decouple; and constitute the TE and TM modes respectively. In general, the nonzero field components of an eigenmode is of the form (ψ_y, ψ_x, ψ_z). Assuming a harmonic time variation

$$\psi_y(x, z; t) = \psi(x)e^{j(\omega t - \gamma z)}, \tag{5.1}$$

$$\psi_x(x,z;t) = \frac{-\gamma\xi}{\omega\mu_0}\psi(x)e^{j(\omega t-\gamma z)}, \tag{5.2}$$

and

$$\psi_z(x,z;t) = \frac{j\xi}{\omega\mu_0}\frac{d\psi(x)}{dx}e^{j(\omega t-\gamma z)}, \tag{5.3}$$

where $\xi = 1$ for TE modes and $\xi = -\mu_0/(\epsilon_0\tilde{n_i}^2)$ in each layer for TM modes. The wavefunction $\psi(x)$ satisfies the one-dimensional wave equation

$$\left[\frac{d^2}{dx^2} + \left(\beta_0^2\tilde{n}^2(x) - \gamma^2\right)\right]\psi(x) = 0, \tag{5.4}$$

with $\beta_0 = \omega\sqrt{\mu_0\epsilon_0}$. Since $\tilde{n}(x)$ is generally a complex function, the propagation constant γ is also complex and can be written as $\gamma = \beta - j\alpha$, where β is the phase constant and α is the attenuation constant. For convenience, the normalized phase and attenuation constants may be respectively defined as $\beta_{eff} = \beta/\beta_0$ and $\alpha_{eff} = \alpha/\beta_0$. The solution to the wave equation (5.4) in the i'th layer for $i = 1, 2, ..., r$ is

$$\psi_i(x) = A_i e^{-j\kappa_i(x-x_i)} + B_i e^{+j\kappa_i(x-x_i)}, \tag{5.5}$$

where

$$\kappa_i = \pm\sqrt{\beta_0^2\tilde{n}_i^2 - \gamma^2}. \tag{5.6}$$

The boundary condition at the interface of two layers is the continuity of the tangential fields, ψ_y and ψ_z. To apply the boundary conditions to all the interfaces, it is convenient to define the transfer matrix of each layer as follows. The transfer matrix of the i'th layer M_i, relates the transverse tangential field ψ_{yi} and its derivative at the bottom boundary of a layer $x = x_i$, to the corresponding quantities at the top boundary of the same layer,

$x = x_{i+1}$.

$$\begin{bmatrix} \psi_{yi}(x_i) \\ \zeta_i \dfrac{d\psi_{yi}}{dx}(x_i) \end{bmatrix} = M_i \begin{bmatrix} \psi_{yi}(x_{i+1}) \\ \zeta_i \dfrac{d\psi_{yi}}{dx}(x_{i+1}) \end{bmatrix}, \tag{5.7}$$

where $\zeta_i = 1$ for TE modes and $\zeta_i = 1/\tilde{n}_i^2$ for TM modes. Using equations (5.1), (5.3) and (5.5) it is straightforward to find M_i,

$$M_i = \begin{bmatrix} \cos \kappa_i d_i & -\dfrac{1}{\zeta_i \kappa_i} \sin \kappa_i d_i \\ \zeta_i \kappa_i \sin \kappa_i d_i & \cos \kappa_i d_i \end{bmatrix}. \tag{5.8}$$

By means of the transfer matrices and using the continuity of ψ_{yi} and $\zeta_i(d\psi_y/dx)$ at the interface of two layers, one can readily construct a relation between these two quantities at the substrate interface to the corresponding values at the cover interface

$$\begin{aligned} \begin{bmatrix} \psi_{ys}(0) \\ \zeta_s \dfrac{d\psi_{ys}}{dx}(0) \end{bmatrix} &= \left(\prod_{i=1}^{r} M_i \right) \begin{bmatrix} \psi_{yc}(x_{r+1}) \\ \zeta_c \dfrac{d\psi_{yc}}{dx}(x_{r+1}) \end{bmatrix} \\ &\equiv \begin{bmatrix} m_{11} & m_{12} \\ m_{21} & m_{22} \end{bmatrix} \begin{bmatrix} \psi_{yc}(x_{r+1}) \\ \zeta_c \dfrac{d\psi_{yc}}{dx}(x_{r+1}) \end{bmatrix}. \end{aligned} \tag{5.9}$$

Since guided modes of the waveguide are being considered, the field in the substrate and cover must vanish at infinity

$$\psi_{ys}(x) = A_s e^{\gamma_s x} \qquad x \leq 0, \tag{5.10}$$

and

$$\psi_{yc}(x) = B_c e^{-\gamma_c (x - x_{r+1})} \qquad x_{r+1} \leq x, \tag{5.11}$$

where

$$\gamma_s = \pm\sqrt{\gamma^2 - \beta_0^2 \tilde{n}_s^2}, \tag{5.12}$$

and

$$\gamma_c = \pm\sqrt{\gamma^2 - \beta_0^2 \tilde{n}_c^2}, \tag{5.13}$$

and the signs must be chosen in a way to have $\Re e(\gamma_s) > 0$ and $\Re e(\gamma_c) > 0$.

The two equations (5.10) and (5.11) combined with (5.7) and yield the dispersion equation for the guided modes, whose complex roots are the complex propagation constants of the propagating modes

$$f(\gamma) = \zeta_s \gamma_s m_{11} + \zeta_c \gamma_c m_{22} - m_{21} - \zeta_s \zeta_c \gamma_s \gamma_c m_{12} = 0. \tag{5.14}$$

5.3 Numerical Solution to the Dispersion Equation

There are traditionally numerous numerical methods available to solve transcendental equations akin to the dispersion equation found in the last section. One major shortcoming of these methods, such as the Newton's method [103] or downhill method [104], is that they all need a priori knowledge about the number of roots as well as an initial guess for them. In most cases, there is no such initial knowledge available. Furthermore, most of these methods are limited by the number of layers or the materials that constitute the waveguide. In superconducting optical waveguides, the extinction factor k of the superconducting layer may be of the same order as n. Therefore, such structures cannot be solved by perturbative methods, which are commonly used to account for lossy dielectrics. This section introduces an efficient, robust, and general numerical method, based on the Cauchy integral theorem and the argument principle method (APM), which is capable of handling any number of layers with any arbitrary complex index of refraction and solves

both the guided and leaky modes of the waveguide.

The general method was proposed in the 60s to solve for the roots of any arbitrary analytical function in the complex plane [105]. The use of this method to solve the planar multilayer waveguides was suggested for the first time in the early 90s [106] and independently shortly afterward in [107] with a slightly different formulation and much more convenience in the numerical implementation. Some elegant modifications were later suggested to eliminate the most computation intensive task of the method by means of analytical calculation of the derivative of the dispersion equation, as well as the extension for solving the anisotropic waveguides [108].

The basic idea behind this method is to find a polynomial whose roots are the same as those of the dispersion equation. Instead of solving for the roots of a transcendental equation the polynomial is solved, for which many efficient and convenient methods exist. Thus, to find the roots (z_i) of the dispersion equation (5.14), it is required to construct the polynomial

$$p\left(z\right)=\prod_{i=1}^{S_0}\left(z-z_i\right)=\sum_{k=0}^{S_0}C_k z^k. \tag{5.15}$$

The order of the polynomial S_0, which corresponds to the number of the roots of $f(z)$, and the coefficients C_k are found by means of the Cauchy integral theorem. The theorem states that for a function $f(z)$ which is analytical within and on the contour C,

$$S_m \equiv \frac{1}{j2\pi}\oint_c z^m \frac{f'\left(z\right)}{f\left(z\right)}dz=\sum_i z_i^m. \tag{5.16}$$

It is readily seen that by putting $m=0$ and calculating the above integral the number of the zeros S_0 and, thereby the order of polynomial are obtained at once. Because the answer is known to be an integer, it is not even necessary to evaluate the integral with a high precision at this step. Then, for $m=1,2,...,S_0$ the integral should be evaluated

accurately to find S_m, from which the coefficients of the polynomial can be calculated by the Newton recursive formula. Assuming that the coefficient of the highest order term is unity [109],

$$C_k = \frac{1}{(k - S_0)} \sum_{j=1}^{S_0 - k} S_j C_{k+j} \quad (k = S_0 - 1, ..., 0)\,. \tag{5.17}$$

Computing the integral (5.16) involves three main tasks. First, evaluating the value of the function $f(z)$ and its derivative at any arbitrary point. Second, choosing the proper contour which contains all the roots of the dispersion equation corresponding to the guided modes of the waveguide. Third, implementing an efficient numerical method to evaluate the integral.

Evaluation of the dispersion equation at a point $f(\gamma)$ at $\gamma = z$ may be done by multiplication of the two-by-two matrices M_i and using (5.14). In the following, the other two main requirements are addressed.

5.3.1 Evaluation of the Derivative of the Dispersion Equation

In general, the derivative of any analytical function may be evaluated through proper numerical methods. Here, an semi-analytical approach will be presented [108], which considerably reduces the computational cost of the Cauchy integral method. Let's define u as $\gamma = k_0 u$. It is straightforward to show that the derivative of the transfer matrices dM_i/du is

$$\begin{bmatrix} \frac{k_0^2 d_i}{\kappa_i} \sin \kappa_i d_i & \frac{k_0^2 d_i}{\zeta_i \kappa_i^2} \cos \kappa_i d_i - \frac{k_0^2}{\zeta_i \kappa_i^3} \sin \kappa_i d_i \\ \frac{-\zeta_i k_0^2}{\kappa_i} \sin \kappa_i d_i - \zeta_i k_0^2 d_i \cos \kappa_i d_i & \frac{k_0^2 d_i}{\kappa_i} \sin \kappa_i d_i \end{bmatrix}.$$

The derivative of the transfer matrix of the multilayer structure subsequently follows

$$\frac{dM}{du} \equiv \begin{bmatrix} \frac{dm_{11}}{du} & \frac{dm_{12}}{du} \\ \frac{dm_{21}}{du} & \frac{dm_{22}}{du} \end{bmatrix} = \sum_{j=1}^{r} \left[\frac{dM_j}{du} . \prod_{i=1, i\neq j}^{r} M_i \right]. \tag{5.18}$$

Thus, the derivative of the dispersion equation is obtained as

$$\begin{aligned} \frac{df(u)}{du} &= \frac{\zeta_s k_0^2 u}{\gamma_s} m_{11} + \frac{\zeta_c k_0^2 u}{\gamma_c} m_{22} + \zeta_s \gamma_s \frac{dm_{11}}{du} \\ &+ \zeta_c \gamma_c \frac{dm_{22}}{du} - \frac{dm_{21}}{du} - \frac{\zeta_s \zeta_c \gamma_c k_0^2 u}{\gamma_s} m_{12} \\ &- \frac{\zeta_s \zeta_c \gamma_s k_0^2 u}{\gamma_c} m_{12} - \zeta_s \zeta_c \gamma_s \gamma_c \frac{dm_{12}}{du}. \end{aligned} \tag{5.19}$$

In order to evaluate the derivative of the transfer matrix efficiently, the following algorithm is used. For the first layer, M_1 and $\frac{dM_1}{du}$ are computed. At the second layer, M_2 and $\frac{dM_2}{du}$ are calculated. At this point, $M^{(2)} = M_1 M_2$ and $\frac{dM}{du}^{(2)} = M_1 \frac{dM_2}{du} + \frac{dM_1}{du} M_2$. This procedure is repeated at each step with $M^{(i+1)} = M^{(i)} M_{i+1}$ and $\frac{dM}{du}^{(i+1)} = M^{(i)} \frac{dM_{i+1}}{du} + \frac{dM}{du}^{(i)} M_{i+1}$.

5.3.2 Determination of the Proper Contour for Integration

For a guided mode in a multilayer structure, with complex propagation constant $\gamma = k_0(\tilde{\beta} - j\tilde{\alpha})$, $\tilde{\beta}$ obeys the inequality [110]

$$\max(n_s, n_c) < \tilde{\beta} < \max(n_i). \tag{5.20}$$

Furthermore, there is a limitation on the attenuation constant of a guided mode $\tilde{\alpha}$. A

guided mode cannot be more dissipative than a plane wave propagating in a homogenous medium solely consisted of the most dissipative material of the structure. Similarly, in case of waveguides with gain layers, the gain of a guided mode is limited to that of the layer with the highest gain in the structure. Thus, if the gain is shown by a negative $\tilde{\alpha}$ the following inequality governs the attenuation constant of a guided mode;

$$\min(k_i) \leq \tilde{\alpha} \leq \max(k_i). \tag{5.21}$$

In ordinary dielectric waveguides which are intended for passive optical elements, such as interconnects or couplers, the loss is not desirable; thus, the constituent materials should not impose much attenuation on the mode. Consequently, the value of $\tilde{\alpha}$ is very low and the complex propagation constant is located in the vicinity of the real axis in the complex $\tilde{\beta}\tilde{\alpha}$ plane. In photodetectors, especially when superconductive layers are present, the complex propagation constant is not close to the real axis and some of the lossy modes may not be extracted unless (5.21) is taken into account explicitly.

Therefore, the proper contour is C_2 in Figure 5.2, i.e. the rectangle whose lower left vertex is $\Big(\max(n_s, n_c), \min(k_i)\Big)$ and upper right vertex $\Big(\max(n_i), \max(k_i)\Big)$. If the contour C_1 in Figure 5.2 is chosen for the integration, the substrate leaky modes are obtained.

The order of the polynomial that should be solved for extraction of the dispersion equation's roots equals to the number of the modes in the integration contour. For the sake of precision of the results, it is necessary to avoid solving polynomials of order more than four. To this end, the proposed contour can be divided into smaller contours, each of which enclosing at most four roots. Since checking the number of roots within a contour is an easy task, a recursive algorithm may be employed to divide the contour as many times as required to avoid solving high-order polynomials.

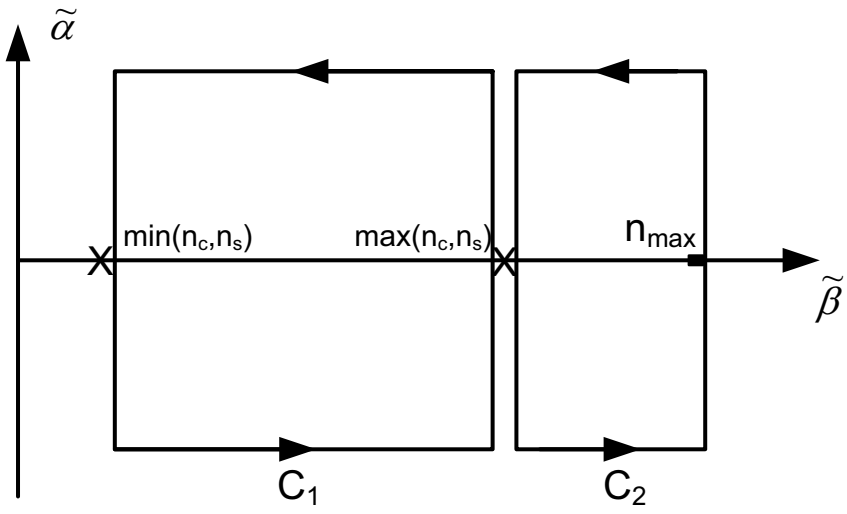

Figure 5.2: Proper Contours to find guided and leaky modes.

5.3.3 Numerical Integration

In order to numerically integrate a function $f(z)$ over an interval $[a, b]$, the integral is approximated by a quadrature sum

$$\int_a^b f(z)dz = \sum_{i=1}^{N} w_i f(z_i). \tag{5.22}$$

The choice of the nodes z_i and the weights w_i could be done with respect to the special characteristic of the integrand function. Nevertheless, for the dispersion equation in hand, no specific assumption is made and the nodes and weights are chosen as if the integrand is an arbitrary function. A 7-point Gaussian rule $G_7 f$ and a 15-point Kronrod rule $K_{15} f$ are used to estimate the integration along a straight line [111]. If the difference between these two methods is less than an acceptable tolerance, the $K_{15} f$ is considered as the answer of

the integral since it is more accurate than $G_7 f$. Otherwise, the interval is divided into two halves and the integration is repeated on each one [107]. The procedure could be continued until a satisfactory result for the integral is obtained.

5.4 Buffered Optical Waveguides with Low-Index Interlayers

The implementation of superconductive optical waveguides involves some significant challenges. Neither the fabrication techniques nor the materials used in conventional optical waveguides are directly applicable to superconductive optical waveguides. For instance, high-quality superconducting films require direct deposition on top of certain substrates or buffer layers whose optical refractive indices are usually much higher than that of the superconducting layer. This problem is more severe for high-temperature superconductors (HTS) which have a broader range of applications. A high-index substrate is classically avoided in the design of conventional dielectric waveguides, because the optical power leaks into the substrate. If the substrate possesses the highest refractive index among all the layers, no guided-mode will result. Although the structure still could be used as a waveguide based on its leaky modes, the mode would suffer from extensive radiation loss. The deployment of thick low-index interlayers and buffer layers presents a remedy for the design of superconducting optical waveguides based on mimicking their dielectric counterparts. The thick low-index interlayer is grown on top of the high-index substrate in order to optically decouple it from the rest of structure; thereby, taking the role of a virtual substrate. The actual substrate will only provides the mechanical stability for the structure. To prevent degradation of the quality of the superconducting film a lattice-matched buffer layer should be deposited before the HTS. In practice, the decoupling of the guide from the substrate

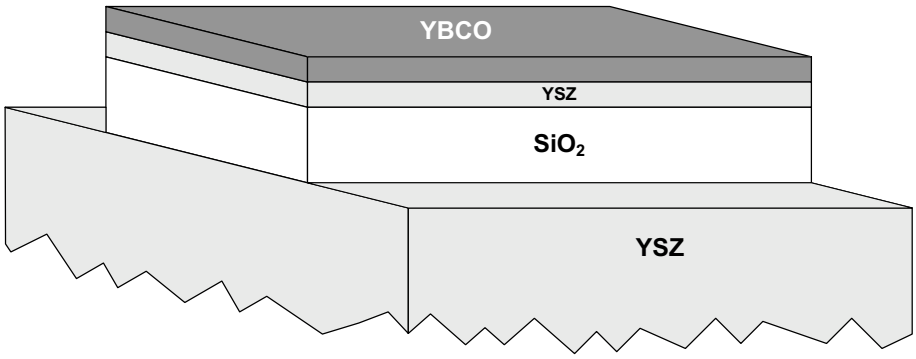

(a)

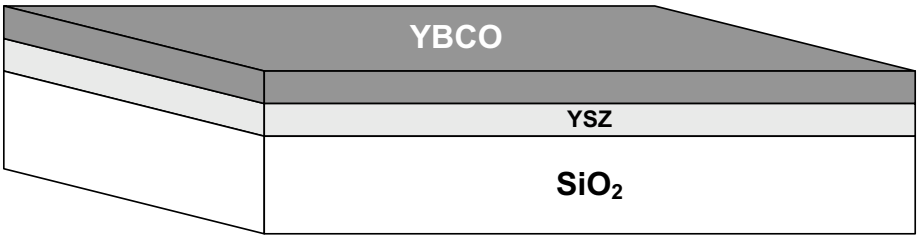

(b)

Figure 5.3: The schematic of a superconducting optical waveguide based on a low-index interlayer and a buffer layer (a) the real structure (b) the equivalent optical guide.

requires that the thickness of the low-index interlayer to be several times of the wavelength. The thicker the interlayer, the lower the power leakage. Figure 5.3a illustrates the physical structure of a YBCO superconducting optical waveguide with a YSZ substrate and buffer layer using SiO_2 as the low-index interlayer. The effective optical guide is depicted in Figure 5.3b. This structure was initially designed for multichip interconnect applications, whose fabrication procedure can be found in [112], and was first proposed as an optical waveguide in [86, 113].

Generally, the thickness of some layers in a waveguide might be determined by the

Table 5.1: Simulated guided modes of the superconductive waveguide with $n_s = 1.45$, $n_1 = 2.2$, $n_2 = 1.60 - j0.48$, $n_c = 1.0$ with $d_1 = 350nm$ and $d_2 = 150nm$.

Mode	$\tilde{\beta}$	$\tilde{\alpha}$
TE_0	2.0402	0.0147
TE_1	1.5604	0.0790
TM_0	1.9712	0.0432
TM_1	1.4541	0.1160

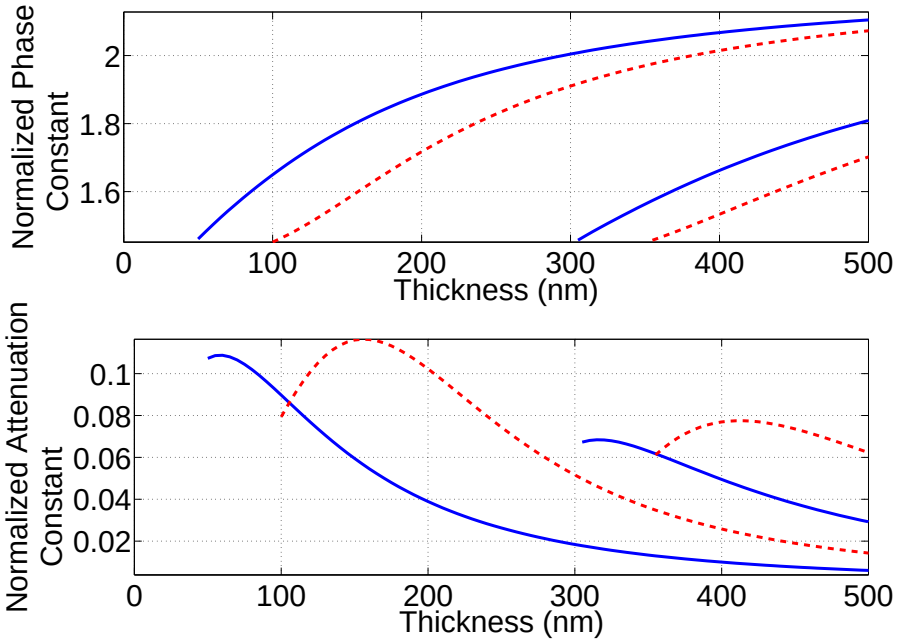

Figure 5.4: Simulated dispersion curves associated with the TE and TM modes of the waveguide with $d_{YBCO} = 100nm$ and variable thickness of YSZ layer. The solid line curves and the dashed line curves are respectively represent with TE and TM modes.

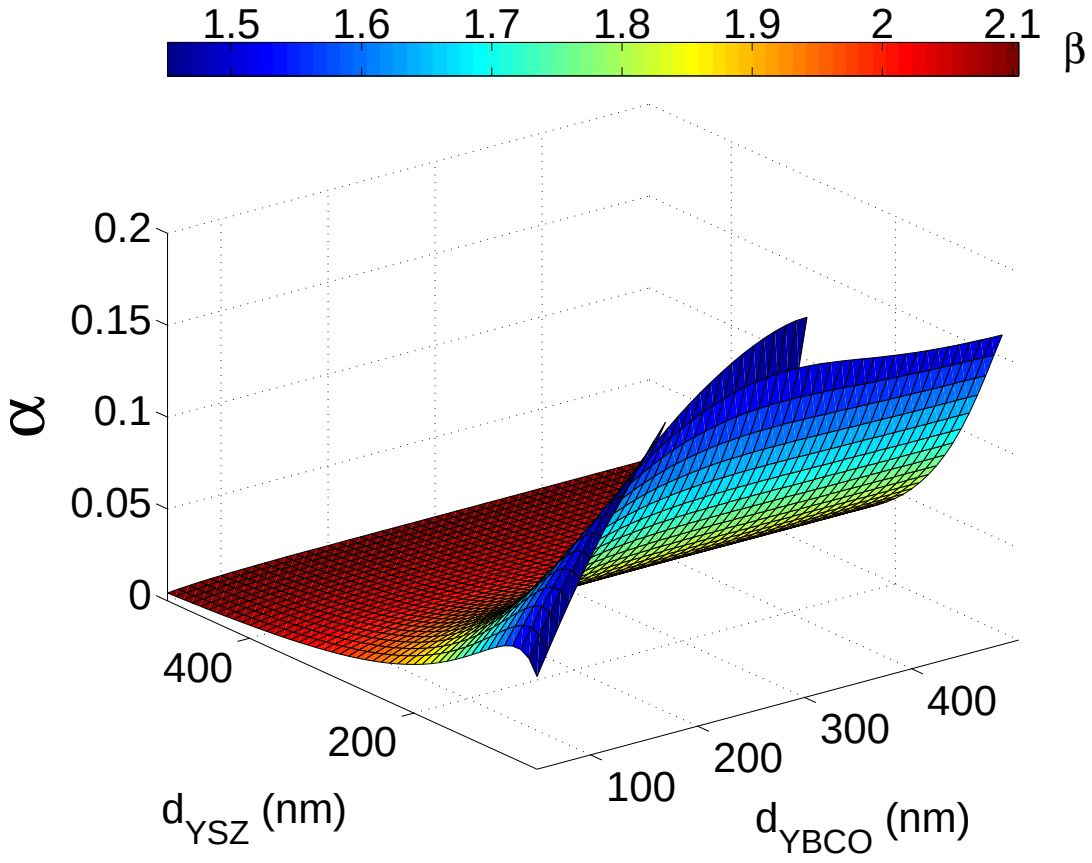

Figure 5.5: Simulated dispersion surface of the fundamental TE mode of the waveguide of Figure 5.3b for varying thicknesses of the YSZ and the superconductive layers. The color of each point on the surface is associated with the normalized phase constant of the mode.

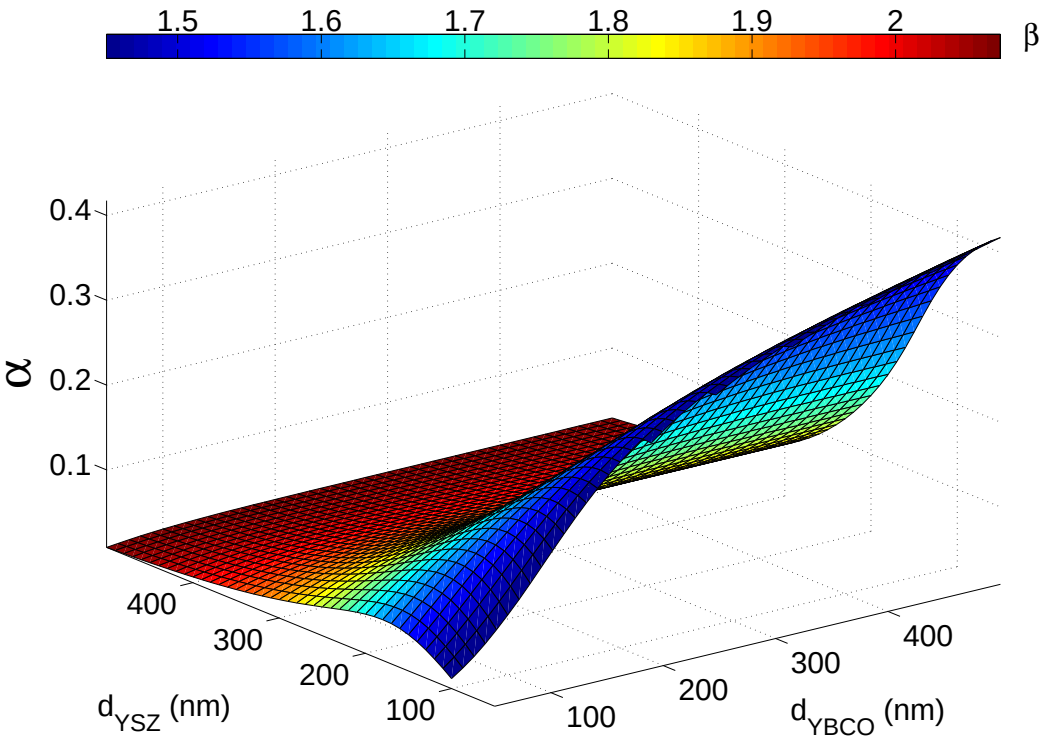

Figure 5.6: Simulated dispersion surface of the fundamental TM mode of the waveguide of Figure 5.3b for varying thicknesses of the YSZ and the superconductive layers. The color of each point on the surface is associated with the normalized phase constant of the mode.

fabrication technology. For instance, it is difficult to fabricate HTS films thinner than 70nm - 80nm or thicker than 300nm. Assuming $d_{YSZ} = 350$nm and $d_{YBCO} = 150$nm, as a typical example, the complex propagation constant of the guided modes of the waveguide are listed in Table.I. Nevertheless, for the purpose of design of a suitable waveguide, it is usually of great help to sweep over a parameter of interest, such as the thickness of a layer, for examining the modal dispersion. Figure 5.4 shows an example of such a dispersion curve associated with the varying thickness of YSZ layer and a fixed thickness of the superconductive film. One can readily observe the cut-off thickness of the fundamental and the second order modes. Thus, if the thickness of the YSZ layer is less than 50nm, no guided mode is available in the device. An interesting case is when the thickness of YSZ layer is between the cut-off thickness of the TE mode and that of the TM mode; where only the TE mode may propagate in the device and the detector exhibits high efficiency for a perpendicular polarization of light. Therefore, this regime is suitable for any possible polarization selective application. Other interesting designs may be proposed by means of optimizing the thickness of both the YBCO and the YSZ layers, some of which will be discussed in the next chapter. Figure 5.5 and Figure 5.6 depict the result of such analysis as two dispersion surfaces for TE and TM modes, respectively.

5.5 Plasmonic Optical Waveguides

Surface Plasmon Polariton (SPP) waves at a metal-dielectric boundary provide an alternative mechanism for guiding the light [70, 77, 92, 114]. In most of the conventional plasmonic optical waveguides, the interface of a low-loss dielectric and a metal supports the plasmonic surface wave, where the mode suffers from the dissipation by the metal. This high attenuation is considered to be the predominant problem for passive plasmonic devices [115, 116].

In active optoelectronic devices, such as photodetectors, the active region should absorb the light, therefore the associated optical guided-mode is necessarily lossy. Thus, for active optoelectronic devices, the main requirement is to maximize the absorption of the optical power by the active region, namely the coupling efficiency.

The generic structure proposed for superconductive plasmonic optical waveguides, as shown in Figure 5.7, consists of a metal-clad HTS film, where the HTS film constitutes the active region and is deposited immediately on a high-index substrate [117, 118]. Surface Plasmon-mediated coupling of power to superconductive structures substantially simplifies the fabrication process and is widely applicable to guided-wave superconductive optoelectronic devices. However, this structure differs from conventional plasmonic optical waveguides in two ways. First, the plasmonic interface supporting the electromagnetic surface wave includes a highly-lossy HTS-metal boundary, rather than a low-loss dielectric-metal boundary. Second, a high-index semi-infinite medium is present in the vicinity of the metal-dielectric boundary.

The high extinction factor of widely-used HTS films, such as YBCO and TBCCO, will be shown to be the main cause of absorption and dominate the loss in the metal, whereas the absorption in the metal is the primary cause of loss in conventional low-loss dielectric-metal plasmonic waveguides. The presence of the high-index substrate in close proximity of the supporting plasmonic boundary modifies the modal characteristics of the resulting SPP mode from those of the widely-used (a)symmetrically dielectric-loaded metal slabs. Specifically a sharp cut-off is seen for increasing thickness of the HTS layer, which coincides with the maximum coupling efficiency to the HTS layer. The cut-off thickness as well as the maximum coupling efficiency depend on the index contrast between the substrate and the HTS film, where both improve for a lower mismatch. Interestingly, in the regime of interest, the contribution of the metal to the optical loss is subordinate, provided that the

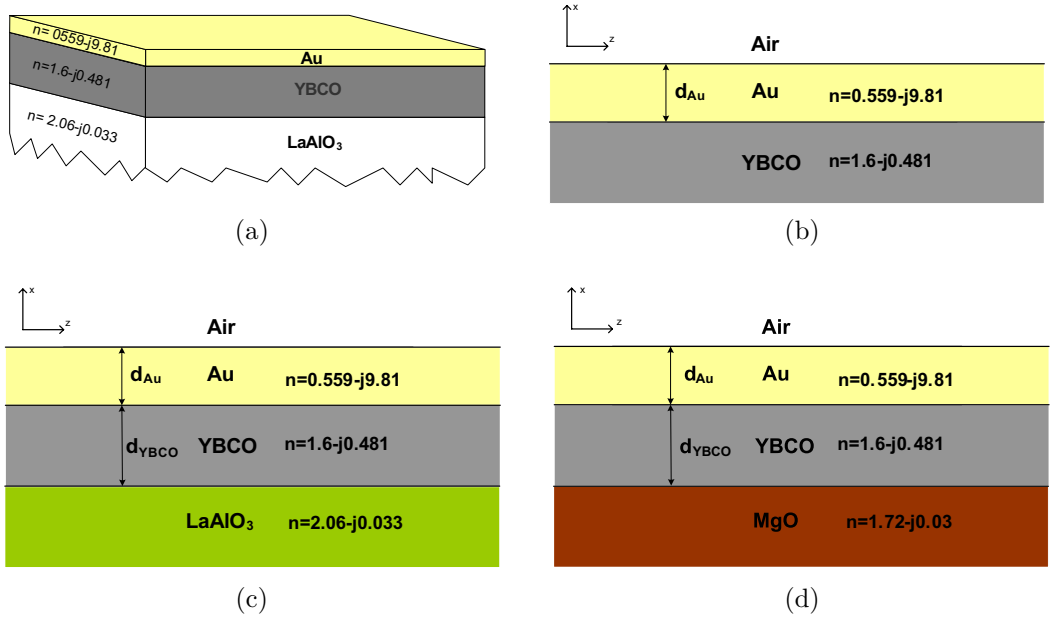

Figure 5.7: Physical structure of a superconductive plasmonic optical waveguide based on a metal-clad HTS layer deposited on a high-index substrate. (a) Physical structure of a YBCO-Au bilayer on a high-index $LaAlO_3$ substrate; (b) the limit of an extremely thick HTS layer, where the SPP wave is decoupled from the substrate; (c) $LaAlO_3$-YBCO-Au structure as a superconductive plasmonic optical waveguide; (d) MgO-YBCO-Au structure as a superconductive plasmonic optical waveguide.

thickness of the metal is sufficiently high to decouple the metal-HTS surface plasmon from the air cladding.

The general structure which is studied in this section consists of a metal-clad HTS layer deposited on a high-index substrate, as shown in Figure 5.7a. The structure of Figure 5.7b shows a limiting case, where the thickness of the HTS layer is sufficiently large in order to decouple the SPP wave from the substrate. The dispersion of the complex propagation constant for this structure is depicted in Figure 5.8a. For extremely thin Au layers, the effective phase constant β_{eff} and attenuation constant α_{eff} diverge. This behavior represents a cut-off. For thicker Au layers, the Au-YBCO SPP wave begins to decouple from the air cover and the complex propagation constant approaches to that of

a SPP wave at the boundary of semi-infinite Au and YBCO media, i.e. $1.6132 - j0.502$. Figure 5.8b demonstrates that the absorption largely occurs in the HTS; and is more than 0.99 for large d_{Au}. Therefore, increasing the thickness of the Au layer beyond the point where the Au-YBCO SPP wave is decoupled from the air, does not affect the absorption efficiency of the HTS layer.

Figure 5.9 and Figure 5.10 show the modal characteristics of the waveguides of Figure 5.7c and Figure 5.7d, respectively. These cases represent more practical situations, in which the HTS layer is thin and the presence of the high-index substrate is of critical significance. Figure 5.9a and Figure 5.10a clearly demonstrate the existence of a cut-off for increasing thickness of the YBCO layer. While the effective index of the mode, i.e. β_{eff}, decreases for increasing d_{YBCO}, the mode cuts off when its effective index equals the refractive index of the YBCO. The cut-off thickness is higher for the MgO substrate whose refractive index is smaller than that of the $LaAlO_3$ substrate. The attenuation constant however, increases with increasing YBCO thickness, since optical power will propagate dominantly through the HTS layer whose extinction factor is higher than both of the substrates. This fact directly affects the absorption efficiency of all the layers, as illustrated in Figure 5.9b and Figure 5.10b. The absorption efficiency of the YBCO active layer increases with increasing d_{YBCO}, whereas the absorption of both the substrate and the metal decrease. Close to the cut-off, the efficiency of coupling to the active layer is as high as 60% and 70%, respectively for the waveguides on the $LaAlO_3$ and MgO substrates. Interestingly, the dominant unuseful absorption, in both cases is the loss in the substrate not the metal. It is readily seen that the extinction factor of both substrates are much higher than that of the substrates used in conventional optical waveguides. Close to the cut-off, the loss associated with the absorption by the metal, which supports the SPP wave, is less than 10%.

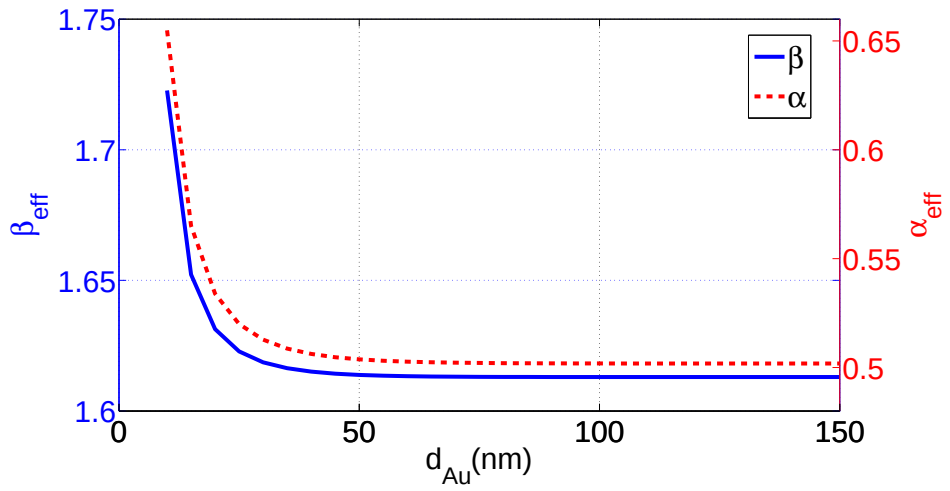

(a)

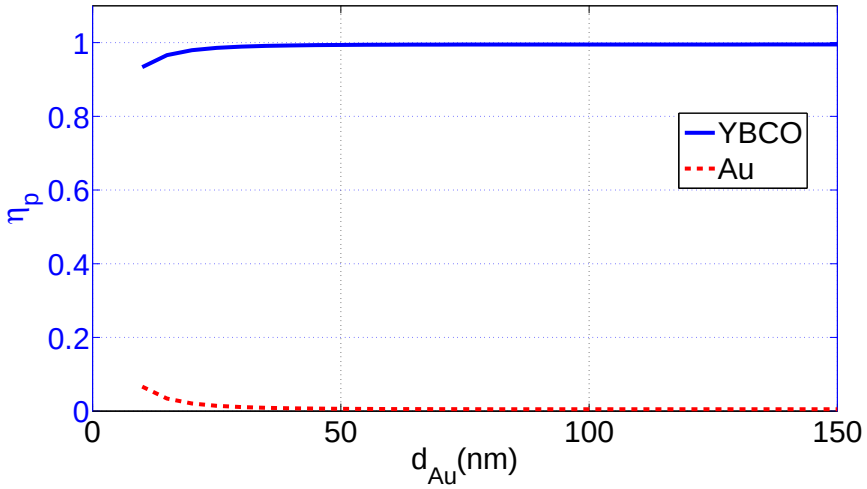

(b)

Figure 5.8: Simulated dispersion curves and coupling efficiency of a YBCO-Au waveguide in the thick-HTS limit, as a function of the metal thickness, at a wavelength of 1550nm. (a) Effective phase and attenuation constants; (b) absorption efficiency of different layers.

Although a great portion of the optical power is still absorbed by layers other than the active layer, the coupling efficiency is much higher comparing to unguided illumination schemes, where the coupling efficiency is well below a few percent. Other advantages of guided-wave optoelectronics, such as extended bandwidth and advanced traveling-wave architectures, apply to plasmonic devices as well and will be exploited in the next chapter. A typical setup and associated techniques for the excitation and the characterization of plasmonic optical waveguides are briefly presented in Appendix B, where several surface plasmon waveguides are experimentally tested.

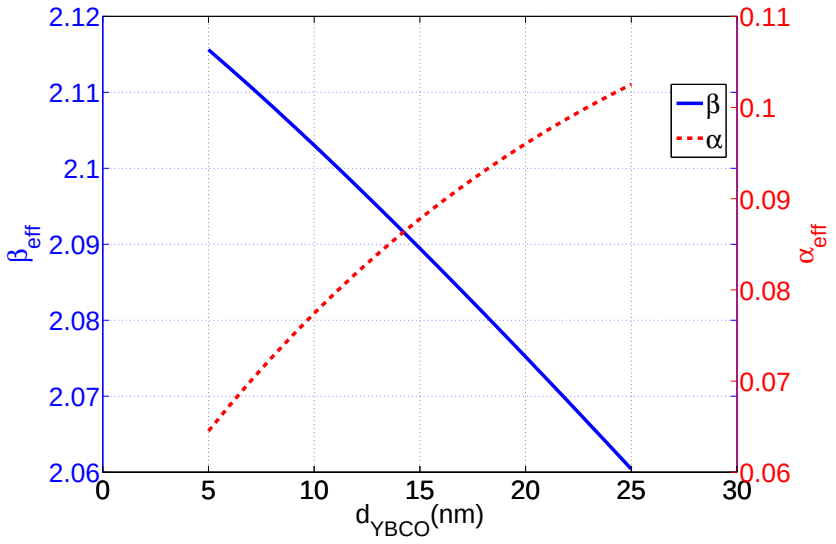

(a)

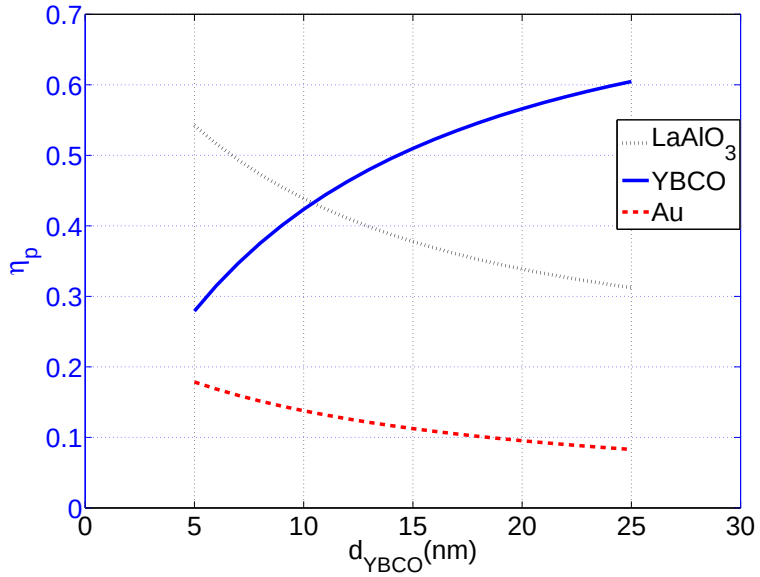

(b)

Figure 5.9: Simulated dispersion curves and coupling efficiency of a $LaAlO_3$-YBCO-Au waveguide, as a function of the HTS thickness, at a wavelength of 1550nm. (a) Effective phase and attenuation constants; (b) absorption efficiency of different layers.

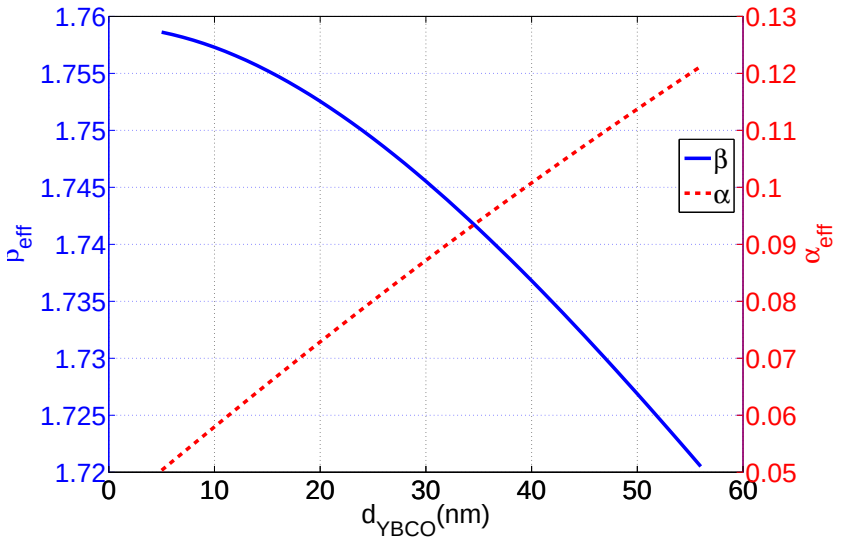

(a)

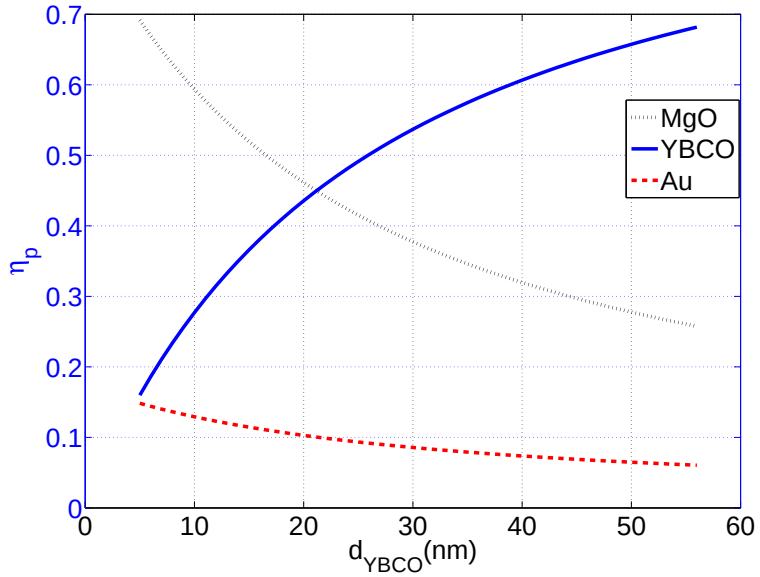

(b)

Figure 5.10: Simulated dispersion curves and coupling efficiency of a MgO-YBCO-Au waveguide, as a function of the HTS thickness, at a wavelength of 1550nm. (a) Effective phase and attenuation constants; (b) absorption efficiency of different layers.

5.6 Summary

This chapter introduced superconducting optical waveguides for advanced optoelectronic applications. A general formulation of the dispersion equation of the superconductive optical waveguide was presented based on the transfer matrix method. Subsequently, an efficient and robust numerical tool capable of finding the guided and leaky modes of the waveguide was introduced based on the Cauchy integral method and the argument principle method. It was pointed out that the ability of this method to find the optical modes without an initial guess as well as its capability to treat lossy waveguides in a natural way are central to the robustness and generality of the subsequent techniques. According to the presented methods, two specific structures were proposes as superconductive optical waveguides. The first design relies on a dielectric-waveguide approach and utilizes a low-index interlayer and a buffer layer to accommodate the existence of a high-index substrate, which is often needed for the deposition of high-quality superconducting films. The second design uses SPP modes of a metal-clad superconducting film as an optical guided wave. This strategy simplifies the fabrication and improves the coupling efficiency to the active superconducting layer.

Chapter 6

Superconductive Traveling-Wave Photodetectors

6.1 Introduction

Kinetic-inductive photodetection was demonstrated in chapter 2 as a means for ultra-fast and ultra-sensitive optoelectronics. However, there are several problems associated with a simple lumped-element device, such as low responsivity, inefficiency of optical coupling, and the limiting R-L time constant. A possible remedy to enhance the responsivity and eliminate the lumped-element time constant is changing the architecture of the device into a distributed one. This goal can be achieved when the photodetection takes place along a transmission line, rather than a lumped-element micro-bridge [83, 86, 119]. For instance, the center stripe of a coplanar waveguide(CPW) can play the role of the kinetic-inductive photodetector. To this end, it is necessary that the optical power be guided over the the transmission line; thus, the integration with an optical waveguide is required [98, 113, 118]. The device resulting from the integration of the thin film kinetic-inductive photodetector,

the microwave transmission line, and the optical waveguide will be distributed both electrically and optically, namely a superconductive traveling-wave photodetector (STWPD) [86].

Traveling-wave photodetectors have already been proved to be very successful in semiconductor optoelectronics [120–122]. A number of devices have been introduced, in which p-i-n diodes [120–123], metal-semiconductor-metal(MSM) junctions and Schottky barriers [81,82,85] are integrated with a transmission line and an optical waveguide. The device function is not limited to detection, but also includes traveling-wave amplification [124] and THz signal generation [81]. In fact, STWPDs have been also shown to be very promising as traveling-wave photomixers for THz wave generation [83, 86].

6.2 Device Concept

Figure 6.1 shows the schematic of an STWPD. The device consists of a microwave transmission line with superconducting strips and an optical waveguide. The transmission line in Figure 6.1 is a CPW, however this is not essential to the device operation and a microstrip or any other planar transmission line could be used as well. The center strip of the CPW serves as the distributed kinetic-inductive photodetector. The center strip may be externally current biased using a bias-T. The optical waveguide is a planar multilayer structure, whose length is determined by the modal attenuation constant of the guide. The center strip is also a part of the optical waveguide and directly contributes to the modal characteristics of the optical propagation. The optical waveguide is a lossy waveguide due to the presence of a superconducting layer. Ideally, it is desirable that the superconducting layer be the only absorptive layer of the waveguide, which assures that the loss is only due to absorbtion of the light by the detecting element.

As the input light propagates down the waveguide, it is attenuated due to absorption

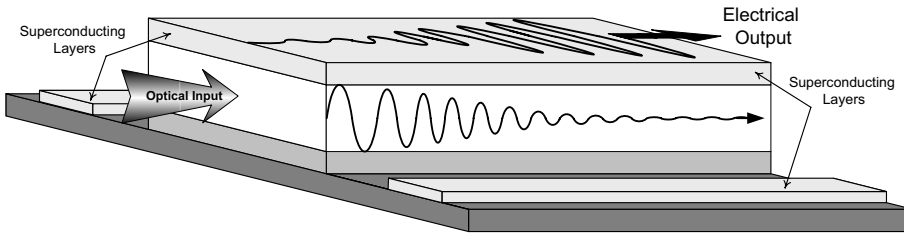

Figure 6.1: Schematic of operation of an STWPD. The structure consists of a CPW transmission line with superconducting electrodes integrated with a multilayer optical waveguide.

by the superconductive layer. At every point on the device, the absorbed optical power is converted to a local voltage as the result of the kinetic-inductive photoresponse. The role of the transmission line is to constructively collect the locally generated voltages, and delivers the photogenerated electrical power to the load at the device output. Therefore, an electrical wave co-propagates with the optical signal along the device. For constructive interference of the local voltages, it is required that the phase velocity of the transmission line matches to the group velocity of the optical waveguide [86]. In fact, it can be shown that the effective bandwidth of traveling-wave devices is primarily determined by this velocity mismatch [120, 122]. Hence for broadband operation, the integrated structure needs to be designed for optimal velocity matching.

6.3 Distributed Photodetection along a Superconducting Transmission Line

Assume that the input optical signal is $P(t) = P_0[1 + \cos(\omega_e t)]$ at the front end of the device $z = 0$; and is completely coupled to a guided mode of the waveguide with a complex propagation constant $\gamma_o = \beta - j\alpha$. The instantaneous optical power flowing at each point

down the waveguide is

$$P(t,z) = P(t - z/v_o, 0)e^{-2\alpha z}, \tag{6.1}$$

where $v_o = (\partial\beta/\partial\omega_o)^{-1}$ is the group velocity of the optical signal and ω_o is the light's frequency . Suppose that ξ_s is the optical absorption efficiency, which is defined as the ratio of the absorbed power by the superconductive film to the total power loss in a unit length of the waveguide in the $+z$ direction. If the superconductive film is the only absorptive layer of an ideal waveguide then $\xi_s = 1$. Therefore, the absorbed power density by the superconductive film, $A_s(t,z) \equiv -\xi_s \frac{dP}{dz}$, at a distance z from the waveguide's input is

$$A_s(t,z) = 2\alpha\xi_s P_0 \left[1 + \cos(\omega_e t - \frac{\omega_e}{v_o} z)\right] e^{-2\alpha z}. \tag{6.2}$$

Using (2.38), the phasor form of the photogenerated voltage at point z is obtained as

$$v_{ph}(z) = k_v e^{-\Gamma_o z}, \tag{6.3}$$

where

$$\Gamma_o = 2\alpha + j\frac{\omega_e}{v_o}, \tag{6.4}$$

and the voltage conversion factor k_v is defined as

$$k_v \equiv 2\alpha\xi_s P_0 R_v(\omega_e). \tag{6.5}$$

The voltage conversion factor k_v, represents the strength the device in converting optical power into electrical voltage. Devices with a small value of k_v need to have long optical waveguides in order to convert all of the input optical power to the electrical domain, whereas large k_v usually corresponds to small devices. According to (6.5), high-k_v devices

must have very lossy optical waveguides; since k_v is directly proportional to the absorbtion constant α of the waveguide. This in turn limits the range of linear operation of the device, where superconductivity ought to persist and must not be destroyed.

6.3.1 The Effect of an Additional Photoconductive Layer

Equation (2.38) readily implies that the responsivity of a superconductive film drops off linearly at low frequencies. In general, the photoresponse of a superconductive film is of a band-pass nature, which is suitable for high frequency signal generation by means of detecting the beat frequency of two mixed optical signals [83, 119]. However, for broad-band photodetection, one may be concerned about low frequencies as well. The inclusion of a photoconductive layer in the optical waveguide is a solution to compensate for low responsivity of the device at low frequencies.

Assume that η_p is the internal quantum efficiency, τ_L is carrier life time and ξ_p is the optical absorption efficiency of the photoconductive layer. If the photoconductive and superconductive layers are the only absorptive layers of an ideal waveguide then $\xi_p = 1-\xi_s$. The absorbed power density by the photoconductive layer is

$$A_p(t,z) = 2\alpha\xi_p P_0 \left[1 + \cos(\omega_e t - \frac{\omega_e}{v_o} z)\right] e^{-2\alpha z}. \tag{6.6}$$

Thus, the phasor form of the photogenerated current is

$$i_{ph}(z) = k_i e^{-\Gamma_o z}, \tag{6.7}$$

where

$$R_i(\omega_e) = \frac{\eta_p q}{\hbar\omega_o}\left(\frac{\tau_L}{\tau_t}\right)\left(\frac{1}{1+j\omega_e\tau_L}\right), \tag{6.8}$$

and τ_t is the transit time of the carriers [125]. The current conversion factor k_i is defined as

$$k_i \equiv 2\alpha\xi_p P_0 R_i(\omega_e). \tag{6.9}$$

6.4 Modified Transmission Line Theory for Traveling-Wave Photodetection

If the superconductive thin film is part of a transmission line, then the effect of photodetection can be considered as distributed voltage and current sources, whose amplitude and phase follow the equations (6.3) and (6.7). The equivalent circuit of a differential length of the transmission line is shown in Figure 6.2. The impedance Z is the equivalent series impedance of the transmission line, including the magnetic and kinetic inductances and the series resistance. The admittance Y is the equivalent shunt admittance of the transmission line, including the conductance and capacitance of the photoconductive layer.

In general, both Z and Y depend on the geometry of the transmission line. Analytical expressions for Z and Y as well as the electrical complex propagation constant $\Gamma_e = \sqrt{ZY}$ for superconductive parallel plate transmission line and coplanar waveguide can be found in [119] and [83], respectively.

The time harmonic form of transmission line equations for the transmission line of Figure 6.2 are

$$\frac{d^2}{dz^2}v(z) - \Gamma_e^2 v(z) = (Zk_i + k_v\Gamma_o)\, e^{-\Gamma_o z}, \tag{6.10}$$

and

$$\frac{d^2}{dz^2}i(z) - \Gamma_e^2 i(z) = (Yk_v + k_i\Gamma_o)\, e^{-\Gamma_o z}. \tag{6.11}$$

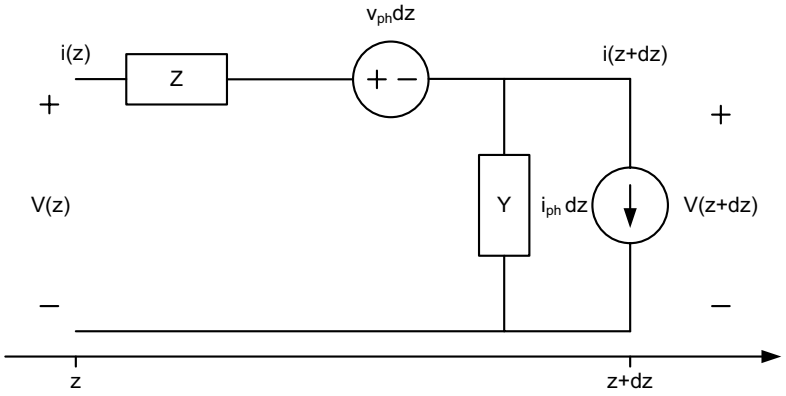

Figure 6.2: Equivalent circuit model of a differential length of a thin film STWPD.

The analytical solutions of the above differential equations are

$$v(z) = v_+ e^{-\Gamma_e z} + v_- e^{\Gamma_e z} + \frac{Zk_i + k_v\Gamma_o}{\Gamma_0^2 - \Gamma_e^2} e^{-\Gamma_o z}, \tag{6.12}$$

and

$$i(z) = \frac{v_+}{Z_0} e^{-\Gamma_e z} - \frac{v_-}{Z_0} e^{\Gamma_e z} + \frac{Yk_v + k_i\Gamma_o}{\Gamma_0^2 - \Gamma_e^2} e^{-\Gamma_o z}, \tag{6.13}$$

where $Z_0 = \sqrt{Z/Y}$ is the characteristic impedance of the transmission line and v_+ and v_- are the amplitudes of forward and backward traveling voltage waves, which should be found from the boundary conditions. There are three sets of terminations which are of practical interest. In the first case the input is open circuited and the output is matched:

$$\frac{v(\ell)}{i(\ell)} = Z_0 \qquad \textit{and} \qquad i(0) = 0. \tag{6.14}$$

If the length of transmission line is ℓ, then

$$v_- = \frac{Z_0 k_i - k_v}{2(\Gamma_o + \Gamma_e)} e^{-(\Gamma_o + \Gamma_e)\ell}, \tag{6.15}$$

and

$$v_+ = v_- - \frac{k_v \Gamma_e + Z_0 k_i \Gamma_o}{\Gamma_o^2 - \Gamma_e^2}. \tag{6.16}$$

The second case is when the input is short circuited and the output is matched:

$$\frac{v(\ell)}{i(\ell)} = Z_0 \qquad and \qquad v(0) = 0. \tag{6.17}$$

This set of loading provides more flexibility in biasing the device. In this case v_- is obtained from (6.15) and v_+ is given as

$$v_+ = -v_- - \frac{Z_0 k_i \Gamma_e + k_v \Gamma_e}{\Gamma_o^2 - \Gamma_e^2}. \tag{6.18}$$

The third case, which is suitable for broadband operation of the device, is when both input and output are matched

$$\frac{v(\ell)}{i(\ell)} = Z_0 \qquad and \qquad \frac{v(0)}{i(0)} = -Z_0. \tag{6.19}$$

In this case v_- is again represented by (6.15) and v_+ is

$$v_+ = -\frac{Z_0 k_i + k_v}{2(\Gamma_o - \Gamma_e)}. \tag{6.20}$$

6.5 Device Performance

In this section, the quantum efficiency and bandwidth of STWPDs are examined as the two most important device performance parameters.

6.5.1 Quantum Efficiency

There are three prominent and potentially inefficient mechanisms in the operation of STWPDs. First, the coupling of the incoming light into the guided modes of the optical waveguide leads to the definition of "coupling efficiency" η_{cop}. Second, the absorbtion of light by the layers that contribute to photodetection might be inefficient. It is likely to have dissipative layers other than those which contribute to photodetection. Also, the non-ideal geometry and material defects might impose other losses through radiation and/or scattering of light. Therefore, if the useful absorption occurs in the layers whose index i belongs to the set U, then the overall "absorption efficiency" is

$$\eta_{abs} \equiv \sum_{i \in U} \xi_i, \tag{6.21}$$

where ξ_i is the absorption efficiency of the i'th layer. The third potentially inefficient mechanism is delivery of the photogenerated electrical power to the load. This inefficiency is due to the loss in the microwave transmission line and load-line impedance mismatch and is represented as a whole by η_{TL}.

There is yet another hidden, but potentially inefficient mechanism. In fact, the contribution of the absorbed photons to photodetection is not absolutely perfect; and leads to the definition of the term "quantum efficiency". Quantum efficiency can be defined in several different ways. The conventional definition is the one used in semiconductor opto-

electronics, i.e. the ratio of the average number of charge carriers generated to the number of absorbed photons. This definition is suitable for possible photoconductive layers in the device. Nevertheless, in superconductors a photon of sufficient energy might generate hundreds of quasi-particles. The conventional definition of quantum efficiency does not carry explicit information about efficiency of the process here [1]. The photon-induced pair breaking happens as a series of events mediated by phonon-electron and electron-electron scattering as well as the condensate reaction through the self-consistency relation [6,37,38]. Hence, the quantum efficiency of the superconductive layer(s) is defined as the ratio of the average actual number of broken Cooper pairs to its maximum possible value ($P_0\tau_Q/2\Delta$).

Thus, it is helpful to combine the absorption and quantum efficiencies into a single parameter called "internal quantum efficiency"

$$\eta_{int} \equiv \sum_{i \in U} \xi_i \eta_i, \tag{6.22}$$

where η_i is the quantum efficiency of the i'th layer. Calculation of ξ_i can be done based on the thorough analysis of the optical waveguide given in chapter 5. Having found the longitudinal propagation constant of the guided modes, it is straightforward to calculate analytically the field profile as well as power absorption in each layer and in turn the absorption efficiencies ξ_i. So, the "external quantum efficiency" of the device can be defined as

$$\eta_{ext} \equiv \eta_{cop}\eta_{int}\eta_{TL}. \tag{6.23}$$

[1] In fact, the term "quantum yield" is commonly used to refer to the average number of quasi particles generated per absorption of a photon in a superconductive film. A useful treatment of quantum yield can be found in [126].

6.5.2 Bandwidth

In principle, there are three issues that limit the bandwidth of STWPDs. The first one is the pair breaking time constant or the carrier life time τ_Q; which is usually in the order of the electron-phonon and electron-electron scattering time constant of the superconductor. For YBCO, these values are around $1.1ps$ and $0.9ps$ respectively [10]. Once operated in the linear regime, STWPDs are not limited by the carrier life time up to THz frequencies. Nevertheless, very close to T_c, the order parameter relaxation time is the dominant limiting factor [38, 45]. The second limiting issue is the carrier drift time in possible photoconductive layers. In fact, the role of the photoconductive layer is only to compensate for the low responsivity of the superconductive film at low frequencies. Since the kinetic inductive responsivity increases with frequency, whereas the photoconductive responsivity decreases, the contribution of photoconductive layer could be ignored at high frequencies. However, the carrier drift time may be reduced at will by shrinking the thickness of the photoconductive layer and using a longer waveguide. The third and the dominant factor which limits the bandwidth of STWPDs is the transient response of the distributed photodetection scheme. As will be seen shortly, this factor depends on the mismatch between group velocity of the optical signal and phase velocity of the electrical signal.

Assume that an optical impulse is applied to the input of a long STWPD. Because the light is not reflected back, the propagating optical signal as a function of time and position along the transmission line is

$$P(t,z) = P_0\delta(t - z/v_o)e^{-2\alpha z}, \tag{6.24}$$

and the absorbed power density by the superconductive film is obtained as

$$A(t,z) = 2\xi_s \alpha P_0 \delta(t - z/v_o) e^{-2\alpha z}. \tag{6.25}$$

Suppose that the photoresponse of the device is instantaneous, it can be modeled as two voltage impulses with equal amplitudes, one forward traveling wave and one backward traveling wave. In general, the output voltage of the transmission line is the superposition of the initially forward-traveling waves and the reflected part of the initially backward-traveling waves. If the input is matched, i.e. $\gamma_{in} = 0$, the output only consists of the initially forward-traveling waves. Thus, the device impulse response shortens and the bandwidth increases. Nevertheless, a matched input dissipates half of the photogenerated electrical power, therefore the efficiency of the device will be limited to 50%. In contrast, an open input, i.e. $\gamma_{in} = 1$, allows the entire photogenerated electrical power to be delivered to the load, however, at the expense of a prolonged impulse response and a restricted bandwidth. Assuming that the responsivity of the superconductive film is R, using an approach similar to [122], the output voltage is

$$v(t,\ell) = \int_0^\ell \frac{R}{2} A(t - \frac{\ell - z}{v_e}, z) dz + \gamma_{in} \int_0^\ell \frac{R}{2} A(t - \frac{\ell + z}{v_e}, z) dz. \tag{6.26}$$

Substituting (6.25) into (6.26) and carrying out the integration, the output voltage can be explicitly written as

$$v(t,\ell) = \alpha \xi_s R P_0 \left[v^+(t) + v^-(t) \right], \tag{6.27}$$

where

$$v^+(t) = \begin{cases} \frac{1}{|v_f|} e^{\frac{2\alpha}{v_f}(t - \frac{\ell}{v_e})} & \frac{\ell}{\max(v_o, v_e)} \leq t \leq \frac{\ell}{\min(v_o, v_e)} \\ 0 & \text{otherwise} \end{cases} \tag{6.28}$$

and

$$v^{-}(t) = \begin{cases} \frac{\gamma_{in}}{v_r} e^{\frac{-2\alpha}{v_r}(t-\frac{\ell}{v_e})} & \frac{\ell}{v_e} \leq t \leq \frac{\ell}{v_o} + \frac{2\ell}{v_e} \\ 0 & \text{otherwise} \end{cases}, \tag{6.29}$$

in which $v_{f,r} = \frac{v_o \mp v_e}{v_o v_e}$. Hence, the $3dB$ bandwidth of matched input and open input configurations are

$$BW_m = \frac{\alpha}{\pi} \frac{v_o v_e}{v_o - v_e}, \tag{6.30}$$

and

$$BW_o \simeq \frac{\alpha}{\pi} \frac{\sqrt{2} v_o v_e}{\sqrt{5v_o^2 - v_e^2}}. \tag{6.31}$$

respectively. The equations (6.30) and (6.31) obviously show that the matched input configuration provides much higher bandwidth for the same device. The enhanced bandwidth is at the expense of reducing the quantum efficiency to 50%, since half of the photogenerated power is absorbed by the input loading. Therefore, a very good figure of merit to evaluate the performance of a device is the bandwidth-efficiency product, as is used in conventional wide-band detectors [120–122].

6.6 Device Design

In this section, a sample STWPD device is designed based on the optical waveguide of Figure 5.3, whose detailed optical analysis was given in chapter 5. The thickness of the YBCO is assumed to be 100nm, which is a reliable thickness for fabrication of HTS materials. Moreover, the width of the superconductive film is taken to be $2\mu m$, which allows that optical lithography be used for patterning the device. The operating temperature is set at 77K for the sake of simplicity.

The responsivity of the superconductive film (2.38) is directly proportional to the bias

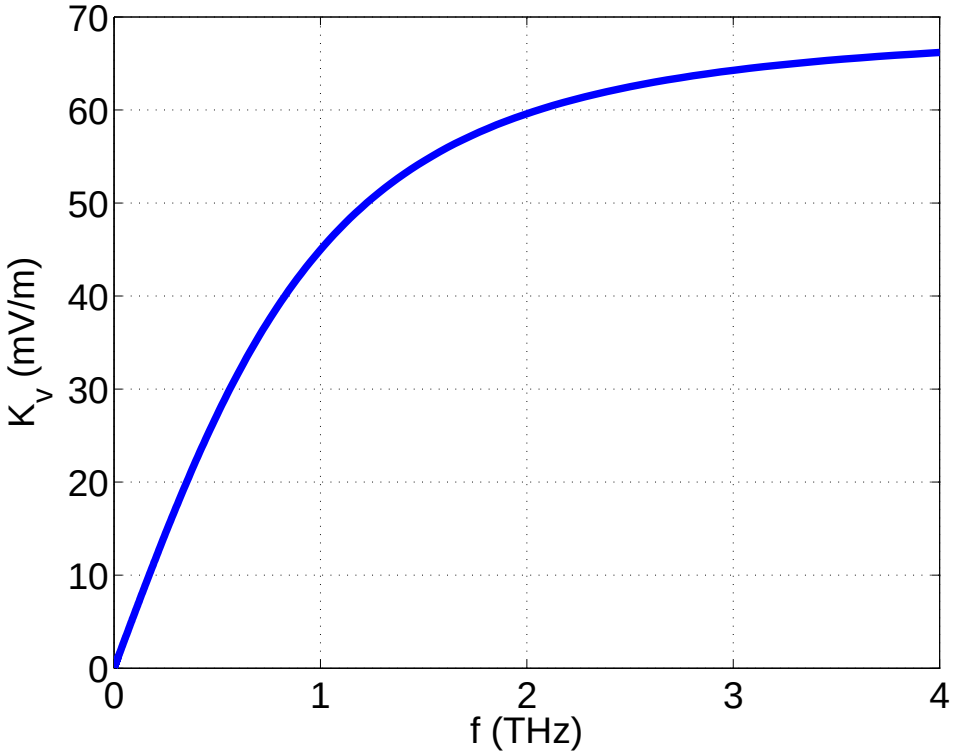

Figure 6.3: The simulated voltage conversion factor for an STWPD with a low-loss buffered YBCO-YSZ-SiO_2 waveguide, where d_{YBCO} = 100nm and d_{YSZ} = 400nm, at a temperature of 77K.

current I_0. However, I_0 must be chosen well below the critical current. The critical current density of the YBCO film, at the operating temperature is more than $1.2 \times 10^6 A/cm^2$ [112]; therefore, $I_B = 1mA$ is a suitable choice.

In order to complete the physical design, the thickness of the YSZ layer as well as the length of the waveguide need to be determined. A thick layer of YSZ results in a low-loss waveguide, whereas a thin layer of YSZ leads to a very lossy waveguide [98]. When the dynamic range of the photodetector is of primary importance, a low-loss waveguide is preferred. In contrast, in case the signal level is very low, a highly absorptive waveguide is necessary. To see this, assume that the maximum allowable power absorption per unit

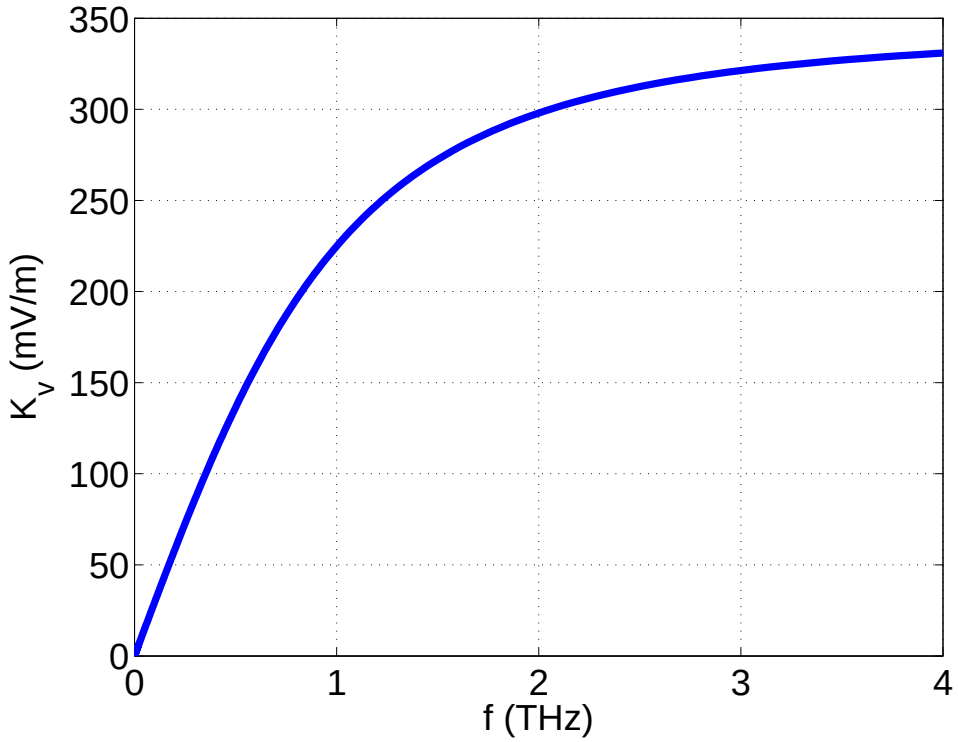

Figure 6.4: The simulated voltage conversion factor for an STWPD with a highly absorptive buffered YBCO-YSZ-SiO_2 waveguide, where d_{YBCO} = 100nm and d_{YSZ} = 170nm, at a temperature of 77K.

length of the superconductive film is P_{max}, as discussed in chapter 2. From (6.2), it is seen that the differential power absorption by the film is proportional to αP_0, in which α is the waveguide attenuation constant and P_0 is the total absorbed power in the device. For the same amount of P_{max}, it is obvious that the low-loss waveguide has a greater value of P_0. Of course the optical waveguide should be sufficiently long in order to absorb all the incident power. At a wavelength of $\lambda = 850nm$ and a YSZ thickness of 400nm, the normalized propagation constant for the fundamental TE mode is 2.07-j0.01, whereas for a YSZ thickness of 170nm it is 1.83-j0.05. In order to absorb 99% of the input optical power the device length should be ℓ=62.3μm and ℓ=12.5μm, respectively for the low-loss and highly absorptive waveguides. Figure 6.3 and Figure 6.4 illustrate the voltage conversion factor k_v for the two devices, respectively.

If the embedded microwave transmission line of the STWPD is perfectly velocity-matched with the optical waveguide and both ends of the line are load-matched, the overall responsivity of the devices is as shown by Figure 6.5.

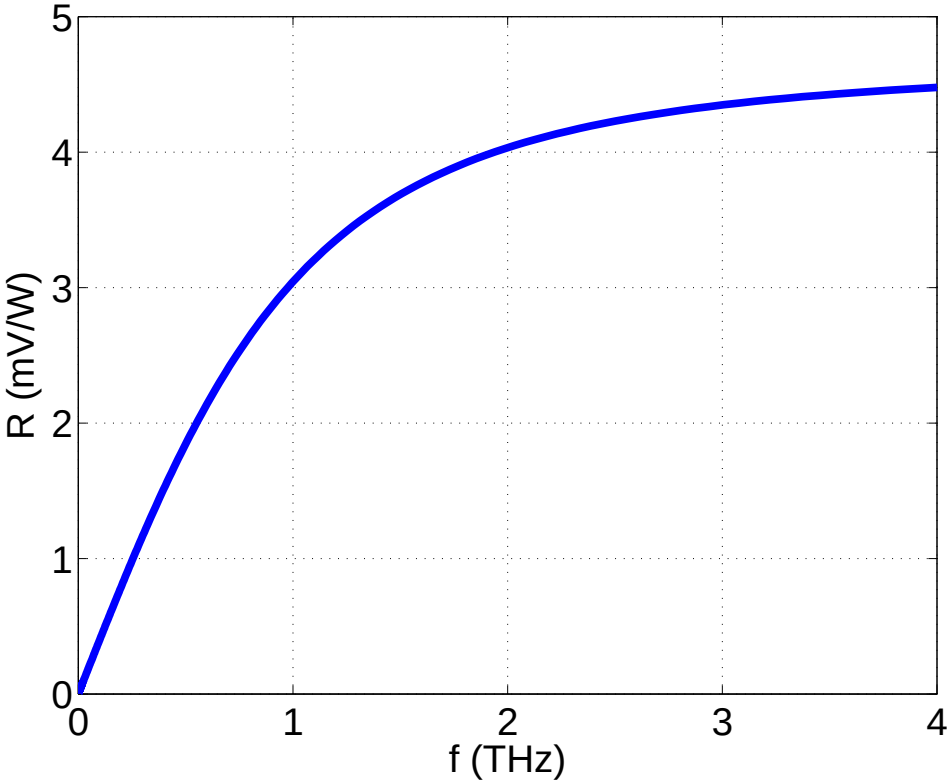

Figure 6.5: The simulated overall responsivity of the sample STWPD devices.

6.7 Summary

In this chapter, superconductive traveling-wave photodetector devices (STWPDs) were introduced as a general platform for ultra-fast, ultra-sensitive and ultra-low-noise optoelectronic devices. The basic mechanisms for the detection of light were examined based on the kinetic-inductance theory of thin films and the modified transmission-line model. While the emphasis was put on the photodetection, other optoelectronic functions, such as photomixing and signal generation, can be realized by means of a photodetector device fed by two slightly off-tuned optical inputs. The device performance parameters including the voltage/current conversion factor, overall responsivity, bandwidth, and efficiency were investigated. A sample structure consisting relevant materials used in a real device was designed. Different regimes of interest for various applications were discussed, and the overall performance of the sample device was simulated.

Chapter 7

Concluding Remarks

7.1 Summary and Results

This thesis has investigated guided-wave superconducting quantum optoelectronic devices as a novel platform for ultra-fast and ultra-sensitive optoelectronic and microwave-photonic functions.

The kinetic-inductive photoresponse of superconducting thin films has been studied in detail with emphasis on the linear response regime. The presented analysis takes the nonequilibrium and bolometric carrier life-times as two phenomenological inputs and predicts the macroscopic responsivity of the structure in terms of the material parameters and geometry. While the carrier life-times may be approximated by means of more fundamental theories, in practice these parameters should be extracted experimentally. The analysis is applicable both to lumped-element and distributed devices, and may conveniently account for the nonequilibrium and bolometric components. The kinetic-inductive photodetection scheme has been experimentally demonstrated by photoresponse measurements in current

driven YBCO meander-lines.

Several superconducting microwave transmission lines have been designed and measured, which serve as the microwave template for high-speed devices. Microwave-photonic devices, such as optically tunable resonators and delay lines, have been designed and measured based on the integration of a kinetic-inductive element and a microwave transmission line. To provide low-loss and low-dispersion propagation of millimeter-wave and THz signals, for ultra-fast and wideband photodetection as well as (sub)millimeter-wave photomixing, surface wave transmission lines have been introduced based on utilizing surface plasmon polariton modes of metal-dielectric-metal waveguides. Complete field analysis has been used to define voltage and current at such high frequencies, including the conditions of quasi-TEM propagation, and the associated line parameters have been derived accordingly.

The theory of superconducting optical waveguides has been developed to support advanced waveguide optoelectronic devices. An analytical formulation and an efficient numerical method has been presented to solve general multilayer slab waveguides comprised of arbitrary number of layers and materials including superconductors, metals, and dielectrics. The method has been applied to design several superconducting optical waveguides. It has been shown that for designs similar to dielectric waveguides, the problem of a high-index substrate may be rectified by means of including a thick low-index interlayer and appropriate buffer layers. Moreover, metal-HTS plasmonic waveguides have been introduced as an alternative technique with considerable ease in fabrication and a substantial enhancement in the coupling efficiency. Experimental setup for the excitation and characterization of metal strip plasmonic waveguides has been demonstrated and several long-range surface plasmon waveguides have been measured, as presented in appendix B.

Superconducting traveling-wave photodetectors have been proposed based on the integration of the distributed kinetic inductive photoresponse along a transmission line and superconducting optical waveguides for efficient and high-speed optoelectronic device applications. The device has been modeled using a modified transmission line theory, and the performance parameters, such as the bandwidth and efficiency, have been addressed. It has been speculated that the inclusion of an additional photoconductive layer may ameliorate the responsivity of the device at low-frequencies. Different loading schemes have been discussed and a sample traveling-wave device has been designed and analyzed.

The effects of inhomogeneities in the size and materials of superconducting structures, including heterostructures and micro-constrictions, on the carrier transport characteristics of the device has been studied in detail in the appendix C. A transfer matrix method has been developed, based on a four-dimensional state vector in the Nambu space and the solutions to the Bogoliubov-de Gennes equation, to calculate the probability amplitudes of the ordinary and Andreev reflections as well as the transmission with and without branch crossing and the I-V characteristics of one-dimensional inhomogeneous superconducting structures. The method has been applied to a Nb-Au NSNSN structure, and the role of the Andreev reflection in the device I-V characteristic and the differential conductance has been highlighted. Furthermore, a YBCO micro-constriction has been designed and measured to illustrate the possibility of Josephson-like I-V features for potential device applications, especially at the millimeter-wave and THz domain.

7.2 Future Works

Inasmuch as the research on superconducting optoelectronics involves the aggregate of many challenging disciplines including advanced electromagnetism, solid-state physics, and nanoelectronics; high-frequency, vacuum, and low-temperature measurements; micro- and nano-fabrication; free-space and guided-wave designs and measurements at the visible, near IR, terahertz, and millimeter-wave domains; the following highlights a few of the most prominent continuations to the work of this thesis.

The fabrication and measurement of metal-HTS plasmonic waveguides is a viable means to realize superconducting optical waveguides. These structures are simple and relatively easy to fabricate, and are suitable for a substantial class of guided-wave optoelectronic devices including traveling-wave photodetectors and photomixers. Nevertheless, direct access to a decent fabrication facility is a central requirement for research at the device level. Remote cooperation with an external source would be definitely inadequate, and might compromise productivity and efficiency. At a technical level, great efforts should be made in the high-resolution lithography and etching processes. Figure 7.1 shows two optical waveguides fabricated on a Nb CPW transmission line[1]. Similar structures, albeit with smooth-facets at an optical-grade, would be of particular interest.

The light sensitivity of superconducting junctions and micro-constrictions may provide an alternative to the kinetic-inductive devices. While the kinetic inductive mechanism is suitable for detection/photomixing of optical waves, this novel mechanism might outperform the kinetic inductive response for the millimeter and THz waves, where the energy of

[1]The different colors are due to the Fabry-Perot resonance modes of the structures with different dielectric thicknesses.

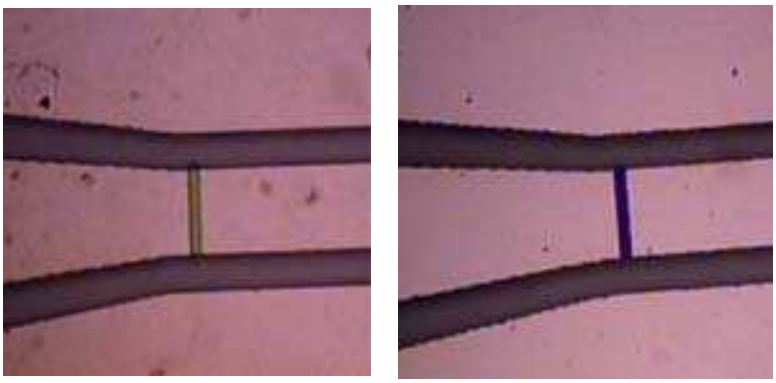

(a) (b)

Figure 7.1: Optical waveguides fabricated across the center strip of a Nb CPW transmission line.

photons is substantially smaller. I-V characteristics of flux-flow juctions, such as the one demonstrated in chapter C, would be the key element in these devices.

Bibliography

[1] E. D. Palik, *Handbook of optical constants of solids.* San Diego: Academic Press, 1998.

[2] R. Kitamura, L. Pilon, and M. Jonasz, "Optical constants of silica glass from extreme ultraviolet to far infrared at near room temperature," *Appl. Opt.*, vol. 64, pp. 8118–8133, 2007.

[3] M. A. Ordal, L. L. Long, R. J. Bell, S. E. Bell, R. R. Bell, J. R. W. Alexander, and C. A. Ward, "Optical properties of the metals Al, Co, Cu, Au, Fe, Pb, Ni, Pd, Pt, Ag, Ti, and W in the infrared and far infrared," *Appl. Opt.*, vol. 22, pp. 1099–1120, 1983.

[4] N. Bluzer, "Temporal relaxation of nonequilibrium in Y-Ba-Cu-O measured from transient photoimpedance response," *Phys. Rev. B*, vol. 44, no. 18, pp. 10 222–10 233, 1991.

[5] C. S. Owen and D. J. Scalapino, "Superconducting states under the influence of external dynamic pair breaking," *Phys. Rev. Lett.*, vol. 28, no. 24, pp. 1559–1561, 1972.

[6] G. A. Sai-Halasz, C. C. Chi, A. Denenstein, and D. N. Langenberg, "Effect of dynamic external pair breaking in superconducting films," *Phys. Rev. Lett.*, vol. 33, no. 4, pp. 215–219, 1974.

[7] N. Perrin and C. Vanneste, "Response of superconducting films to periodic optical irradiation," *Phys. Rev. B*, vol. 28, no. 9, pp. 5150–5159, 1983.

[8] A. Frenkel, "Mechanism of nonequilibrium optical response of high-temperature superconductors," *Phys. Rev. B*, vol. 48, no. 13, pp. 9717–9725, 1993.

[9] J. Bardeen, L. N. Cooper, and J. R. Schrieffer, "Theory of superconductivity," *Phys. Rev.*, vol. 108, no. 5, pp. 1175–1204, 1957.

[10] M. Lindgren, M. Currie, C. A. Williams, T. Y. Hsiang, P. M. Fauchet, R. Sobolewski, S. H. Moffat, R. A. Hughes, J. S. Preston, and F. A. Hegmann, "Ultrafast photoresponse in microbridges and pulse propagation in transmission lines made from high-T_c superconducting thin films," *IEEE J. Sel. Topics Quantum Electron.*, vol. 2, no. 3, pp. 668–678, 1996.

[11] R. Adam, M. Currie, R. Sobolewski, O. Harnack, and M. Darula, "Picosecond response of optically driven Y-Ba-Cu-O microbridge and Josephson-junction integrated structures," *IEEE Trans. Appl. Supercond.*, vol. 9, no. 2, pp. 4091–4094, 1999.

[12] A. D. Semenov, M. A. Heusinger, K. F. Renk, E. Menschikov, A. V. Sergeev, A. I. Elant'ev, I. G. Goghidze, and G. N. Gol'tsman, "Influence of phonon trapping on the performance of NBN kinetic inductance detectors," *IEEE Trans. Appl. Supercond.*, vol. 7, no. 2, pp. 3083–3086, 1997.

[13] A. V. Sergeev, V. V. Mitin, and B. S. Karasik, "Ultrasensitive hot-electron kinetic-inductance detectors operating well below the superconducting transition," *Appl. Phys. Lett.*, vol. 80, no. 5, pp. 817–819, 2002.

[14] R. Sobolewski, "Applications of high-T_c superconductors in optoelectronics," in *Proc. SPIE*, vol. 1512, 1991, pp. 14–27.

[15] ——, "Ultrafast superconducting optoelectronics," in *12th IEEE LEOS Annual Meeting Conference Proceedings*, vol. 2, 1999, pp. 631–632.

[16] R. Sobolewski, A. Verevkin, G. N. Gol'tsman, A. Lipatov, and K. Wilsher, "Ultrafast superconducting single-photon optical detectors and their applications," *IEEE Trans. Appl. Supercond.*, vol. 13, pp. 1151–1157, 2003.

[17] K. M. Rosfjord, J. K. W. Yang, E. A. Dauler, A. J. Kerman, V. Anant, B. M. Voronov, G. N. Gol'tsman, and K. K. Berggren, "Nanowire single-photon detector with an integrated optical cavity and antireflection coating," *Opt. Exp.*, vol. 14, pp. 527–534, 2006.

[18] B. A. Mazin, P. K. Day, H. G. LeDuc, A. Vayonakis, and J. Zmuidzinas, "Superconducting kinetic inductance photon detectors," in *Proc. SPIE*, vol. 4849, 2002, pp. 283–293.

[19] A. H. Majedi, S. K. Chaudhuri, and S. Safavi-Naeini, "Kinetic inductive model of a millimeter-mave high-temperature superconducting optoelectronic mixer," *IEEE Trans. Appl. Supercond.*, vol. 14, no. 3, pp. 1974–1982, 2004.

[20] B. S. Robinson, A. J. Kerman, E. A. Dauler, R. J. Barron, D. O. Caplan, M. L. Stevens, J. J. Carney, S. A. Hamilton, J. K. W. Yang, and K. K. Berggren, "781

Mbit/s photoncounting optical communications using a superconducting nanowire detector," *Opt. Lett.*, vol. 31, pp. 444–446, 2006.

[21] R. Sobolewski, "Ultrafast optoelectronic interface for digital superconducting electronics," *Supercond. Sci. Tech.*, vol. 14.

[22] J. Zhang, N. Boiadjieva, G. Chulkova, H. Deslandes, G. Gol'tsman, a. M. L. A. Komeev, and P. Kouminov, a. R. M. W. Lo, . Okunev, A. Pearlman, W. Slysz, a. A. V. K. Smimov, and C. Tsao, B. Voronov, K. Wilsher, and R. Sobolewski, "Non-invasive CMOS circuit testing with NbN superconducting single-photon detectors," *Elec. Lett.*, vol. 39, no. 14.

[23] W. Slysz, M. Węgrzecki, J. Bar, P. Grabiec, M. Gòrska, V. Zwiller, C. Latta, P. Bohi, I. Milostnaya, O. Minaeva, A. Antipov, O. Okunev, A. Korneev, K. Smirnov, B. Voronov, N. Kaurova, G. Gol'tsman, A. Pearlman, A. Cross, I. Komissarov, A. Verevkinm, and R. Sobolewski, "Fiber-coupled single-photon detectors based on NbN superconducting nanostructures for practical quantum cryptography and photon-correlation studies," *Appl. Phys. Lett.*, vol. 88, p. 261113, 2006.

[24] D. Rosenberg, A. E. Lita, A. J. Miller, S. Nam, and R. E. Schwall, "Performance of photon-number resolving transition-edge sensors with integrated 1550nm resonant cavities," *IEEE Trans. Appl. Supercond.*, vol. 15, pp. 575–578, 2005.

[25] G. Brammertz, P. Verhoeve, D. Martin, A. Peacock, and R. Venn, "Future optical detectors based on Al superconducting tunnel junctions," in *Proc. SPIE*, vol. 5499, 2004, pp. 269–280.

[26] R. Humphreys, P. Hirst, a. N. P. R. Heath, and D. Elliner, and M. A. G. Smith, "Passive mm-wave imager using HTS Josephson junction detectors," in *Proc. SPIE*, vol. 5619, 2004, pp. 59–69.

[27] A. H. Majedi, D. Saeedkia, S. K. Chaudhuri, and S. Safavi-Naeini, "Physical modeling and frequency-response analysis of a high-temperature superconducting terahertz photomixer," *IEEE Trans. Microwave Theory Tech.*, vol. 52, no. 10, pp. 2430–2437, 2004.

[28] C. J. Stevens and D. J. Edwards, "Photomixing reciever using the kinetic inductive effect in high-T_c superconductors," *IEEE Trans. Appl. Supercond.*, vol. 37, no. 23, pp. 1420–1421, 2001.

[29] A. Rothwarf and B. N. Taylor, "Measurement of recombination liftimes in superconductors," *Phys. Rev. Lett.*, vol. 19, no. 1, pp. 27–30, 1967.

[30] A. H. Majedi, "Optical-microwave interaction modeling in superconducting film for microwave/photonic applications," Ph.D. dissertation, University of Waterloo, 2001.

[31] D. Saeedkia, "Modeling and design of photoconductive and superconductive terahertz photomixer sources," Ph.D. dissertation, University of Waterloo, 2005.

[32] L. N. Cooper, "Bound electron pairs in a degenerate Fermi gas," *Phys. Rev.*, vol. 104, no. 4, pp. 1189–1190, 1956.

[33] M. J. Lancaster, *Passive Microwave Device Applications of High-Temperature Superconductors*. Cambridge: Cambridge University Press, 1997.

[34] T. P. Orlando and K. A. Delin, *Foundations of Applied Superconductivity*. Massachusetts: Addison-Wesley, 1991.

[35] F. London, *Superfluids.* New York: Wiley, 1950, vol. 1.

[36] C. A. Balanis, *Advanced Engineering Electromagnetics.* New York: Wiley, 1989.

[37] W. H. Parker, "Modified heating theory of nonequilibrium superconductors," *Phys. Rev. B*, vol. 12, no. 9, pp. 3667–3672, 1975.

[38] J. A. Pals, K. Weiss, P. M. T. M. van Atfekum, R. E. Horstman, and J. Wolter, "Non-equilinrium superconductivity in homogeneous thin films," *Phys. Rep.*, vol. 89, no. 4, pp. 323–390, 1982.

[39] A. A. Abrikosov, L. P. Gorkov, and I. E. Dzyaloshinksi, *Methods of Quantum Field Theory in Statistical Physics.* New Jersey: Prentice-Hall, 1963.

[40] L. R. Testardi, "Destruction of superconductivity by laser light," *Phys. Rev. B*, vol. 4, no. 7, pp. 2189–2196, 1971.

[41] N. Bluzer, "Temporal relaxation of photoinduced nonequilibrium in Niobium," *Phys. Rev. B*, vol. 46, no. 2, pp. 1033–1042, 1992.

[42] ——, "Temporal relaxation measurement of photoinduced nonequilibrium superconductors," *J. Appl. Phys.*, vol. 71, no. 3, pp. 1336–1348, 1992.

[43] N. Bluzer, D. K. Fork, T. H. Geballe, M. R. Beasley, M. Y. Reizer, S. R. Greenfield, J. J. Stankus, and M. Fayer, "Superconducting, transition, and normal state photoresponse in YBCO observed at different temperatures," *IEEE Trans. Mag.*, vol. 27, no. 2, pp. 1519–1522, 1991.

[44] M. Johnson, N. Bluzer, M. Reyzer, T. H. Geballe, S. R. Greenfield, J. J. Stankus, M. D. Fayer, and C. Herring, "Photoresponse of Nb films - observation of biexponen-

tial recovery time of the superconducting state," *IEEE Trans. Mag.*, vol. 27, no. 2, pp. 1523–1527, 1991.

[45] M. Tinkham, *Introduction to Superconductivity.* New York: Dover Publication Inc., 1996.

[46] C. Williams, Y. Xu, R. Adam, M. Darula, O. Harnack, J. Scherbel, M. Siegel, F. Hegmann, and R. Sobolewski, "Ultrafast YBCO photodetectors based on the kinetic inductive process," *IEEE Trans. Appl. Supercond.*, vol. 11.

[47] C. Williams, R. Adam, Q. Xie, R. Sobolewski, and O. Harnack, "Nonequilibrium kinetic inductive response of YBaCuO photodetectors," *Super. Sci. Tech.*, vol. 12, pp. 843–846, 1999.

[48] N. Bluzer and M. G. Forrester, "Quantum detectors in superconducting YBCO," *IEEE. Trans. Appl. Supercond.*, vol. 5, no. 2, pp. 2583–2586, 1995.

[49] ——, "Superconducting quantum detectors," *Opt. Eng.*, vol. 33, no. 3, pp. 697–703, 1994.

[50] ——, "Quantum detectors in superconducting YBCO," *J. Supercond.*, vol. 7, no. 2, pp. 395–398, 1994.

[51] N. Bluzer, "Analysis of quantum superconducting kinetic inductance photodetectors," *J. Appl. Phys.*, vol. 78, no. 12, pp. 7340–7351, 1995.

[52] E. N. Grossman, D. G. McDonald, and J. E. Sauvageau, "Far-infrared kinetic inductance detectors," *IEEE. Trans. Appl. Supercond.*, vol. 27, no. 2, pp. 2677–2680, 1991.

[53] H. A. Atikian, "Microwave photonic characterization of high temperature superconducting optoelectronic devices," Ph.D. dissertation, University of Waterloo, 2009.

[54] R. A. Simons, *Coplanar Waveguide Circuits, Components, and Systems.* New York: Wiley, 2001.

[55] R. Mendis and D. Grischkowsky, "Undistorted guided-wave propagation of subpicosecond terahertz pulses," *Opt.Lett*, vol. 26, p. 846, 2001.

[56] ——, "Modular parallel-plate THz components for cost-efficient biosensing systems," *IEEE Microw. Wirel. Compon. Lett.*, vol. 11, p. 444, 2001.

[57] R. Mendis, "Thz transmission characteristics of dielectric-filled parallel-plate waveguides," *J. Appl. Phys.*, vol. 101, p. 083115, 2007.

[58] ——, "Nature of subpicosecond terahertz pulse propagation in practical dielectric-filled parallel-plate waveguides," *Opt. Lett.*, vol. 31, p. 2643, 2006.

[59] S. Coleman and D. Grischkowsky, "A THz transverse electromagnetic mode two-dimensional interconnect layer incorporating quasi-optics," *App. Phys. Lett.*, vol. 83, p. 3656, 2003.

[60] J. Dai, S. Coleman, and D. Grischkowsky, "Planar THz quasioptics," *App. Phys. Lett.*, vol. 85, p. 884, 2004.

[61] S. Coleman and D. Grischkowsky, "Parallel plate THz transmitter," *App. Phys. Lett.*, vol. 84, p. 654, 2004.

[62] H. Cao, R. A. Linke, and A. Nahata, "Broadband generation of terahertz radiation in a waveguide," *Opt. Lett.*, vol. 29, p. 1751, 2004.

[63] A. Bingham, Y. Zhao, and D. Grischkowsky, "Thz parallel plate photonic waveguides," *App. Phys. Lett.*, vol. 87, p. 051101, 2005.

[64] J. Zhang and D. Grischkowsky, "Whispering-gallery-mode cavity for terahertz pulses," *J. Opt. Soc. Am. B*, vol. 20, p. 1894, 2003.

[65] Z. Jian, J. Pearce, and D. M. Mittleman, "Defect modes in photonic crystal slabs studied using terahertz time-domain spectroscopy," *Opt. Lett.*, vol. 29, p. 2067, 2004.

[66] M. Nagel, P. H. Bolivar, and H. Kurz, "Modular parallel-plate THz components for cost-efficient biosensing systems," *Semicond. Sci. Technol.*, vol. 20, p. S281, 2005.

[67] R. Mendis, "Guided-wave THz time-domain spectroscopy of highly doped silicon using parallel-plate waveguides," *Electron. Lett.*, vol. 42, p. 19, 2006.

[68] H. Raether, *Surface plasmons on smooth and rough surfaces and on gratings.* New York: Springer-Verlag, 1988.

[69] V. M. Shalaev and S. Kawata, *Nanophotonics with Surface Plasmons.* Amsterdam: Elsevier, 2007.

[70] E. N. Economou, "Surface plasmons in thin films," *Phys. Rev.*, vol. 182, pp. 539–553, 1969.

[71] J. J. Burke and G. I. Stegeman, "Surface-polariton-like waves guided by thin, lossy metal film," *Phys. Rev. B*, vol. 33, pp. 5186–5201, 1986.

[72] A. D. Boardman, *Electromagnetic Surface Modes.* New York: Wiley Interscience, 1982.

[73] J. Gomez-Rivas, C. Janke, and a. H. K. P. Bolivar, "Transmission of THz radiation through InSb gratings of subwavelength apertures," *Opt. Express*, vol. 13, pp. 847–59, 2005.

[74] S. A. Maier, *Plasmonics: Foundamentals and Applications*. New York: Springer, 2007.

[75] D. Sarid, "Long-range surface-plasma waves on very thin metal films," *Phys. Rev. Lett.*, vol. 47, p. 1927, 1981.

[76] G. I. Stegeman and J. J. Burke, "Effects of gaps on long range surface plasmon polaritons," *J. Appl. Phys.*, vol. 54, no. 9, pp. 4841–4843, 1983.

[77] P. Berini, "Plasmon-polariton waves guided by thin lossy metal films of finite width: Bound modes of symmetric structures," *Phys. Rev. B*, vol. 61, p. 10484, 2000.

[78] F. Yang, Z. Cao, L. Ruan, and J. Fang, "Long-range surface modes of metal-clad four-layer waveguides," *Appl. Opt.*, vol. 25, pp. 3903–3908, 1986.

[79] C. Themistos, B. M. Azizur Rahman, M. Rajarajan, V. Rakocevic, and K. T. V. Grattan, "Finite element solutions of surface-plasmon modes in metal-clad dielectric waveguides at THz frequency," *IEEE J. Lightwave Tech.*, vol. 24, p. 5111, 2006.

[80] T. Jeon and D. Grischkowsky, "THz Zenneck surface wave (THz surface plasmon) propagation on a metal sheet," *J. App. Phys.*, vol. 88, p. 061113, 2006.

[81] A. Stöhr, A. Malcoci, A. Sauerwald, I. C. Mayorga, R. Güsten, and D. S. Jäger, "Ultra-wide-band traveling-wave photodetectors for photonic local oscillators," *IEEE J. Lighw. Tech.*, vol. 21, p. 3062, 2001.

[82] E. A. Michael, "Travelling-wave photonic mixers for increased continuous-wave power beyond 1 THz," *Semicond. Sci. Technol.*, vol. 20, p. 164, 2005.

[83] A. H. Majedi and B. G. Ghamsari, "Thz signal generation/propagation in an integrated traveling-wave superconductive/photoconductive heterodyne photodetector," in *Proc. SPIE*, vol. 6373, 2006, p. 63730V.

[84] B. G. Ghamsari and A. H. Majedi, "Microwave and millimeter-wave generation in superconductive traveling-wave photomixers," in *21st Annual Meeting of the IEEE LEOS Proc.*, 2008, pp. 423–424.

[85] J.-W. Shi, K.-G. Gan, Y.-J. Chiu, Y.-H. Chen, C.-K. Sun, Y.-J. Yang, and J. E. Bowers, "Metal-semiconductor-metal traveling-wave photodetectors," *IEEE Photon Technol. Lett.*, vol. 16, p. 623625, 2001.

[86] B. G. Ghamsari and A. H. Majedi, "Theory of superconductive traveling-wave photodetectors," *Trans. Appl. Supercond.*, vol. 18, no. 4, pp. 1761–1768, 2008.

[87] J. Gomez-Rivas, M. Kuttge, P. Bolivar, P. Haring, H. Kurz, and J. Sanchez-Gill, "Propagation of surface plasmon polaritons on semiconductor gratings," *Phys. Rev. Lett.*, vol. 93, p. 256804, 2004.

[88] J. Gomez-Rivas, M. Kuttge, H. Kurz, P. Bolivar, P. Haring, H. Kurz, and J. Sanchez-Gill, "Low-frequency active surface plasmon optics on semiconductors," *Appl. Phys. Lett.*, vol. 88, p. 082106, 2006.

[89] W. Barnes and R. Sambles, "Only skin deep," *Science*, vol. 305, p. 785, 2004.

[90] J. B. Pendry, L. Martin-Moreno, and F. J. Garcia-Vidal, "Mimicking surface plasmons with structured surfaces," *Science*, vol. 305, p. 847, 2004.

[91] J. A. Stratton, *Electromagnetic Theory.* McGraw-Hill: Wiley, 1941.

[92] G. I. Stegeman and J. J. Burke, "Long-range surface plasmons in electrode structures," *Appl. Phys. Lett.*, vol. 43, pp. 221–223, 1983.

[93] B. Prade, J. Y. Vinet, and A. Mysyrowicz, "Guided optical waves in planar heterostructures with negative dielectric constant," *Phys. Rev. B*, vol. 44, no. 24, p. 13556, 1991.

[94] B. G. Ghamsari and A. H. Majedi, "THz plasmonic modes in metal-clad planar multilayer waveguides," in *Proc. SPIE*, vol. 7311, 2009, p. 7311B.

[95] ——, "Terahertz transmission lines based on surface waves in plasmonic waveguides," *J. Appl. Phys.*, vol. 104, p. 083108, 2008.

[96] I. P. Kaminow, W. L. Mammel, and H. P. Weber, "Metal-clad optical waveguides: analytical and experimental study," *Appl. Opt.*, vol. 13, no. 2, p. 396, 1974.

[97] B. G. Ghamsari and A. H. Majedi, "Prospects of guided-wave superconductive optoelectronic devices," in *Proc. IEEE Toronto International Conference - Science and Technology for Humanity.*

[98] ——, "Superconductive traveling-wave photodetectors: fundamentals and optical propagation," *IEEE J. Quantum Electron.*, vol. 44, pp. 667–675, 2008.

[99] F. Stella, M. Casalboni, M. Cirillo, V. Merlo, C. Palazzesi, G. P. Pepe, P. Prosposito, and M. Salvato, "Integrating superconductive and optical circuits," *Appl. Phys. Lett.*, vol. 92, p. 202505, 2008.

[100] R. Russo, M. Cirillo, F. DeMatteis, M. Casalboni, V. Merlo, P. Prosposito, L. V. Filippenko, and S. Schutzmann, "Toward optical and superconducting circuit integration," *Supercond. Sci. Tech.*, vol. 17, pp. 456–459, 2004.

[101] A. Gilabert, D. B. Ostrowsky, and C. Vanneste, "Superconducting weak links induced by guided opical waves," *Appl. Phys. Lett.*, vol. 31, no. 9.

[102] K. Yoshida and A. Minami, "Traveling-wave type $LiNbO_3$ optical modulator with a superconducting coplanar waveguide electrode," *IEEE Trans. Appl. Supercond.*, vol. 7, no. 2.

[103] L. Sun and E. Marhic, "Numerical study of attenuation in multilayer infrared waveguides by the circle-chain convergence method," *J. Opt. Soc. Amer. B*, vol. 8, pp. 478–483, 1991.

[104] K. H. Schlereth and M. Tacke, "The complex propagation constant of multilayer waveguides: An algorithm for a personal computer," *IEEE J. Quantum Electron.*, vol. 26, pp. 626–630, 1990.

[105] L. M. Delves and J. N. Lyness, "A numerical method for locating the zeros of an analytic function," *Math. Comp.*, vol. 21, pp. 543–560, 1967.

[106] R. E. Smith, S. N. Houde-Walter, and G. W. Forbes, "Numerical determination of planar waveguide modes using the analyticity of the dispersion relation," *Opt. Lett.*, vol. 16, no. 17, pp. 1316–1318, 1991.

[107] E. Anemogiannis and E. N. Glytsis, "Multilayer waveguides: efficient numerical analysis of general structure," *IEEE J. Lightw. Tech.*, vol. 10, no. 10, pp. 1344–1351, 1992.

[108] C. Chen, P. Berini, D. Feng, S. Tanev, and V. P. Tzolov, "Efficient and accurate numerical analysis of multilayer planar optical waveguides in lossy anisotropic media," *Optics Express*, vol. 7, no. 8, pp. 260–272, 2000.

[109] A. S. Housholder, *The Numerical Treatment of a Single Nonlinear Equation*. New York: McGraw-Hill, 1970.

[110] P. Yeh, *Optical Waves in Layered Media*. New York: Wiley, 2005.

[111] A. S. Kronrod, *Nodes and Weights of Quadrature Formulas*. New York: Consultant Bureau, 1965.

[112] S. Afonso, K. Y. Chen, Q. Xiong, Y. Q. Tang, G. J. Salamo, F. T. Chan, J. Cooksey, S. Scott, Y. J. Shi, S. Ang, W. D. Brown, and L. W. Schaper, "$Y_1Ba_2Cu_3O_{7-x}$ multilayer structures with a thick SiO_2 interlayer for multichip modules," *J. Mater. Res.*, vol. 12, p. 29472951, 1997.

[113] B. G. Ghamsari and A. H. Majedi, "Rigorous analysis of superconducting multilayer optical waveguides," *IEEE Trans. Appl. Supercond.*, vol. 17, pp. 590–593, 2007.

[114] P. Berini, "Plasmon-polariton modes guided by a metal film of finite width bounded by different dielectrics," *OPTICS EXPRESS*, vol. 7, pp. 329–335, 2000.

[115] A. Boltasseva and S. I. Bozhevolnyi, "Directional couplers using long-range surface plasmon polariton waveguides," *IEEE J. Sel. Topics Quantum Electron.*, vol. 12, pp. 1233–1241, 2006.

[116] R. Charbonneau, C. Scales, I. Breukelaar, S. Fafard, N. Lahoud, G. Mattiussi, and P. Berini, "Passive integrated optics elements based on long-range surface plasmon polaritons," *IEEE. J. Lightwav. Tech.*, vol. 24, pp. 477–494, 2006.

[117] B. G. Ghamsari and A. H. Majedi, "Surface plasmon-assisted propagation of optical waves in superconducting active waveguides," in *21st Annual Meeting of the IEEE LEOS Proc.*, 2008, pp. 210–211.

[118] ——, "Plasmonic optical waveguides in superconductive traveling-wave photodetectors," in *Proc. SPIE*, vol. 7099, 2008, p. 709913.

[119] A. H. Majedi, "Traveling-wave photodetection in high-temperature superconducting parallel plate line on semiconductor substrate," in *Proc. SPIE*, vol. 5971, 2005, p. 597121.

[120] K. S. Giboney, M. J. W. Rodwell, and J. E. Bowers, "Traveling-wave photodetectors," *IEEE Photon. Technol. Lett.*, vol. 4, pp. 1363–5, 1992.

[121] ——, "Traveling-wave photodetectors," *IEEE J. Sel. Topics Quantum Electron.*, vol. 2.

[122] V. M. Hietala, A. Vawter, T. M. Brennan, and B. E. Hammons, "Traveling-wave photodetectors for high-power, large bandwidth applications," *IEEE Trans. Microw. Theory Tech.*, vol. 43, pp. 2291–8, 1995.

[123] T. Ishibashi, N. Shimizu, S. Kodama, H. Ito, T. Nagatsuma, and T. Furuta, "Uni-traveling-carrier photodiodes," in *OSA Trends in Optics and Photonics*, vol. 13, 1997, pp. 83–87.

[124] D. Lasaosa, D. Pasquariello, J. Piprek, and J. E. Bowers, "Recent advances in photodetectors with distributed optical amplification," in *Proc. SPIE*, vol. 5246, 2003, pp. 480–490.

[125] J. M. Liu, *Photonic Devices*. Cambridge: Cambridge University Press, 2005.

[126] A. D. Semenov, G. N. Gol'tsman, and A. A. Korneev, "Quantum detection by current carrying superconducting film," *Physica C*, vol. 351, no. 4, pp. 349–356, 2001.

[127] R. Charbonneau, P. Berini, E. Lisicka-Shrzek, and E. Berolo, "Experimental observation of plasmonpolariton waves supported by a thin metal film of finite width," *Opt. Lett.*, vol. 25, no. 11, p. 844, 2000.

[128] P. Berini, R. Charbonneau, N. Lahoud, and G. Mattiussi, "Characterization of long-range surface-plasmon-polariton waveguides," *J. Appl. Phys.*, vol. 98, p. 043109, 2005.

[129] R. Charbonneau, E. Lisicka-Shrzek, and P. Berini, "Broadside coupling to long-range surface plasmons using an angle-cleaved optical fiber," *Appl. Phys. Lett.*, vol. 92, p. 101102, 2008.

[130] R. Daviau, E. Lisicka-Skrzek, R. N. Tait, and P. Berini, "Broadside excitation of surface plasmon waveguides on cytop," *Appl. Phys. Lett.*, vol. 94, p. 091114, 2009.

[131] P. G. de Gennes, *Superconductivity of Metals and Alloys*. New York: Benjamin, 1966.

[132] J. Bardeen, R. Kümmel, A. E. Jacobs, and L. Tewordt, "Structure of vortex lines in pure superconductors," *Phys. Rev.*, vol. 187, no. 2, pp. 556–569, 1969.

[133] R. Kümmel, "Electronic structure of the intermediate state in type-I superconductors," *Phys. Rev. B*, vol. 3, no. 3, pp. 784–793, 1971.

[134] J. Bar-Sagi and C. G. Kuper, "Self-consistent pair potential in an inhomogeneous superconductor," *Phys. Rev. Lett.*, vol. 28, no. 24, pp. 1556–1559, 1972.

[135] W. L. Clinton, "Solvable pair potential for the Bogoliubov-de Gennes equations of space-dependent superconductivity," *Phys. Rev. B*, vol. 8, no. 5, pp. 1962–1964, 1973.

[136] G. E. Blonder, M. Tinkham, and T. M. Klapwijk, "Transition from metallic to tunneling regimes in superconducting microconstrictions: Excess current, charge imbalance, and supercurrent conversion," *Phys. Rev. B*, vol. 25, no. 7, pp. 4515–4532, 1982.

[137] R. Kümmel, U. Gunsenheimer, and R. Nicolsky, "Andreev scattring of quasiparticle wave packets and current-voltage characteristics of superconducting metallic weak links," *Phys. Rev. B*, vol. 42, no. 7, pp. 3992–4009, 1990.

[138] H. Plehn, U. Gunsenheimer, and R. Kümmel, "Subgap peaks and Tomasch-McMillan-Anderson oscillations in the density of states of sns bridges," *J. Low Temp Phys.*, vol. 83, no. 1/2, pp. 71–88, 1991.

[139] H. Ishikawa, S. Kurihara, and Y. Enomoto, "Electronic states and currents in superconducting multilayers," *Physica C*, vol. 336, no. 3, pp. 181–191, 2000.

[140] ——, "Resonant states and currents in superconducting multilayers," *Physica C*, vol. 350, no. 1/2, pp. 62–68, 2001.

[141] M. Ozana, A. Shelankov, and J. Tobicka, "Bogoliubov-de Gennes versus quasiclassical description of Josephson layered structures," *Phys. Rev. B*, vol. 66, no. 5, p. 4508, 2002.

[142] U. Gunsenheimer, U. Schüssler, and R. Kümmel, "Symmetry breaking, off-diagonal scattering, and Josephson currents in mesoscopic weak links," *Phys. Rev. B*, vol. 49, no. 9, pp. 6111–6125, 1994.

[143] L. N. Bulaevskii and M. V. Zyskin, "Energy gap in layered superconductors," *Phys. Rev. B*, vol. 42, no. 16, pp. 10 230–10 240, 1990.

[144] R. Yagi, "Quasiparticle transport in narrow superconducting wires with superconductor/insulator/normal tunnel junctions," *Superlatt. Microstruct.*, vol. 34, no. 3-6, pp. 263–269, 2003.

[145] J. Feng and S. Xiong, "Coherent mesoscopic transport and Andreev reflection in a normal-metal/quantum-dot/superconducting-film/normal-metal system," *Physica C*, vol. 406, no. 3-4, pp. 143–153, 2004.

[146] H. Plehn, O. J. Wacker, and R. Kümmel, "Electronic structre of superconducting multilayers," *Phys. Rev. B*, vol. 49, no. 17, pp. 12 140–12 150, 1994.

[147] M. Vanević and Z. Radović, "Quasiparticle states in superconducting superlattices," *Eur. Phys. J. B*, vol. 46, no. 3, pp. 419–426, 2005.

[148] B. P. Stojković and O. T. Valls, "Density of states in layered short-coherence-length superconducting structures," *Phys. Rev. B*, vol. 50, no. 5, pp. 3374–3383, 1994.

[149] S. Datta and P. F. Bagwell, "Can the Bogoliubov-de Gennes equation be interpreted as a 'one-particle' wave equation?" *Superlatt. Microstruct.*, vol. 25, no. 5/6, pp. 1233–1250, 1999.

[150] A. H. Majedi, "Multilayer Josphson junctions as a multiple quantum well structure," *IEEE Trans. Appl. Superconduct.*, vol. 17, no. 2, pp. 617–620, 2007.

[151] J. E. Mercereau, "Macroscopic quantum phenomena," in *Superconductivity Vol. 1*, R. D. Parks, Ed. New York: Dekker, 1960.

[152] R. P. Huebener, *Magnetic Flux Structures in Superconductors.* New York: Springer-Verlag, 1979.

Appendices

Appendix A

Conditions for Linear Kinetic Inductive Response

Consider a superconducting film under an optical illumination $p(t)$, where $P_0 = \langle p(t) \rangle$ is the average incident power and $s(t) = p(t) - P_0$ is the signal. For the film to be in the superconducting state, the average incident power may not exceed $P_{0,max}$

$$P_{0,max} = \frac{n_0^*(T)}{g_B}, \tag{A.1}$$

where $g_B \equiv (\eta_B \tau_B)/(2\Delta A \ell)$. Under an average incident power P_0, the average steady-state carriers densities read

$$n_s^*(T) = (1 - \alpha_0) n_0^*(T), \tag{A.2}$$

and

$$n_s(T) = 2(\theta + \alpha_0) n_0^*(T), \tag{A.3}$$

where $\alpha_0 = P_0/P_{0,max}$ is the normalized average incident power and $\theta \equiv n_0(T)/2n_0^*(T)$. In order to avoid superconducting-normal transitions the peak incident power is limited to $P_{s,max}$

$$P_{s,max} = \frac{(1-\alpha_0)n_0^*(T)}{g_Q}, \tag{A.4}$$

where $g_Q \equiv (\eta_Q \tau_Q)/(2\Delta A \ell)$. The time varying part of the steady-state carrier densities follow

$$\delta n^*(t,T) = -\alpha_s(1-\alpha_0)n_0^*(T), \tag{A.5}$$

and

$$\delta n(t,T) = +2\alpha_s(1-\alpha_0)n_0^*(T), \tag{A.6}$$

where $\alpha_s = s(t)/P_{s,max}$ is the normalized signal power. Therefore,

$$L_k(t) = \frac{L_{k0}}{1-\alpha_s}, \tag{A.7}$$

and

$$R_n(t) = \frac{R_{n0}}{1+\rho_s}, \tag{A.8}$$

where

$$L_{k0} = \frac{m_0 \ell}{2e^2 A n_s^*}, \tag{A.9}$$

and

$$R_{n0} = \frac{m_0 \ell}{e^2 A \tau_{tr} n_s}, \tag{A.10}$$

and $\rho_s = \alpha_s(1-\alpha_0)/(\theta+\alpha_0)$. Linear operation requires that $|\alpha_s| \ll 1$ and $|\rho_s| \ll 1$. In terms of the peak-to-average ratio of the incident optical power $\zeta \equiv p_{max}/P_0$, one can

readily rewrite the conditions of linear operation as

$$\frac{g_0\alpha_0\zeta}{1-\alpha_0} \ll 1, \tag{A.11}$$

and

$$\frac{g_0\alpha_0\zeta}{\theta+\alpha_0} \ll 1, \tag{A.12}$$

where

$$g_0 \equiv \frac{g_Q}{g_B} = \frac{\eta_Q\tau_Q}{\eta_B\tau_B}. \tag{A.13}$$

Appendix B

Cutback Measurement for Long-Range Surface Plasmon Waveguides

This appendix briefly overviews the basic setup and experimental techniques for the excitation and characterization of the surface plasmon mode of metal strip waveguides[1]. Figure B.1 illustrates the schematic of the waveguide structures, where a 30nm-thick gold strip is embedded inside a dielectric medium. Two sets of waveguides are measured, in which SiO_2 and Cytop are used as the dielectric medium respectively [116, 127–130]. All the devices are fabricated on SiO_2 substrates, and only differ in the width and the length of the gold strip.

The schematic of the measurement setup is depicted in Figure B.2. A 1550nm laser diode is used to excite the waveguide. The laser light is guided through a polarization

[1]The devices were designed and fabricated by Professor Berini's Group at the School of Information Technology and Engineering, University of Ottawa. The presented measurements were performed, by the author, at Professor Berini's Laboratory.

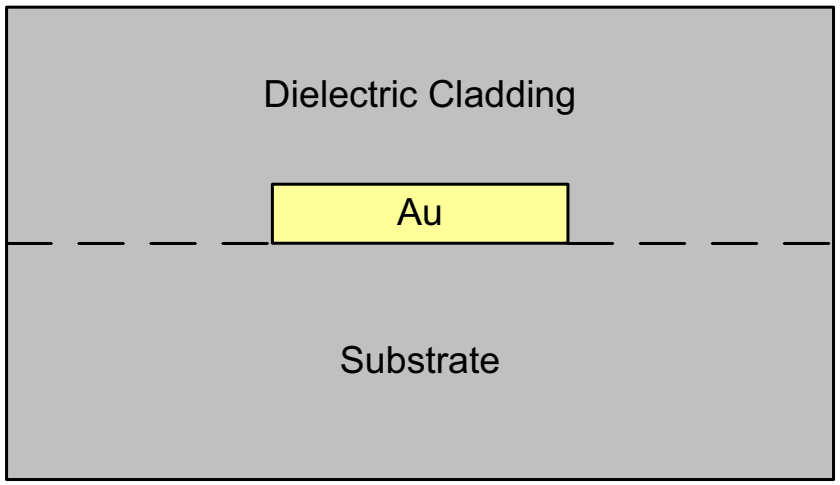

(a)

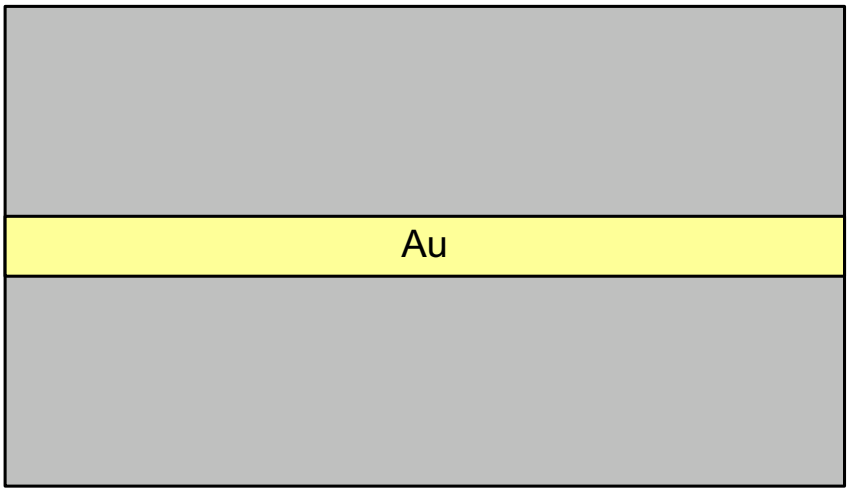

(b)

Figure B.1: A long-range surface plasmon waveguide. (a) Side-view (b) Top-view .

Table B.1: The results of cutback measurement for the waveguides of Figure B.3 and Figure B.4.

Dielectric	Strip Width W (μm)	Propagation Loss α (dB/mm)	Coupling Loss C (dB)
SiO_2	4	3.12	1.43
SiO_2	8	3.68	2.21
Cytop	5.4	6.74	3.02

maintaining fiber (PMF) to the waveguide. The tip of the fiber and the edges of the waveguides are carefully cleaved to maximize the coupling. The close effective indices of the fiber mode and the long-range surface plasmon wave enables the direct excitation of the waveguide. The lateral position of the fiber is optimized by means the precision positioning stages. A far-field image of the plasmonic mode may be obtained using a series of lenses. The insertion loss of a waveguide can be measured through coupling the output facet of the waveguide into a fiber, as illustrated in Figure B.2b. The cut-back measurement technique is applied to characterize the waveguides' attenuation constant. For each waveguide, the insertion loss (IL) is measured for devices with different lengths; and liner model is fitted to the data

$$IL = 2C + \alpha L, \tag{B.1}$$

where C (dB) is the coupling loss at the facets, α (dB/mm) is the attenuation constant of the waveguide, and $L(mm)$ is the device length. Figure B.3 and Figure B.4 illustrate the result of the cut-back measurements for the waveguide devices. The results are summarized in Table B.1.

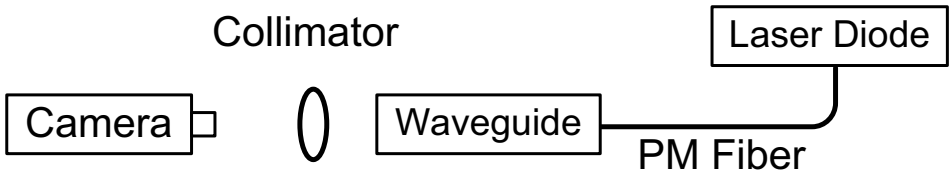

(a)

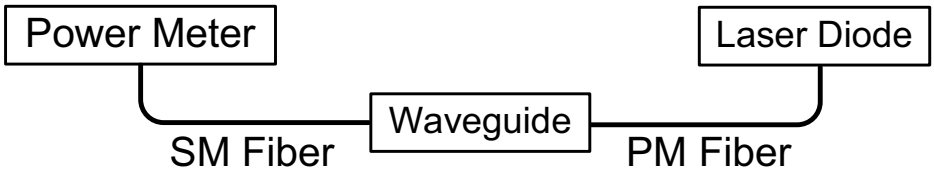

(b)

Figure B.2: Schematic of the setup for (a) imaging the mode profile and (b) cutback measurement.

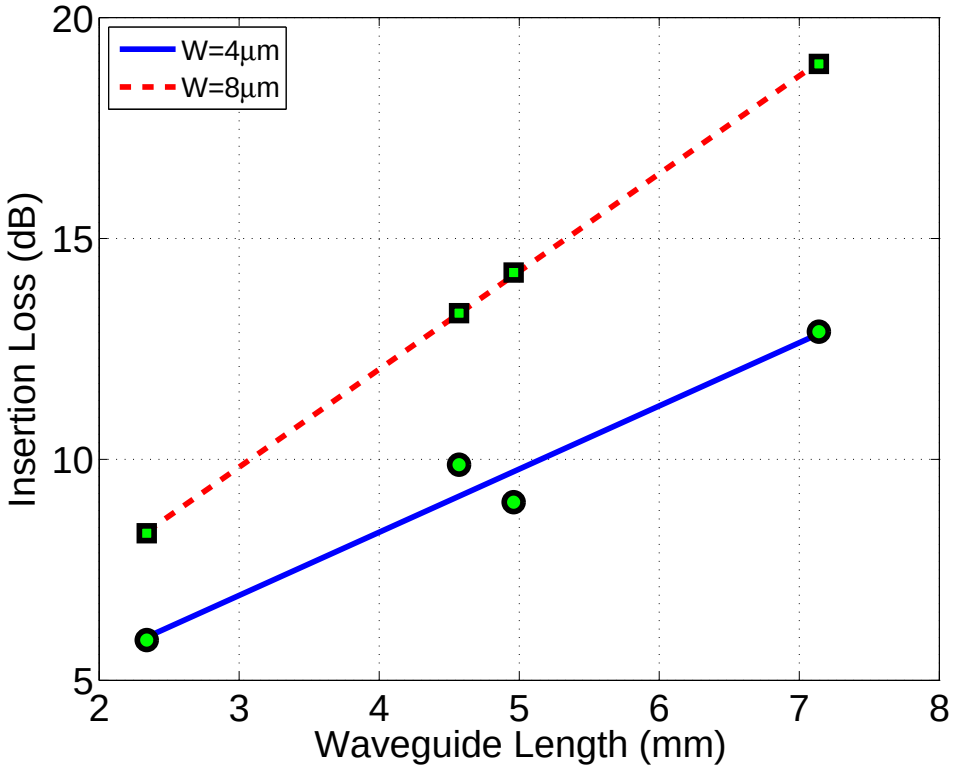

Figure B.3: Measured insertion loss for the long-range surface plasmon mode of a 30nm-thick gold strip inside SiO_2.

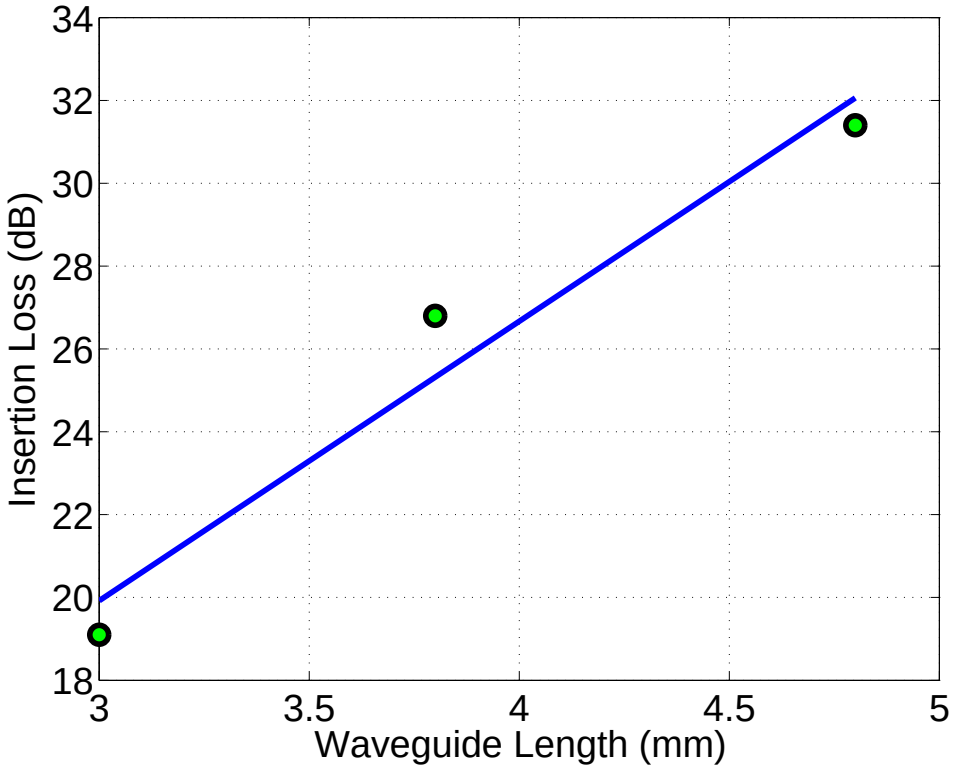

Figure B.4: Measured insertion loss for the long-range surface plasmon mode of a 30nm-thick gold strip inside Cytop.

Appendix C

Carrier Transport in Superconductive Heterostructures, Superlattices, and Micro-Constrictions

C.1 Introduction

The electronic structure of superconducting heterostructures and micro-constrictions has recently received renewed attention. On the one hand, the advancement of nanofabrication technology has enabled the realization of artificial superconducting superlattices for potential device applications. On the other hand, the intrinsically layered structure of high-temperature superconductors motivates the research in the field for a better understanding of the mechanism of superconductivity in these materials.

In many of the optoelectronic and microwave-photonic devices that have been studied so far, it is often required that the feature size of the superconducting structure shrinks down to a (sub)micron scale over a short length. This abrupt change in the dimension of

the superconductor may squeeze the pairing potential field Δ, which in turn perturbs the electrical properties of the device. In particular, such phenomena as the Andreev reflection or Josephson tunneling may be induced within the device. While these effects should be avoided in a kinetic-inductive device, they might provide novel mechanisms for doing optoelectronics as well.

Generally, Bogoliubov-de Gennes (BdG) equation is used to study electronic excitations within inhomogeneous superconductors [131]. Closed form solutions to the BdG equation can be found only in a few cases, therefore the Wentzel-Kramers-Brillouin-Jeffreys (WKBJ) approximation has been used for many problems such as the structure of vortex lines in pure type-II superconductors [132], the intermediate states in type-I superconductors [133], and the self-consistent pair potentials in SN junctions [134, 135].

The celebrated Blonder-Tinkham-Klapwijk (BTK) work [136] is a milestone, where the BdG equation was used to study quasiparticle transport and the I-V characteristic of NS junctions with particular emphasis on the role of Andreev reflection in the excess current and the enhancement of the differential conductance. Ever since the BTK work, many researchers have used the method to study different aspects of layered superconductors, superlattices, and weak-links, such as the I-V characteristics [137–142], energy gaps [143], the quasiparticle transport [144, 145], bound states spectrum [146, 147] and density of states [148].

Besides the standard interpretation of the BdG equation, there has been also several attempts to interpret the BdG equation as a single-particle wave equation [149] and even more phenomenological approaches based on a macroscopic wave function [150] in the same way as other macroscopic quantum phenomena, such as the Josephson effect [151]. Interestingly, these phenomenological approaches have succeeded to repeat many of the previously known results with more simplicity, however this work strictly follows the stan-

dard theory [131, 136].

In this chapter a transfer matrix approach is introduced for modeling layered superconductive heterostructures, and the propagator and boundary matrices are explicitly defined based on the solutions of the BdG equation. It is then discussed how the scattering probability amplitudes for Andreev and ordinary reflection as well as transmission with and without branch-crossing are computed from the structure's transfer matrix. The scattering probability amplitudes are in turn used to obtain the I-V relation of the structure, as well as its differential conductance versus the voltage. As an example, the method is applied to a niobium NSNSN device. The possibility of Josephson-like features will be also illustrated by means of transport measurement in a YBCO micro-constriction.

C.2 Analysis and Formulation

Consider a one-dimensional multilayer superconductive structure consisting of N interlayers sandwiched between the left (L) and right (R) contacts, as shown in Figure C.1. Each layer is characterized by its length d_i, pair potential Δ_i, carriers effective mass m_i^*, and electrostatic potential U_i. A delta potential $W_i\delta(z_i)$ is used to model the finite transparency of the junction between the ith and $(i+1)$th layers. The unitless parameter $Z_i \equiv (m_0 W_i)/(\hbar^2 k_F)$ quantifies the strength of the barrier, where m_0 and $\hbar$ respectively are the mass of an electron and the reduced Plank's constant, and k_F is the Fermi wavevector of the structure at equilibrium. The BdG equation governs the quasiparticles states in the structure

$$\begin{pmatrix} H_0(\mathbf{r}) & \Delta(\mathbf{r}) \\ \Delta^*(\mathbf{r}) & -H_0^*(\mathbf{r}) \end{pmatrix} \begin{pmatrix} u(\mathbf{r}) \\ v(\mathbf{r}) \end{pmatrix} = E \begin{pmatrix} u(\mathbf{r}) \\ v(\mathbf{r}) \end{pmatrix}, \tag{C.1}$$

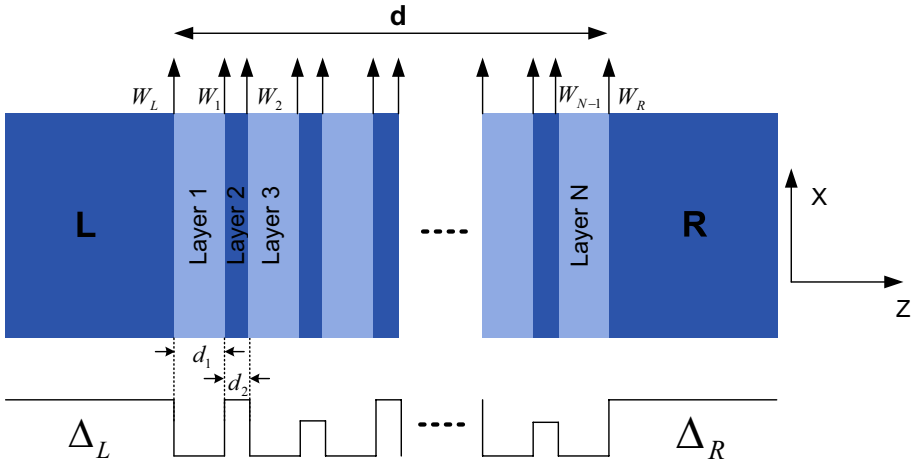

Figure C.1: Schematic of a general one-dimensional layered superconducting structure.

where E is the quasiparticle energy measured from the chemical potential μ, $\begin{pmatrix} u(\mathbf{r}) \\ v(\mathbf{r}) \end{pmatrix}$ is the quasiparticle wavevector in the Nambu space, and H_0 is the single-particle Hamiltonian. In absence of a magnetic field $\mathbf{A} = 0$ and within the ith layer, i.e. $z_i < z < z_{i+1}$, the Hamiltonian reads

$$H_{0,i} = -\nabla \frac{\hbar^2}{2m_i^*} \nabla + \mu + U_i + W_i \delta(z - z_{i+1}). \tag{C.2}$$

Within the ith layer

$$\begin{aligned} \begin{pmatrix} u_i \\ v_i \end{pmatrix} &= a_i^+ \begin{pmatrix} u_{0i} \\ v_{0i} \end{pmatrix} \sin[k_i^+(z - z_i)] + b_i^+ \begin{pmatrix} u_{0i} \\ v_{0i} \end{pmatrix} \cos[k_i^+(z - z_i)] \\ &+ a_i^- \begin{pmatrix} v_{0i} \\ u_{0i} \end{pmatrix} \sin[k_i^-(z - z_i)] + b_i^- \begin{pmatrix} v_{0i} \\ u_{0i} \end{pmatrix} \cos[k_i^-(z - z_i)], \end{aligned} \tag{C.3}$$

where

$$k_i^{\pm} = \sqrt{2m_i^*(\mu + U_i \pm \epsilon_i)/\hbar^2}, \tag{C.4}$$

$$\epsilon_i = \sqrt{E^2 - |\Delta_i|^2}, \tag{C.5}$$

and

$$u_{0i}^2 = 1 - v_{0i}^2 = [1 + \epsilon_i/E]/2. \tag{C.6}$$

While the value of $u(\mathbf{r})$ and $v(\mathbf{r})$ would suffice to describe the state of the quasiparticle at every point in a uniform superconductor, the spatial derivative of the coherence factors $\nabla u(\mathbf{r})$ and $\nabla v(\mathbf{r})$ are also required to give a complete description of the quasiparticle state in an inhomogeneous structure. Therefore, the generalized state vector of a quasiparticle at a point z in the ith layer of a one-dimensional structure is represented as

$$\Psi_i(z) \equiv \begin{pmatrix} u_i(z) \\ v_i(z) \\ u_i'(z) \\ v_i'(z) \end{pmatrix} \tag{C.7}$$

where $u'(z)$ and $v'(z)$ are derivatives of u and v with respect to z. The propagator matrix of the ith layer and the boundary matrix of the interface of the ith and $(i+1)$th layers are defined as

$$\Psi_i(z_i) \equiv P_i \Psi_i(z_{i+1}), \tag{C.8}$$

and

$$\Psi_i(z_{i+1}) \equiv B_i \Psi_{i+1}(z_{i+1}). \tag{C.9}$$

From (C.3) and the boundary conditions:

$$P_i = \begin{pmatrix} \alpha^+ & -\beta & \frac{\gamma^{+,-}}{k_i^+ k_i^-} & \frac{\lambda^-}{k_i^+ k_i^-} \\ \beta & \alpha^- & -\frac{\lambda^-}{k_i^+ k_i^-} & -\frac{\gamma^{-,+}}{k_i^+ k_i^-} \\ \gamma^{+,+} & -\lambda^+ & \alpha^+ & -\beta \\ \lambda^+ & \gamma^{-,-} & \beta & \alpha^- \end{pmatrix}, \tag{C.10}$$

where

$$\alpha^\pm = \eta(u_{0i}^2 c^\pm - v_{0i}^2 c^\mp), \tag{C.11a}$$

$$\beta = \eta u_{0i} v_{0i} (c^+ - c^-), \tag{C.11b}$$

$$\gamma^{\pm,\pm} = \eta(u_{0i}^2 s^\pm k_i^\pm - v_{0i}^2 c^\mp k_i^\mp), \tag{C.11c}$$

$$\lambda^\pm = \eta(u_{0i} v_{0i} (k_i^\pm s^+ - k_i^\mp s^-), \tag{C.11d}$$

and

$$s^\pm = \sin(k_i^\pm d_i), \tag{C.12a}$$

$$c^\pm = \cos(k_i^\pm d_i), \tag{C.12b}$$

$$\eta = 1/(u_{0i}^2 - v_{0i}^2). \tag{C.12c}$$

Similarly,

$$B_i = \begin{pmatrix} 1 & 0 & 0 & 0 \\ 0 & 1 & 0 & 0 \\ -2Z_i k_F m_{r,i} & 0 & m_{r,i} & 0 \\ 0 & -2Z_i k_F m_{r,i} & 0 & m_{r,i} \end{pmatrix}, \tag{C.13}$$

where $m_{r,i} = m_i^*/m_{i+1}^*$.

Therefore, the transfer matrix of the structure is obtained as

$$\Psi_L(0) \equiv T\Psi_R(d) = \left(B_L \prod_{i=1}^{N} P_i B_i \right) \Psi_R(d), \tag{C.14}$$

where $d = \sum_{i=1}^{N} d_i$ is the length of the whole structure.

Hence, the problem of scattering of an incoming wave packet by the multilayer heterostructure reduces to the scattering by a single effective interface which is modeled by T. For an incident excitation from the left, the solutions of the BdG equation in the left and right contacts, which respectively involve incoming and outgoing particles, are

$$\begin{pmatrix} u_L \\ v_L \end{pmatrix} = \begin{pmatrix} u_{0L} \\ v_{0L} \end{pmatrix} e^{-jk_L^+ z} + a_0 \begin{pmatrix} v_{0L} \\ u_{0L} \end{pmatrix} e^{-jk_L^- z} + b_0 \begin{pmatrix} u_{0L} \\ v_{0L} \end{pmatrix} e^{jk_L^+ z}, \tag{C.15}$$

and

$$\begin{pmatrix} u_R \\ v_R \end{pmatrix} = c_0 \begin{pmatrix} u_{0R} \\ v_{0R} \end{pmatrix} e^{-jk_R^+ (z-d)} + d_0 \begin{pmatrix} v_{0R} \\ u_{0R} \end{pmatrix} e^{jk_R^- (z-d)}. \tag{C.16}$$

Defining

$$S \equiv \begin{pmatrix} a_0 \\ b_0 \\ c_0 \\ d_0 \end{pmatrix}, \tag{C.17}$$

the state vectors at the two contact boundaries can be written as

$$\Psi_L(0) = A_L S + G, \tag{C.18}$$

and

$$\Psi_R(d) = A_R S, \tag{C.19}$$

where the explicit form of $A_{L,R}$ and G can be obtained from (C.15) and (C.16), and are

$$A_L = \begin{pmatrix} v_{0L} & u_{0L} & 0 & 0 \\ u_{0L} & v_{0L} & 0 & 0 \\ jk_L^- v_{0L} & -jk_L^+ u_{0L} & 0 & 0 \\ jk_L^- u_{0L} & -jk_L^+ v_{0L} & 0 & 0 \end{pmatrix}, \tag{C.20}$$

$$A_R = \begin{pmatrix} 0 & 0 & u_{0R} & v_{0R} \\ 0 & 0 & v_{0R} & u_{0R} \\ 0 & 0 & jk_R^+ u_{0R} & -jk_R^- v_{0R}) \\ 0 & 0 & jk_R^+ v_{0R} & -jk_R^- u_{0R}) \end{pmatrix}, \tag{C.21}$$

and

$$G = \begin{pmatrix} u_{0L} \\ v_{0L} \\ jk_L^+ u_{0L} \\ jk_L^+ v_{0L} \end{pmatrix}. \tag{C.22}$$

In fact, the problem of scattering of an excitation by the structure reduces to a system of linear equations given by

$$(TA_R - A_L)S = G. \tag{C.23}$$

Following the BTK arguments [136], the probability amplitudes of Andreev and ordinary reflection as well as transmission without and with branch-crossing's respectively are

$$A(E) = \frac{v_L^-}{v_F} a_0 a_0^* (|u_{0L}|^2 - |v_{0L}|^2), \tag{C.24a}$$

$$B(E) = \frac{v_L^+}{v_F} b_0 b_0^* (|u_{0L}|^2 - |v_{0L}|^2), \tag{C.24b}$$

$$C(E) = \frac{v_R^+}{v_F} c_0 c_0^* (|u_{0R}|^2 - |v_{0R}|^2), \tag{C.24c}$$

$$D(E) = \frac{v_R^-}{v_F} d_0 d_0^* (|u_{0R}|^2 - |v_{0R}|^2), \tag{C.24d}$$

where

$$v_{L,R}^{\pm} = \hbar k_{L,R}^{\pm} / m_{L,R}^*. \tag{C.25}$$

Hence, the current density through the multilayer heterostructure is

$$J = 2N(0) e v_F \int_{-\infty}^{+\infty} [f_0(E - eV) - f_0(E)][1 + A(E) - B(E)] dE, \tag{C.26}$$

where $N(0)$ is the single-spin density of states at Fermi level, e is the electric charge of an electron, V is the applied voltage and f_0 is the fermi function.

C.3 Numerical Example

This section applies the method of the previous section to a niobium-gold NSNSN structure. For the sake of simplicity, one may assume $T = 0K$, equal effective masses $m_i^* = m_0$, and transparent junctions $Z_i = 0$. For an incident electron from the left, there is no ordinary reflection and branch-crossing transmission, since all the junctions are transparent. Figure C.2 shows the probability amplitude of Andreev reflection and ordinary transmission for different layers thicknesses. By inspection, one can observe that for a larger thickness, the scattering amplitudes approach to that of a simple metallic NS junction. Also, at some specific energies, the incident electron undergoes total Andreev reflection or total transmission. These situations correspond to the Bragg reflection/transmission and are

responsible for the formation of stop/pass bands in an infinite periodic structure.

Figure C.3 shows the I-V curves associated with each structure. It is readily seen that the curves fall between the I-V characteristics of SN and NN junctions. Therefore, by tuning the layer thickness one can engineer the I-V curve. To achieve better control, it is necessary to have more number of layers. At sufficiently high voltages, the conductance of the device approaches to that of an NN metallic junction, nevertheless there is a finite difference between those curves and the I-V of the NN junction. In fact, this difference is the excess current resulting from the superconductivity of the device. The excess current can also be tuned by appropriate thickness of the layers, between zero and the excess current of a metallic SN junction.

Figure C.4 shows the differential conductance of the devices. Due to absence of ordinary reflection the differential conductance is always between two and unity. In case of finite transparency at the junctions, i.e. $Z \neq 0$, both the excess current and differential conductance decrease. This is due to the suppression of Andreev reflection at the junctions and the increase in ordinary reflection.

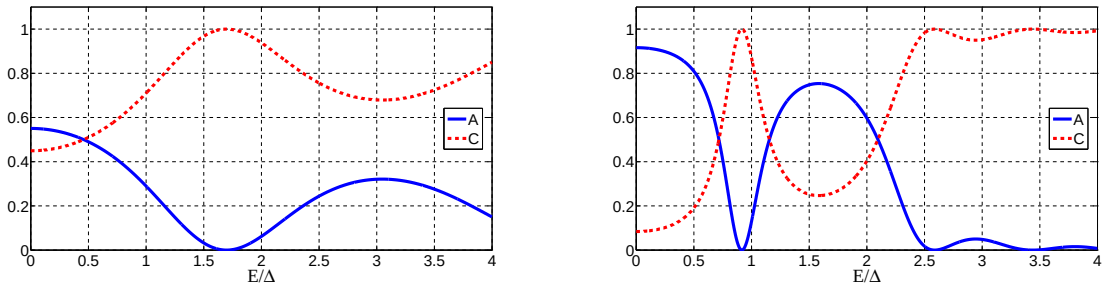

(a)

(b)

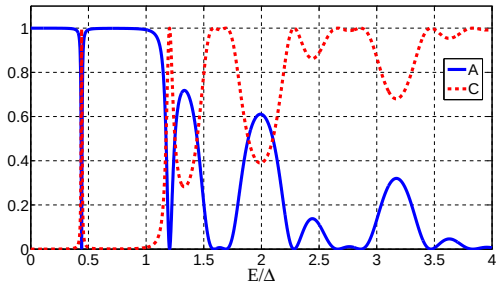

(c)

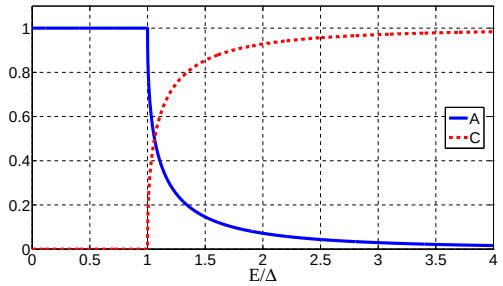

(d)

Figure C.2: Simulated probability amplitudes for the Andreev reflection, A (solid lines), and ordinary transmission, C (dashed lines), for niobium heterostructure at $T = 0K$ with $\Delta/E_F = 2.82 \times 10^{-4}$ and $Z = 0$. (a) NSNSN with $d = 1.5\xi_0$; (b) NSNSN with $d = 3\xi_0$; and (c) NSNSN with $d = 8\xi_0$; (d) An NS junction.

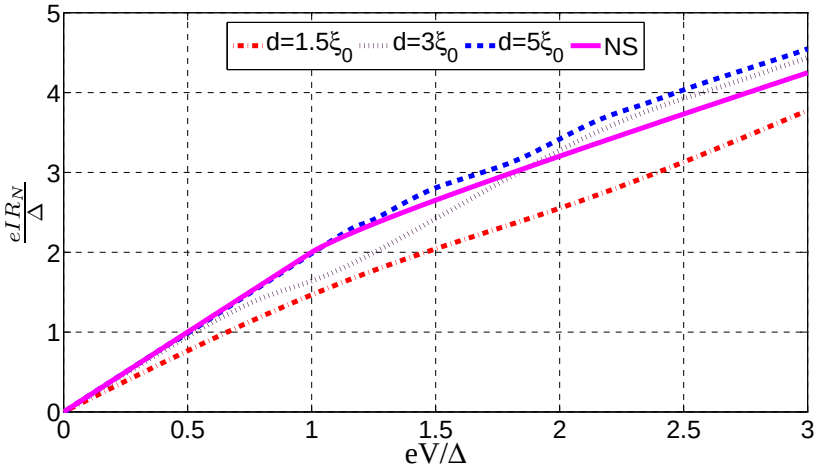

Figure C.3: Simulated I-V characteristics for niobium heterostructure at $T = 0K$ with $\Delta/E_F = 2.82 \times 10^{-4}$ and $Z = 0$. Solid-line curve is for an NS junction, dashed line, dotted line and dash-dotted line are for an NSNSN array with $d = 1.5\xi_0$, $d = 3\xi_0$ and $d = 8\xi_0$, respectively.

C.4 Current-Voltage Measurement of a YBCO Micro-Bridge

This section demonstrate a Josephson-like current-voltage characteristic in a YBCO micro-bridge. Figure C.5 shows the physical structure of the device, where two superconducting banks are connected through a 1μm$\times 2\mu$m micro-bridge. The whole structure is made out of a 100nm-thick YBCO film on top of LAO substrate.

Figure C.6 illustrates the device's current-voltage characteristic, which was measured in a four-point measurement setup at a temperature of 77K. Figure C.7 shows the characteristic near the Josephson state. Clearly, the device exhibits a superconducting state up to a critical current around 8mA. Then a transition state is seen followed by an abrupt jump to the resistive state. The transition state is not normally observed in the Josephson junctions based on Type-I superconductors. Given that YBCO is a Type-II superconductor,

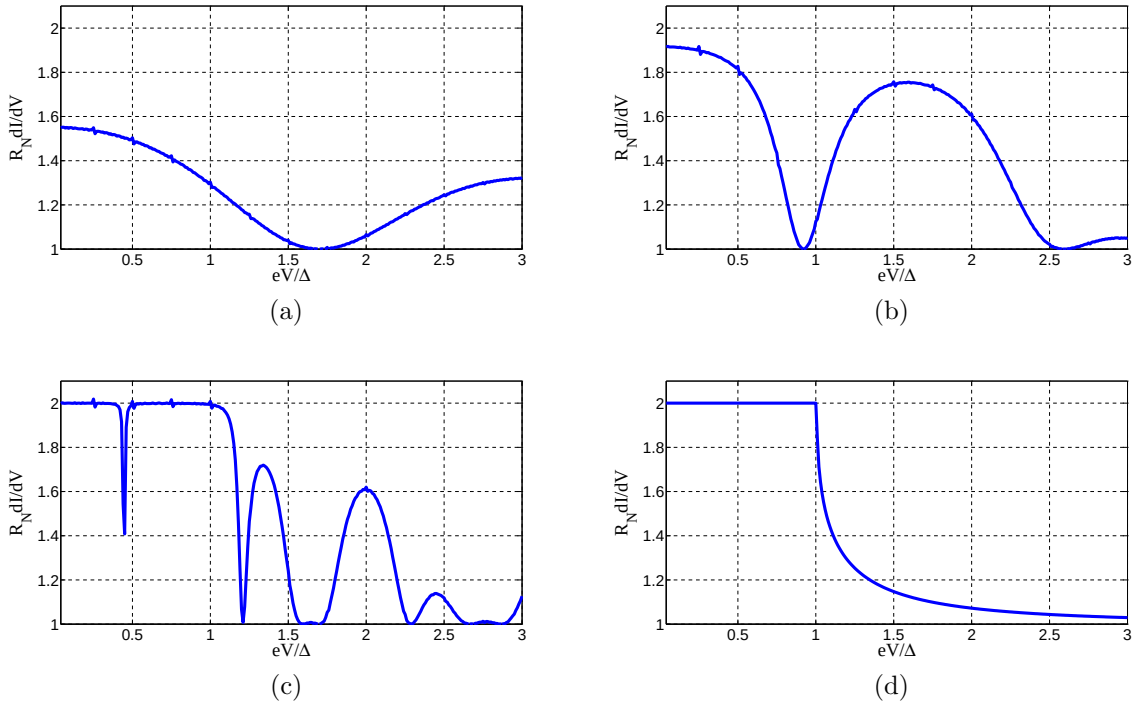

Figure C.4: Simulated differential conductance vs, voltage for variable unit cell length of a niobium heterostructure at $T = 0K$ with $\Delta/E_F = 2.82 \times 10^{-4}$ and $Z = 0$. (a) NSNSN with $d = 1.5\xi_0$; (b) NSNSN with $d = 3\xi_0$; (c) NSNSN with $d = 8\xi_0$ and (d) an NS junction.

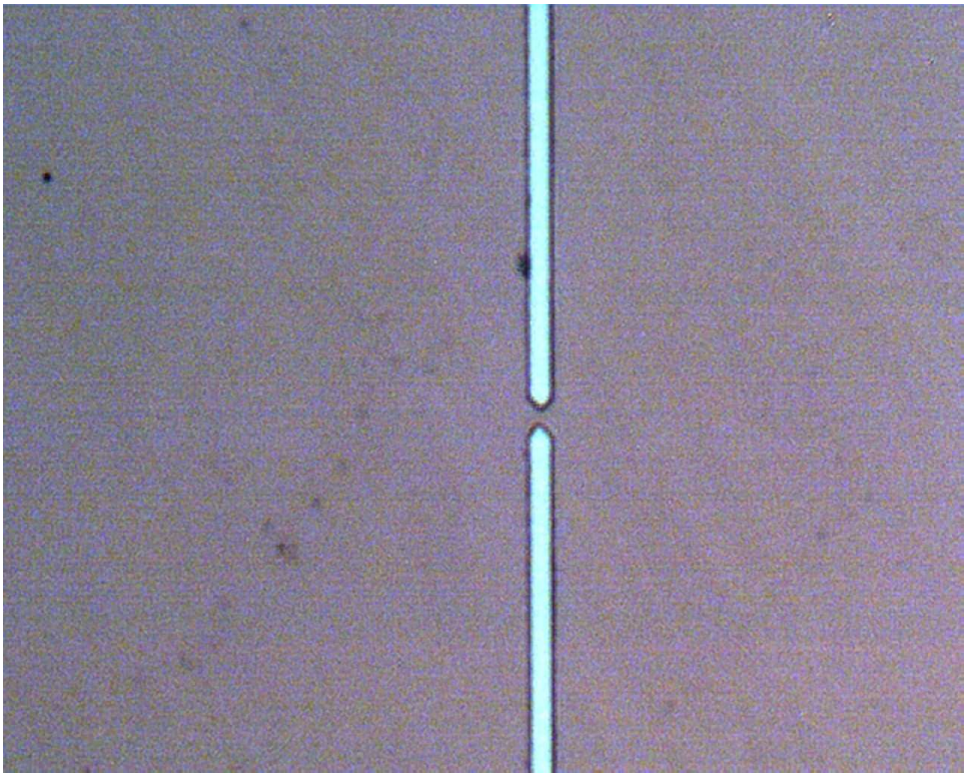

Figure C.5: The optical image of a YBCO micro-constriction device. The device consists of two superconducting banks connected by a 1μm$\times 2\mu$m micro-bridge.

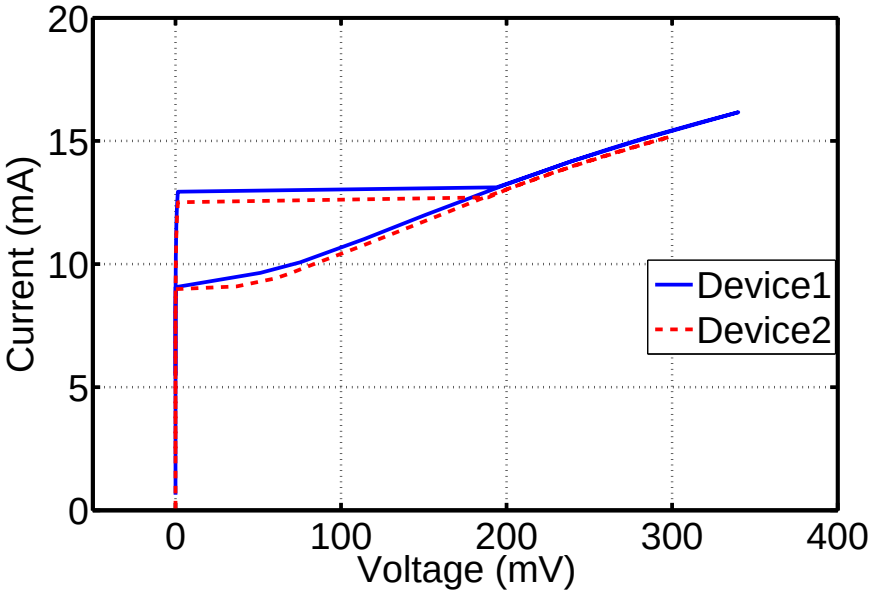

Figure C.6: The measured I-V characteristic of the YBCO micro-constriction at 77K.

the transition feature may be attributed to the vortex-flow state and the phase-slip centers in the bridge due to the self-magnetization [152]. On the reverse direction, a prominent hysteresis is seen in the I-V characteristic.

While the micro-bridge structure is commonly used as an optoelectronic element, this measurement shows that different electronic states may occur upon shrinking down the size of the device, which could impede the kinetic inductive response. Nevertheless, the Josephson-like I-V feature, might be employed as an alternative mechanism for novel opto-electronic and microwave-photonics applications. This possibility is even more pronounced for the millimeter-wave and THz regime due to the enhancement of the Josephson-like voltage/current scales by a factor of at least 10.

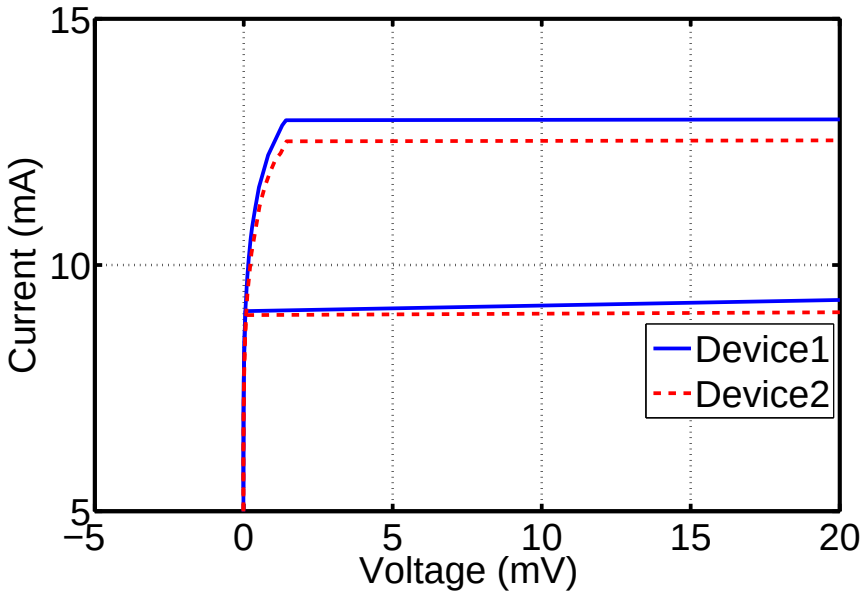

Figure C.7: The measured I-V characteristic of the YBCO micro-constriction near the zero-voltage state.

Index